Title
A Magnetic Resonance Perspective of Adsorbates Motion in Metal Organic Frameworks

Author
Witherspoon, Velencia Jasmine

Publication Date
2017

Peer reviewed|Thesis/dissertation

A Magnetic Resonance Perspective of Adsorbates Motion in Metal Organic Frameworks

by

Velencia Witherspoon

A dissertation submitted in partial satisfaction of the

requirements for the degree of

Doctor of Philosophy

in

Chemical Engineering

in the

Graduate Division

of the

University of California, Berkeley

Committee in charge:

Professor Jefferey Reimer, Chair
Professor Berend Smit
Professor Ting Xu

Spring 2017

A Magnetic Resonance Perspective of Adsorbates Motion in Metal Organic Frameworks

Abstract

A Magnetic Resonance Perspective of Adsorbates Motion in Metal Organic Frameworks

by

Velencia Witherspoon

Doctor of Philosophy in Chemical Engineering

University of California, Berkeley

Professor Jefferey Reimer, Chair

One of the most promising novel materials being developed is a type of nano-porous media referred to as Metal Organic Frameworks (MOFS). MOFs can be envisioned as Tinker Toys^{TM}, with inorganic paddle wheels and organic connecting sticks. MOFs are a novel type of porous materials that have shown unprecedented storage capacities, separation selectivity, and chemical reactivity as solid catalysts. These attributes are further enriched by the modularity of MOF structures, including the ability to tune geometry (pore size), topology (pore shape(s)), chemical affinity (linker design), and reactivity (metal coordination chemistry). This diverse array of applications requires a thorough understanding of MOF-adsorbate interactions in a wide range of thermodynamically diverse operating conditions. Although there are many macroscopic techniques available to researchers, very few techniques can probe the relevant times (ns) and length scales (nm) of the molecular interactions that contribute to the overall performance MOF materials. I have chosen to use Nuclear Magnetic Resonance (NMR) to probe these interactions because NMR is a non-destructive tool that can access in-situ molecular motion and energetics at these time and length scales, while minimizing the amount MOF needed (mg). The NMR observables (i.e. trends in longitudinal relaxation, transverse relaxations, self-diffusion coefficients, and NMR lineshapes and crystal orientation studies) at relevant operating conditions provide information that when complimented by molecular simulations can be extended to macroscopic material attributes for separations. In pursuit of these systematic investigations this dissertation includes the construction NMR instrumentation to observe the behavior of both liquid and gaseous adsorbents. Characterization of the translational motion of xylene molecules in MOF-5 through observation of the self-diffusion coefficients to develop understanding of motion of xylene molecules in

isotropic confinement. The investigation of these structure-property relationships via NMR in IRMOFs (iso-reticular MOFs) systems has lead to understanding the influence of the open-metal site pore chemistry on molecular transport of methane (CH_4) in an IRMOF, M_2(dobdc), where M is either the (Mg, Ni, or Zn) metal. NMR relaxometry conducted on CH_4 in this systems suggest a large difference in local density causes increase rotational correlations times. Diffusive diffraction behavior was observed at certain pressures in this family of materials and a kinetic Monte Carlo program was written in order to interpret the data. Finally, an international collaboration with the Prof. Blmich at RWTH Aachen was executed in order to expand the applicability of magnetic resonance methods for characterizing transport on more prototypical MOFs. These gradients must be considered for interpretation of relaxometry data.

This thesis is dedicated to failures. It is my strongest belief that only through experiencing failure, small or large, may we as individuals or a society grow to our true potential. My endurance of failure during the pursuit of this degree is owed to those who have nurtured my many facets of self and have shown me that above all your character is your most important legacy.

To Prof. Jeff Reimer, my adviser, there are not enough words; how grateful I am that you randomly decided to asked me to get coffee my first year. You have taught me to be more humble, and to see the immense value every individual has to offer.

To the Reimer Group members, my family away from home who challenged my mind, my perspective, and helped an endlessly anxious former perfectionist to see the glass as half-full.

To the Undergrads, Marty, Lucy, Yusu, Nathan and Aditya for your patience and dedication to our work as we faced endless challenges; but most of all for your trust freely given that motivated me to be worth its value.

To the educators...for literally teaching me to speak, to analyze, but most importantly to how to learn.

To my many mentors for ignoring my awkwardness and showing me kindness and respecting my ideas to help build a confidence of self.

To my Historically Black College and University, "Florida Agricultural and Mechanical University, 1887, what!" for teaching to to embrace my essence of my culture and showing the magical spectrum of blackness.

For my friends, first for making me recovery biscuits after what I thought was the most epic failure of my life, but more importantly, for hearing rhythm of my life and deciding to simply dance with me.

To my adoptive sister, Ashia, for the uncountable hours of pep talks, wine rants, coffee shop squatting and for challenging every belief I ever had just for the sake of argument teaching me the insane logic of a consistent level of skepticism.

To my siblings, Clashous and Victoria, for letting me read you textbooks, socializing me, and reminding me to laugh.

To my parents for never punishing my endless curiosity, even when it meant rationalizing decisions with a child and for showing me how to trust God find my strength in faith.

To God for giving me the tools, the people, and his love so that I may find peace in all my failures still to come.

Contents

Acknowledgments

I would like to acknowledge the contributions of collaborators in this work.

I would like to acknowledge Prof. Smit and the MolSim group members (Efrem Braun, Sudi Jawahery, Rocio Mercado) for providing computational support and lively discussions.

I would like to acknowledge Prof. Blumich for allowing to spend time with his group in Aachen, Germany and providing experimental support and guidance and his student Stefan Benders for introducing to the use of the spectrometers.

Chapter 1

Introduction: Magnetic Resonance Characterization of the Ideal Porous Media (MOFs)

1.1 Motivation

Investigating motion in Metal Organic Frameworks

As price of energy continues to rise due to the finite amount of carbon based fuels, efforts have been made to develop energy efficient technologies that make energy use more sustainable. A report that assessed US energy consumption showed that industrial processes account for 32 % of the total energy consumed[1]. Most chemical industrial processes, due to the complexity of the reaction pathways, yield substantial amounts of by products requiring chemical plants to be equipped with a unit operation dedicated towards the separation of the desired product(s). This cost of separation may account for up 30-80 % of the total cost of the chemical plant because separation processes consume large amounts of energy[2]. Chemical separation processes actually account for 10-15 % of the total energy consumption in the US. Thus participants in both chemical and petrochemical industries are motivated to develop more sustainable separation processes. Research efforts include goals to design novel materials that serve as a separation medium which lower the overall penalty of the process [1]. One avenue that is being explored, is the use of porous materials as adsorption media that efficatiously target particular chemical compounds. The development of these types of porous materials may also be useful for more niche applications like chemical sensing, catalysis, and/or gas storage[3, 4]. Metal-organic frameworks are a class of

porous materials that are being investigated for such use in adsorptive technologies. This is primarily due to their large surface areas, tunable surface chemistry, and diverse structures[5]. Metal-organic frameworks (MOFs) are composed of metal clusters and organic linkers coordinately bonded into a network that result in an open framework topology which is both mechanically robust and thermally stable. These novel porous materials can be modified via organic linker functionalization, transition metal type, and post-synthetic modification, often resulting in unprecedented degrees of separations selectivity for a variety of small molecules[6].

MOFs are actualized in many topologies and are often grouped by their structural similarities to each other. Many of the earliest discovered MOFs consisted of isotropic structures such as MOF-5 which is composed of tetrahedral zinc oxides bridged by a rod-like benzenedicarboxylate acid(bdc) linkers.[7] Later, open-metal site MOFs were introduced by researchers distinguished by the presence of chemically stable yet under-coordinated metal ion existing after removal of the synthesis solution. MOFs may also be classified by their similarities to other well-known porous media i.e. zeolitic imadazolate frameworks (ZIFs) whose secondary building blocks (tetrahedral zinc oxide clusters and imidazolate linkers) enables the mimicry of common zeolitic crystal topologies. Although MOFs were originally believed to be completely rigid, a subclass of flexible MOFs exist whose structures dynamically responds to different external stimuli by changing the pore size and/or shape. Traditionally the these materials are characterized for different adsorptive applications through common methods available to most chemical laboratories (i.e. BET surface area analysis, powder or single crystal x-ray diffraction, and adsorption isotherms). [6]

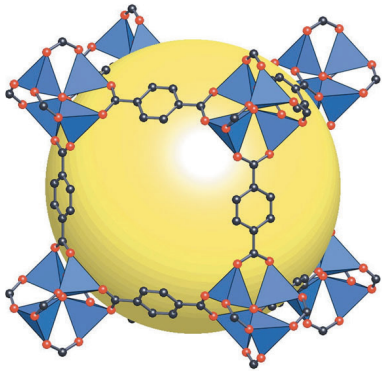

Figure 1: Schematic showing the metal organic framework most commonly referred to as MOF-5. The zinc oxide tetrahedral cluster are depicted in blue connected by the benzenedicarboxylate acid(bdc) organic linkers to form a cubic structure. The yellow sphere is include to emphasize the free pore volume. Figure taken from Ref. [7]

Although these characterizations are adequate for identifying potentially applicable MOFs amongst the hundreds of structures published yearly, the methods often yield very little definitive experimental evidence about the dynamics of the interactions between the adsorbate and the MOF; these interactions influence the overall performance of the material. Therefore, once a potential MOF is identified for a particular application, further analysis is accomplised

by using methods that capture the transport behavior to ostensibly understand how attributes like pore size, chemical function, and type of adsorbate molecule influence the performance as a separation medium. The study of transport or motion in porous materials, however, has been challenging for two reasons. [8] The first being that most previously investigated porous materials for adsorptive technologies (polymers and carbons) do not possess both long-range crystallinity as well as defined locations of the adsorptive sites with respect to that structure. Investgators are often challenged by having a well-defined crystal structure (e.g. zeolites) but are not capable of experimentally pinpointing the location of the charged ions that serve as the active sites. [9] Further while it is possible to understand the relative location of the adsorption sites on a polymer chain, the material does not exhibit a well-defined overall topology due to the semi-amorphous nature of polymers and their sensitivity to synthesis procedure. On the other hand MOFs are a porous materials where both the relative locations of the chemical affinity groups are well-defined and the material possess long-range crystallinity. In this thesis MOFs were treated as idealized porous media where observations of dynamics under systematic perturbations of the thermodynamic state improved the fundamental descriptors that govern the motion of small molecules under confinement. MOFs offer a unique opportunity for members of the porous media community to attempt to systematical investigate the subtleties of adsorbate-adsorbent interactions through the lens of adsorbate motion.

The second challenge in the application of porous materials for target small separations is the availability of experimental methodologies to characterize the adsorbate dynamics in porous materials. Common methods like permeation and breakthrough curves are actually performed on experimental time scales that contribute more information about inter-crystalline transport phenomenon than transport in the intracrystalline environment where researchers have the capability to change the chemical functionality and structure. [10] There are few techniques that exist to quantify motion on the length scale of the pore and then relate observables to the overall adsorptive performance. Typical macroscopic methods yield values of a Fickian diffusion coefficents or mass transfer coefficient that contain contributions that does not facilitate the isolation of intracrystalline effects. [11, 12].

A mass balance across transient porous crystalline pack bed is shown in (1.1), where the species i is a component in the gas phase, R is the ideal gas constant, T is the temperature, u is the superficial gas velocity, z is the distance into the packed bed along the adsorber, ρ is the the MOF density, η is the bed voidage, and $\bar{q}_i$ is the

average loading of the components with in each crystallite [11, 12].

$$\underbrace{\frac{1}{RT}\frac{\partial p_i}{\partial t}}_{\text{Accum.inOuletStream}} = \underbrace{\frac{1}{RT}\frac{\partial (up_i)}{\partial z}}_{\text{AmountinGasPhase}} - \underbrace{(1-\eta)\rho\frac{\partial \bar{q}_i}{\partial t}}_{\text{Accum.inAdsorbent}} \quad i = 1, 2, ..., n_{components} \tag{1.1}$$

The average loading of each crystal is determined by rate of accumulation in the crystal with time. The mass transfer phenomenon is best described by Fick's 2nd law, where the flux of the gas component into the porous material controls the rate of accumulate. The Maxwell-Stefan formulation of the intracrystalline transport diffusivity is used here to represent the adsorbate traveling through the medium, or adsorbent.[12]. Only a few methods that involve the collection of spatially and temporally resolved concentration data within a single crystallite may capture the atomistic meaning of these entities.[13, 14]

The research community has sought to employ magnetic resonance methods that quantify observables such as relaxation time constants, self-diffusion coefficients, and chemical spectra in the presence of interactions between adsorbates and MOFs. In the past few years, magnetic resonance techniques (i.e. relaxometry and diffusometry) have become more widely employed by the community for characterization of important adsorbate-adsorbent interactions.[15] Magnetic resonance has been employed in order to understand dynamics of adsorbed molecules in widely popular archetypes.[16] In this thesis I submit that a systematic characterization of basic inter- and intra-molecular interactions of adsorbates in porous materials will help to increase our understanding of how the structure of the MOF may be modified to increase favorable adsorbate-adsorbent interactions .

1.2 Phenomenological Introduction Nuclear Magnetic Resonance

After its initial discovery in the 1940's by notable figures such as Bloch and Purcell [17], nuclear magnetic resonance (NMR) began to emerge as an analytical tool that enabled the quantification of the molecular structure of organic molecules because of the dependence of spectral features on the local bonding environments of nuclei. Following the 1950's, the development of Hahn Echo[18] based pulse sequences has enabled magnetic resonance of porous media to become a robust tool that facilitates gathering unique insights and experimental perspectives for understanding structural features, complex adsorbate-adsorbate dynamics, and adsorbate-adsorbent interactions in porous materials. [15] NMR based investigations have led to understanding these

phenomena in both zeolitic and polymeric communities. The cohesive work of these groups when combined with molecular dynamics (MD) simulations and density functional theory (DFT) calculations, previously enabled the zeolitic community to better understand the effects of the framework's structure and surface chemistry on it's macroscopic adsorption and transport properties. Before delving into the intricacies of NMR in porous media, let us first explore the most basic concepts, chemical shift, relaxation, and diffusion that led to NMR's broad use in complex systems.

1.3 Concepts of Magnetic Resonance

The phenomenon of NMR is based on the principle that when a nucleus with a spin $\vec{I}$ is placed in an overall magnetic field it will begin to process at a frequency known as the Larmor frequency,

$$\omega_0 = B_0 \frac{\gamma_I}{2\pi}. \tag{1.2}$$

Here gyromagnetic ratio, γ, is related to the intrinsic value of the spin magnetic moment, and B_0 is the strength of the static magnetic field, usually aligned with the z-axis. The time evolution of the magnetic moment associated with the ensemble of spins is described by the phenomenological Bloch-Torrey model, where all individual magnetic moments sum to a total magnetization vector, $\vec{M}$, i.e. the macroscopic magnetization. In 1946 Bloch [17] described the evolution of the magnetization vector by identifying that magnetic moments in the presence of a short, pulsed orthogonal applied magnetic field, will feel a torque, $\vec{M} \times \vec{B}$, causing the direction of the magnetic moment to become unaligned with the overall field direction. In the laboratory frame, this magnetization vector is always precessing, see Fig. 2 at the Larmor frequency, ω_0. This magnetic moment is best visualized in a rotating frame precessing at the same frequency of the spin. This new rotating frame vector is composed of x, y, and z components, however hardware limitations allow detection of only the projection of this vector into the transverse (x-y) plane. The evolution of $\vec{M}$ is actually what is described by the Bloch-Torrey equation, eq 1.3 [19]

$$\frac{d\vec{M}(t)}{dt} = \vec{M}(t) \times \vec{B}(t)\mathbf{R}(\vec{M}(t) - \vec{M}(0)) - \nabla \mathbf{D} \nabla \mathbf{B}_{ext} \tag{1.3}$$

modified to include the effects of both relaxation, representing by the tensor $\mathbf{R}$, and diffusion represented by $\mathbf{D}$. This $\vec{M}$ is manipulated during an NMR experiment through generation of instantaneous magnetic fields through radio frequency (RF)

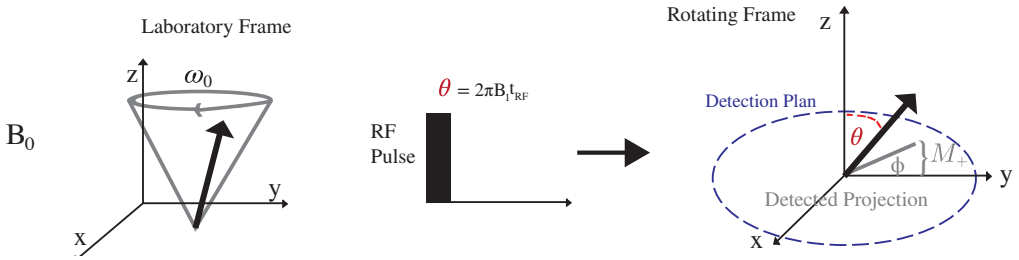

Figure 2: The magnetization vector in the laboratory frame before and after excitation by an RF pulse of the B_1 field. At the right is the projection into the $x-y$ plane.

pulses, $\vec{B_1}$, applied at the ω_0 frequency. In equation 1.4

$$\vec{B}(t) = \vec{B}_0 + \vec{B}_1(t) \tag{1.4}$$

an RF coil generates the B_1 field perpendicular to $\vec{B}_0$ and the same coil is used to detect $\vec{M}$. The sum of the phase, ϕ, and magnitude, M of all the spins in the x-y plane is detected. Although, $B_1 \ll \vec{B}_0$, the torque of $\vec{B}_1$ is enough to disturb the spins from equilibrium.

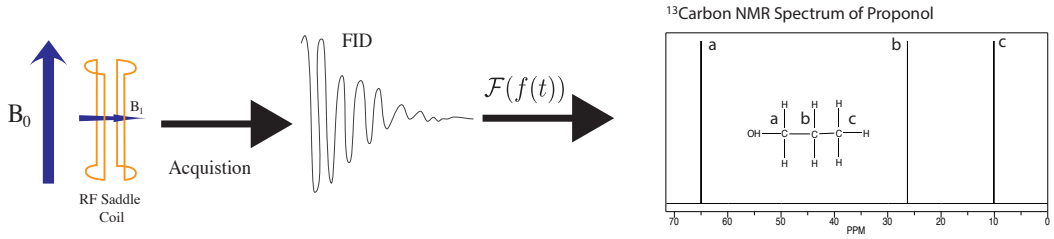

Figure 3: Schematic showing the basic saddle coil that produces a B_1 effective field perpendicular to the overall applied field, the FID acquired by such coil in the time domain (middle), and the Fourier Transform of yielding the NMR spectrum for liquid propanol(right).

The resulting $\vec{M}$ after the RF pulse is now

$$\vec{M}(t) = M_0 \begin{pmatrix} 0 \\ sin(\theta) \\ cos(\theta) \end{pmatrix} \tag{1.5}$$

where θ is the tilt angle of the pulse, $\theta = t_{RF} B_1 2\pi$, where t_{RF} is the duration of the pulse. When the vector is tilted into the x-y plane, it is detectable in the laboratory frame as an oscillating magnitude. We consider the x and y magnetization to be equivalent and instead define the M_+ as the transverse magnetization with a phase ϕ relative to the phase of the detector. This oscillating magnitude is recorded as a Fourier induction decay, FID, in the time domain (Fig 3) and an application of a Fourier Transform allows the data to be resolved into the detected precessing frequencies. Local variations in the magnetic field surround the observed spin (for example bonding causing a static local magnetic field environments) yields to an *effective* B_0, or B_{eff}. This is demonstrated in Fig 3 where the bonding environment of the carbon nuclei in propanol cause three distinct "shifts" from the resonance frequency. These shifts are typically measured in parts per million (ppm) of the applied field.

$$\delta[inppm] = \frac{\omega_{reference} - \omega_{obs}}{\omega_0} \tag{1.6}$$

.

Upon being disturbed from equilibrium by an RF pulse $\vec{M}(t)$ will return to its equilibrium magnetization $\vec{M}(0)$ as given by Eq. 1.3. In the absence of magnetic field gradients, the return to equilibrium is determined by the relaxation tensor R

$$R = M_0 \begin{pmatrix} \frac{1}{T_2} & 0 & 0 \\ 0 & \frac{1}{T_2} & 0 \\ 0 & 0 & \frac{1}{T_1} \end{pmatrix} \tag{1.7}$$

Here the relaxation time constants are longitudinal relaxation time (T_1) (spin-lattice) and transverse relaxation time (T_2) (spin-spin). The complex sum of the x and y components is referred to as the transverse magnetization, $M_+ = M_x - iM_y$, (Fig 2 the detectable magnetization) and relaxes back to zero at equilibrium. M_z is referred to as the longitudinal component and expected to relax back to the value of M_0. It is important to note that the detectable magnetization may also be written as $M_+ = M * e^{i\phi}$, where ϕ is the phase associated with the projection in the x-y plane.

Figure 4 depicts the role T_1 plays in directing the evolution of magnetization in the longitudinal or z direction, whereas T_2 (5) determines the rate of change of the magnetization present in the x-y plane as it decays to zero.

1.4 Relaxation and Molecular Motion

It is well understood that relaxation processes are driven by various physical mechanisms. The the spin-lattice relaxation dictates the time it takes for the spins to

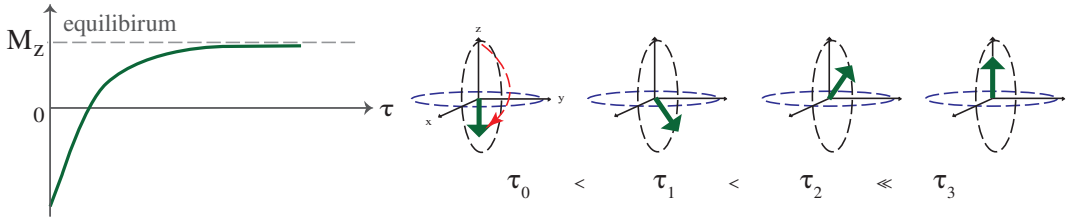

Figure 4: The magnetization vector relxaing in the absence of magetic field gradients back to equilibrium with increasing time intervals, τ.

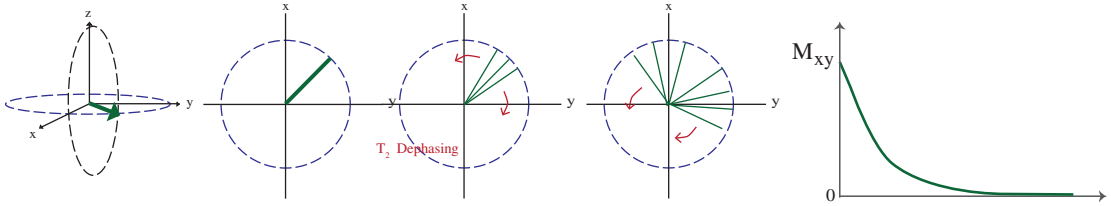

Figure 5: The $\mathbf{M}_+$ magnetization in the x-y rotating frame after excitation by an RF pulse as it experiences T_2 relaxation with increasing τ.

exchange energy with the surrounding reservoir, e.g. the lattice. This process is an energy absorbing process in which the exchange is moderated by both molecular rotational motion and proximity of all spins to other local fields. Motion of the neighboring nuclei on the same molecule or nearby molecules may serve as the source of a fluctuating local magnetic field that drives magnetization to its equilibrium state. An early model developed for pure liquids is Bloembergen Parcell Pound (BPP) theory[20] whose authors showed that for pure liquids there were two main contributions relaxation to T_1 relaxation: inter-molecular fluctuating nuclear dipole fields that are associated with other molecules, and fluctuating fields contained within the same molecule as the spin. These rates are represented in this model by the Fourier transforms of the angular auto-correlation functions of the spin-pair vectors. The authors showed that for pure simple liquids, relaxation may also couple nucelar spin angular momentum with molecular spin rotation mechanisms may be correlated with the rotational diffusion coefficient of the spin bearing molecule. Following investigators have developed more specific models for limited physical systems to probe the molecular rotational motions and their associated correlations times to facilitate understanding motion. The activation energy associated with rotational motion may be calculated for adsorbates in MOFs [21] when the contribution from

spin rotation dominates the relaxation. The observed value T_1 may also be associated with the fluctuating fields from the surrounding spins, thus it is common practice in many protein studies to asses binding strength through the observations trends in T_1 with loading and temperatures [22]; similar theories are applicable in MOF-adsorbate systems.

Transverse relaxation, T_2, (spin-spin relaxation), is a dominated by spin interactions and moderated by translational motion. In this case the local fields, whether intra- or inter- molecular, are considered "static," while each spin interacts with these fields by motion. In most cases $T_2 < T_1$ although both are affected by motion.

In the absence of relaxation and in the presence of a gradient in the magnetic field, $\nabla\mathbf{B}$, diffusion will return $\vec{M}(t)$ back to its equilibrium state, where $\mathbf{D}$ is the tensor form of the self-diffusion coefficient of the spin bearing molecule. The systems studied in the following chapters will consider working within the bounds of the Maxwell Stefan definition of the self diffusivity, $D_{s_{ij}}$, where the spin bearing molecule i diffuses in the medium j. In the case of the pure liquid , i=j, in the case of adsorbates in porous media it is understood that $i \neq j$, and instead i=adsorbate and j = adsorbent, the symbol D_s is used and is often referred to as the apparent self diffusivity. Thus the practice of NMR Diffusometry is the use of crafted gradient fields to control the evolution of $\vec{M}(t)$ and extract information about the self-diffusivity of the spin bearing molecule.

1.5 Application of Magnetic Resonance in Porous Media

Porous materials are extremely complex, and early on it was found that liquids in porous materials experience extremely fast relaxation. In short, magnetic resonance in porous media would have been impossible without the contributions of Prof. Hahn, who observed that one could re-phase or reverse the signal lost due to de-phasing in the transverse plane with the pulse sequence, coined "Hahn Echo". This later developed into the Carr-Purcell-Meiboom-Gill (CPMG) sequence, Fig 6, where a rapid succession of uniformly spaced echo times enable rapid refocusing. Although adding a CPMG train usually sacrifices the spectral resolution and weights any observable by T_2, the additional signal from summing the train significantly decrease acquisition time and enables many 2-D experiments.[18, 23]

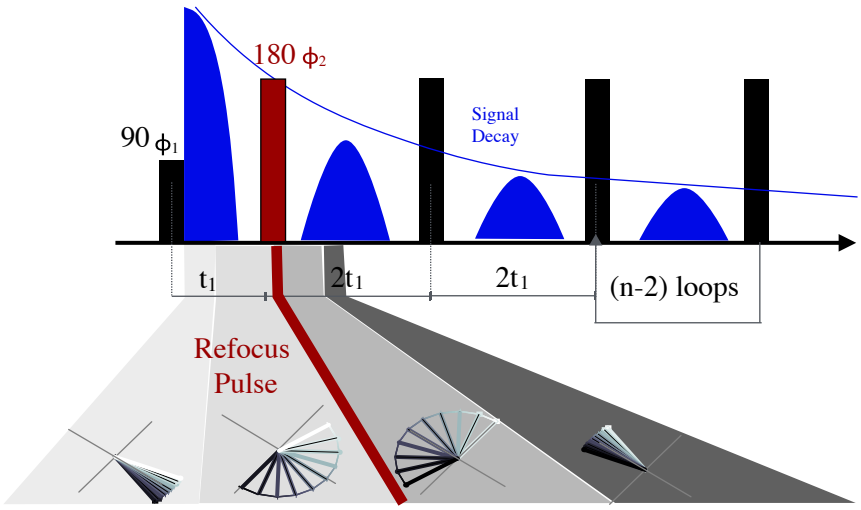

Figure 6: Schematic depiction of the CPMG sequence. The signal decay and resulting echos are shown in blue, where a depiction of coherence of the individual moments of the spins in the x-y detection plan is depicted before and after the refocusing π pulse. The demonstrates how repeated π pulses serve to refocus the coherence of the spins rate of the spacing between pulses.

Diffusometry: Diffusion in Porous Media

Free Diffusion

Although transport diffusivity, D_T, is most commonly used to described the motion of adsorbates in porous media, direct measurements of this phenomenological diffusivity are challenging and rare. Let us recede from the framework of restricted diffusion as presented in 1.1 and consider first the framework of free diffusion. Diffusion is a stochastic process driven by random thermal motion of molecules, i.e "Brownian motion," and in the case a unrestricted gas or liquid molecules Einstein's self-diffusivity is defined as the mean square displacement (MSD) of a molecule in a set amount of time, [24].:

$$\mathbf{D}_s = \frac{\langle(\mathbf{r}_1 - \mathbf{r}_0)^2\rangle}{6(t_0 - t)} \tag{1.8}$$

A probabilistic description of the mean square displacement is of better use for understanding the NMR methodologies. The concept of the probabilistic diffusion propagator introduced, encompasses the conditional probability of finding a molecule initially located at $\mathbf{r}_0$, that the same molecule would be located at $\mathbf{r}_1$ at some future

time t, $P(\mathbf{r}_0, \mathbf{r}_1, t)$. Thus the mean-squared displacement (MSD) may be calculated as the integration of the product of probability, overa all possible starting locations and all possible displacement values.

$$\langle(\mathbf{r}_1 - \mathbf{r}_0)^2\rangle = \int_{-\infty}^{\infty} (\mathbf{r}_1\mathbf{r}_0)^2 \rho(\mathbf{r}_0) P(\mathbf{r}_0, \mathbf{r}_1, t) d\mathbf{r}_o d\mathbf{r}_1 \tag{1.9}$$

In its truest form $\mathbf{D}_s$ is a tensor of Cartesian values, yet when diffusion is isotropic in for most liquids, it simplifies to Einstein-Stokes description.

Gradients and Phase Decoherence

Now let us recall the Bloch-Torrey equations, Eq 1.3 which show that in the absence of relaxation $\vec{M}$ is attenuated by diffusion in gradient fields, ∇B_{ext}. Although the overall magnetic field, B_0, is homogeneous, gradient coils may be used to introduce linear fields through the application of a gradient pulses to the sample volume. For the simplicity of visualization, let us consider the application of a gradient in the z-direction to a control volume. In the case of a linearly changing magnetic field, the z-gradient is a constant value, $G[\frac{Gauss}{mm}]$. This implies that the alignment magnetization vectors of the observed ensemble average of spins is no longer coherent but is a function of the location of the spin bearing molecule along the z axis. Thus each spin, according to its, z-location will process a slight faster or slower $\omega_0(z)$ the instant a gradient pulse is applied. How much faster or slower the procession frequency is depends upon the pulse duration, δ and the magnitude of the G. Fig 7 demonstrates the effect of a z-axis gradient pulse on the magnetization vector of spins. A gradient pulse causes organized decoherence of the spin magnetization vectors in the transverse plane, or effectively each spin vector feels phase shift, $\phi(z,t)$. This pulse is considered short and almost instantaneous and the resulting "torque" on the magnetization vector will manifest phase differences between spatial distributed spins in the direction of the applied gradient. The increment in the value of $\phi(z,t)$, which can vary between 0 and 2π, is detected as increasing decoherence of transverse magnetization.

$$\begin{aligned} \vec{M}(r(z), t+\delta) &= (B_0 + B_{app}(r(z), \delta))\frac{\gamma}{2\pi} \\ &= (B_0 + G(\delta, r) * r)\frac{\gamma}{2\pi} \\ &= \vec{M}_0(r_0, t_0) + \phi(G, \delta, z) \end{aligned} \tag{1.10}$$

The Measurement of the D_s

In the absence of diffusion, the effects of the gradient pulses are essentially reversible. The accumulated decoherence may be reversed by applying the same pulse in an opposite direction.

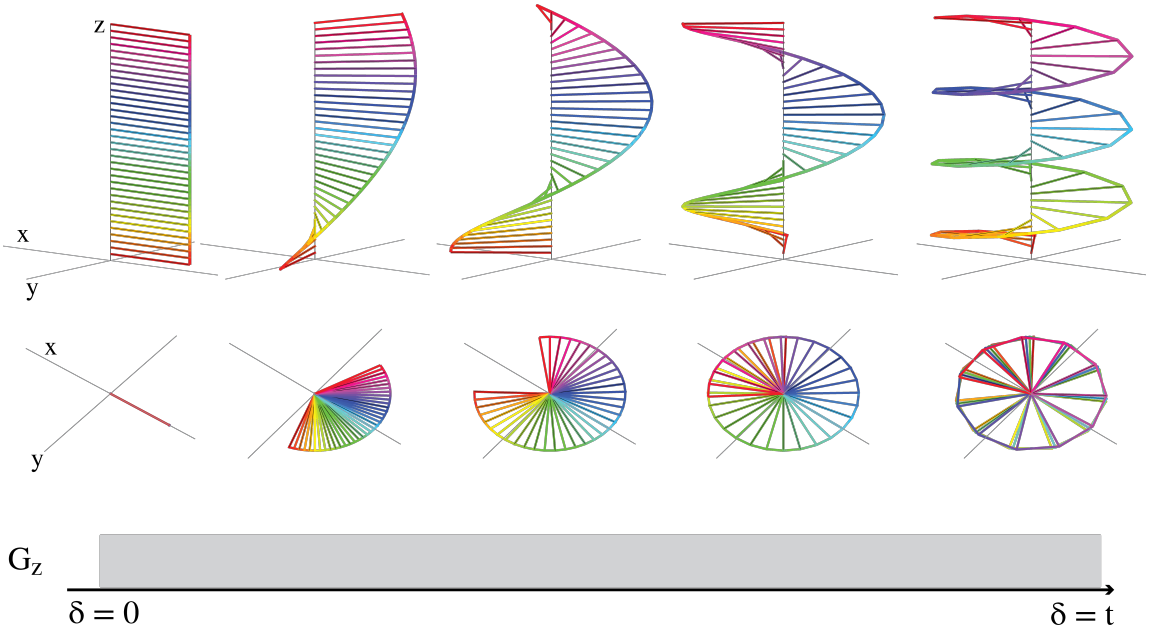

Figure 7: Showing the magnetization vectors spatially distributed along the z-axis of the sample as the length of the gradient pulse increases. Relaxation effects are neglected

$$\begin{aligned}\vec{M}(r(z),\delta+t_f) &= \vec{M}_0(r(z_0),t_0)+\phi_+(G,\delta,z|_{t_0}=z_0)-\phi_-(-G,\delta,z|_{t_f}=z_f)\\ &\vec{M}_0(r(z_0),t_0)+(if\, z_f=z_0 than \phi_+-\phi_-=0)\\ &=\vec{M}_0(r(z_0),t_0)\end{aligned} \tag{1.11}$$

In the presence of diffusion,however, the observed signal will decay as a function of the length of the pulse δ, the experimental time allocated for diffusion, $\Delta t = t_f - t_0$, magnitude of the applied pulse, G, and the difference in the z position for each spin, $z_f - z_0$,

$$\begin{aligned}\vec{M}(r(z),t_0+\delta+t_f) &= \vec{M}_0(r(z_0),t_0)+\phi_+(G,\delta,z_0)-\phi_-(-G,\delta,z_f)\\ &=\vec{M}_0(r(z_0,t_0)+\Delta\phi(G,\delta,t_f-t_0,z_f-z_0)\end{aligned}. \tag{1.12}$$

When the signal attenuation is considered over an ensemble-average of spins with the displacement in any direction (x,y, or z), Stejskal and Tanner [25] showed that the signal attenuated exponentially with the MSD over the experimental diffusion time and a function of all the other parameters. They coined this experiment a Pulsed-Field-Gradient Spin Echo (PFGSE) Sequence. They proved that by varying the experimental controls of the gradient pulse, G and δ, and holding the diffusion time, Δ, constant, one could sample the Fourier transform of the probability distribution function of a spin experiencing a certain amount of displacement within a known amount of time. Described by a Gaussian, the mean of this distribution is directly proportional to Einstein's self-diffusion coefficient (D_s), making the signal attention proportional to

$$\frac{M_{G,\delta,\Delta}}{M_0} \propto exp(-G^2\delta^2\Delta D_s) \tag{1.13}$$

.

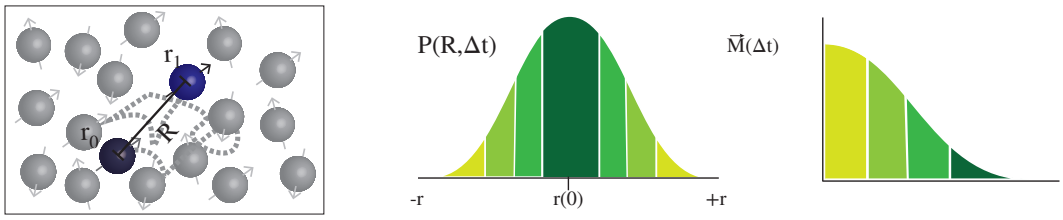

Figure 8: Showing the magnetization vectors spatially distributed along the z-axis of the sample as the length of the gradient pulse increases. Relaxation effects are neglected.

Brief Description of Internal Gradients

Many variations of the"Hahn echo", component of this sequence exist for the purpose of minimizing the contributions from the relaxation tensor to the signal attenuation. In the case of applications to porous media, it is acceptable to employ a variation of this reffered to as Stimulated Echo pulse sequences [26]. These sequences minimize the T_2 contribution to the signal attenuation by storing the magnetization moment along the z-axis during the Δ and shortening the overal time spent with the magnetization in the tranverse plan to be $<T_2$.[27]. In addition to applications of pulsed gradients, the same mathematical description may be applied to systems measured under a constant gradient field where the amount of time experiencing the static gradient in the transverse plane is varied to attenuate the signal. [28] In most experiments,

then the influence of the gradient is controlled by either the application of pulse or by specifying the time in the presence of a constant applied magnetic field gradient (∇B).

Now that is is clear how NMR may quantify the D_s, it is important to note that relaxation attenuation may occur when an internal magnetic field gradient (g_{int}) is present. The g_{int} are areas of magnetic susceptibility contrast that distort the overall field felt by the magnetic moment of the spin on a diffusing molecule. In most cases these small distortions are negligible and do not contribute to signal attenuation. However, if the magnitude of the g_{int} is large, and the time spent sampling these spatially varying internal gradients is also large, additional attenuation may occur during a relaxation experiment due to diffusion through internal field gradients. [29, 30] . Understanding this phenomenon has allowed the development of several NMR techniques such as pores size characterization [31] and susceptibility contrast imaging [32] that use the difference in the detected relaxation values due to the effects of diffusion in g_{int} as indicators. Previously, such phenomena were not explored in MOFs but these details may be found in Chapter 3. In general, when investigating porous media imbibed with fluids it is important to consider the affects of internal gradients on the observed parameters.

References

(1) Angelini, P.; Armstrong, T.; Counce, R.; Griffith, W.; Klasson, T.; Muralidharan, G; Closset, G.; Keller, G.; Watson Disclaimer, J. *Materials for Separation Technologies: Energy and Emission Reduction Opportunities*; tech. rep.; US Department of Energy, 2005.

(2) Cussler, E. L.; Dutta, B. K. *AIChE J.* **2012**, *58*, 3825–3831.

(3) King, C. J., *Separation processes*, 2nd Edition; 13: 978-0-486-49173-8; Dover Publications: MIneola, New York, 2013.

(4) Cunningham, R. E.; Williams, R. J. J., *Diffusion in gases and porous media*; Springer: Boston, MA, 1980; Vol. 1.

(5) Czaja, A. U.; Trukhan, N.; Müller, U. *Chem. Soc. Rev.* **2009**, *38*, 1284–1293.

(6) Meek, S. T.; Greathouse, J. a.; Allendorf, M. D. *Adv. Mater.* **2011**, *23*, 249–67.

(7) Li, H.; Eddaoudi, M.; O'Keeffe, M.; Yaghi, O. M. *Nature* **1999**, *402*, 276–279.

(8) Li, J.-R.; Kuppler, R. J.; Zhou, H.-C. *Chem. Soc. Rev.* **2009**, *38*, 1477–1504.

(9) Krishna, R.; Baur, R. *Sep. Purif. Technol.* **2003**, *33*, 213–254.

(10) Kärger, J.; Caro, J.; Cool, P.; Coppens, M.-O.; Jones, D.; Kapteijn, F.; Rodríguez-Reinoso, F.; Stöcker, M.; Theodorou, D.; Vansant, E. F.; Weitkamp, J. *Chem. Eng. Technol.* **2009**, *32*, 1494–1511.

(11) Scholes, C.; Others *Chem. Aust.* **2012**, 34.

(12) Krishna, R.; Long, R; Long, J. R. *J. Phys. Chem. C* **2011**, *115*, 12941–12950.

(13) Schemmert, U.; Kärger, J.; Weitkamp, J. *Microporous Mesoporous ...* **1999**, *32*, 101–110.

(14) Gueudré, L.; Binder, T.; Chmelik, C.; Hibbe, F.; Ruthven, D. M.; Kärger, J. *Materials (Basel).* **2012**, *5*, 721–740.

(15) Barrie, P. J. *Annu. reports NMR Spectrosc.* **2000**, *41*, 265–316.

(16) Stallmach, F.; Gröger, S.; Künzel, V.; Kärger, J.; Yaghi, O. M.; Hesse, M.; Müller, U. *Angew. Chem. Int. Ed. Engl.* **2006**, *45*, 2123–6.

(17) Bloch, F. *Phys. Rev.* **1946**, *70*, 460–474.

(18) Hahn, E. L. *Phys. Rev.* **1950**, *80*, 580–601.

(19) Torrey, H. C. *Phys. Rev.* **1956**, *104*, 563.

(20) Bloembergen, N.; Purcell, E. M. E.; Pound, R. R. V. *Phys. Rev.* **1948**, *73*, 679–712.

(21) Kong, X.; Scott, E.; Ding, W.; Mason, J. a.; Long, J. R.; Reimer, J. a. *J. Am. Chem. Soc.* **2012**, *134*, 14341–4.

(22) Craik, D. J.; Higgins, K. A., *NMR Studies of Ligand-Macromolecule Interactions*, 1989; Vol. 22.

(23) Burstein, D. *Concepts Magn. Reson.* **1996**.

(24) Einstein, A **1956**.

(25) Stejskal, E. O.; Tanner, J. E. *J. Chem. Phys.* **1965**, *42*, 288–292.

(26) Hürlimann, M. D.; Griffin, D. D. *J. Magn. Reson.* **2000**, *143*, 120–135.

(27) Cotts, R. M.; Hoch, M. J. R.; Sun, T; Markert, J. T. I. *J. Magn. Reson.* **1989**, *266*, 252–266.

(28) Casanova, F.; Perlo, J., *Single-Sided NMR*; Casanova, F., Perlo, J., Blümich, B., Eds.; Springer Berlin Heidelberg: Berlin, Heidelberg, 2011.

(29) Mitchell, J.; Chandrasekera, T. C. *J. Chem. Phys.* **2014**, *141*, DOI: 10.1063/1.4903311.

(30) Mitchell, J.; Chandrasekera, T. C.; Gladden, L. F. *J. Chem. Phys.* **2013**, *139*, DOI: 10.1063/1.4818806.

(31) Song, Y.-Q. Q. *Concepts Magn. Reson.* **2003**, *18A*, 97–110.

(32) Shiroishi, M. S.; Castellazzi, G.; Boxerman, J. L.; D'Amore, F.; Essig, M.; Nguyen, T. B.; Provenzale, J. M.; Enterline, D. S.; Anzalone, N.; Dörfler, A.; Rovira, À.; Wintermark, M.; Law, M. *J. Magn. Reson. Imaging* **2015**, *41*, 296–313.

Chapter 2

Translational and Rotational Motion of C8 Aromatics Adsorbed in Isotropic Porous Media (MOF-5): NMR Studies and MD Simulations

2.1 Abstract

We combined nuclear magnetic resonance (NMR) and molecular dynamics (MD) simulation to study xylene behavior in MOF-5, probing the effects of adsorbate geometry in a weakly interacting model isotropic metal-organic framework (MOF) system. We employed NMR diffusometry and relaxometry techniques at low field (13 MHz) to quantify the self-diffusion coefficients (D_s) and the longitudinal relaxation times (T_1) of xylenes in MOF-5 as a function of temperature at the saturated loading for each xylene. These experiments reveal the translational motion activation energies to be 15.3 kJ mol^{-1}, 19.7 kJ mol^{-1} and 21.2 kJ mol^{-1} and the rotational activation energies to be 47.26 kJ mol^{-1}, 12.88 kJ mol^{-1} and 11.55 kJ mol^{-1}for the (p-,m-,o-) xylene isomers, respectively. Paraxylene exhibits faster translational motion, yet shows four times the activation energy barrier for rotational motion vis-à-vis the other isomers. MD simulations performed on these model systems corroborate the findings for paraxylene and suggest that paraxylene has the lower free energy barrier for hopping away from its binding sites, yet has the slowest rotational motion in the plane of the xylene molecule.

2.2 Introduction

MOFs are a type of porous media under investigation for applications that require molecular specificity[33]. Since the initial discovery of MOF-5 (also known as IRMOF-1),[34] this novel class of materials has been explored for potential use in gas separation and storage, selective catalysis, and numerous other industrial applications. Targeted design and synthesis [35] enables modularity in MOFs achieving highly desired adsorbent characteristics.[8, 36] More recently, MOFs have been investigated for many liquid separation processes that requires a distinctive difference in the transport behavior of small molecules.[37]

To determine the suitability of these adsorbents for particular applications, transport phenomena are commonly investigated by performing macroscopic measurements (e.g. breakthrough measurements) that characterize effective mass transport values containing contributions from both the intercrystalline and the intracrystalline regimes[10]. To gain insight into the mechanisms that determine these macroscopic measurements, molecular-scale interactions need to be measured. In particular, MOFs offer the nanoporous media community a unique opportunity to improve our understanding of how adsorbed molecules move in a confined spaces since both the topology and the chemical affinity is well-defined.[38] Although MD simulations have been instrumental in developing a physical description of adsorbate motion in porous media, there are very few experimental studies on motional dynamics of the adsorbed molecules that can be used to validate these findings.

Many researchers employ NMR based techniques to quantify the self-diffusion coefficients in an effort to understand translational motion. The NMR longitudinal relaxation times are analogous to the self-diffusion coefficients,[16] in quantifying rotational motion of adsorbates in MOF systems.[39–42] Most of these studies have focused on determining differences between strongly and weakly adsorbed molecules, where stark differences in the observed self-diffusion coefficient and longitudinal relaxation time are used to understand motion and selectivity. [41, 42]

The separation of xylene isomers poses a lucrative scientific challenge, as distillation of these isomers accounts for a significant amount of global energy consumption.[43] Composed of a conjugated ring perturbated by two methyl groups, xylene isomers have similar kinetic diameters (less than 1 Å differences) and similar chemical interaction energies which makes the design of a selective adsorbent difficult. The selectivity of MOFs such as MIL-47[44–46] and MIL-53 [47–50] for xylene isomers has been studied and attributed slectivity to framework anisotropy that affects π-π stacking, which was identified as the dominant type of host-guest interaction. Macroscopic breakthrough measurements at high temperature (553 K) and pressure (1.2 bar) were used to

determine transport intracrystalline diffusivities of xylenes in MOF-5 and showed that the vapor phase paraxylene diffused two times slower than the other isomers. [51] Previous descriptions of how C8 aromatics diffuse in a porous environment postulate that entropy may play a greater role in determining the molecular mobility,[52–55] yet present very little systematic experimental evidence.

We have chosen to employ magnetic resonance methods to quantify D_s as a characterization of translational motion and NMR relaxometry to probe the local rotational motion of adsorbed xylene isomers in the MOF-5 framework. We explore how subtle geometric differences in the xylene isomers are manifest in translational and rotational motion. To further analyze the interplay between rotational and translational motion, we conduct MD simulations to calculate D_s, spatial probability distributions, rotational diffusion coefficients, and relative orientations of the xylene isomers in MOF-5.

2.3 Methods

MOF-5 Synthesis and Characterization

MOF-5 was synthesized by preparing a 3:1 mixture of zinc nitrate hexahydrate and 1,4-benzenedicarboxylic acid (Sigma Aldrich chemicals, 99.95 % purity) in 100 mL of diethylformamide (DEF) and heating for 72 hours at 90 °C, resulting in an typical crystal size of 425 µm. Solvent exchanges from DEF to dry dimethylformamide (DMF) were followed by solvent exchanges from DMF to dry dichloromethane (DCM) in preparation for activation. After solvent exchange, powder x-ray diffraction spectra were measured at room temperature using a D8 Discover GADDS Powder XRD (Appendix A) and nitrogen (Praxair, 99.999 %) adsorption isotherms were collected using a Micromeritics TriStar 3000 BET instrument determined the BET surface area of the crystals to be $3565\,\mathrm{m^2\,g^{-1}}$. A flow of argon gas at a temperature of 150 °C degassed the samples overnight. Afterwards a 425 µm sieve separated approximately 100 mg of the larger crystals, which were activated overnight at 150 °C and 10 mtorr of vacuum in a flame-dried 5 mm glass NMR tube.

Ex-Situ NMR Preparation and Measurements

After activation, the sample was dosed with a predetermined microliter amount of high purity degassed anhydrous xylenes purchased from Sigma Aldrich. NMR spin counting methods (7.4 T magnet using a Tecmag Discovery Magnet with a 5 mm Solid State NMR MAS Doty probe), as well as gravimetric methods, yielded loadings of (49 m to 56 molecules/unit cell) for each xylene isomer. These loadings ensure that

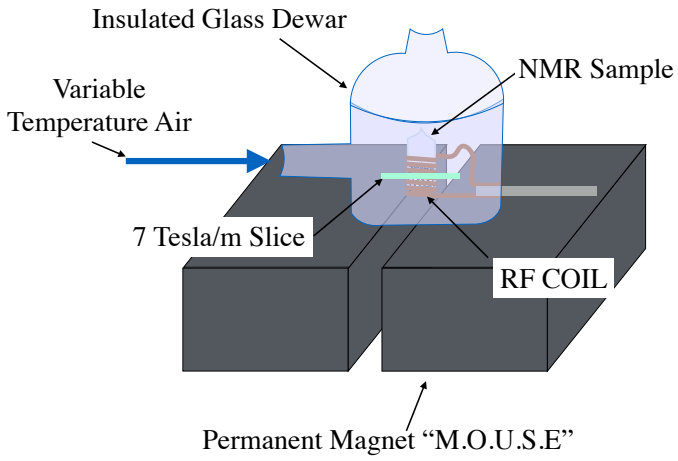

Figure 1: A schematic representing the custom homebuilt probe and temperature control setup used to make measurements. A volumetric coil is centered in the 1 mm selective slice inherent to xylene. A glass dewar was placed on top of the permanent magnet and was used to insulate the sample and electronics from the environment.

all adsorbed xylene molecules were in the high-density liquid-like phase based on theoretically-determined vapor-liquid phase diagrams provided previously[56]. The samples were flame sealed using a cold bath and liquid nitrogen, giving a minimal headspace of approximately 0.018 cm^3. The linear strayfield of a 0.3 T single sided magnet[57] equipped with a temperature controlling dewar was used for all NMR experiments (Fig. 1). The magnet field gradient strength was confirmed to be 7 $T\,m^{-1}$ through liquid diffusion calibrations. In order to increase sensitivity we constructed a home built probe using a solenoid copper coil oriented perpendicularly to the magnetic field direction, combined with a remote tuning box (Fig. 1). A Magritek Kea II Spectrometer was used with Prospa® operating software for the data acquisition. Power modulation was used to control the pulsed angle during all experiments.

The CPMG sequence[58] was used to measure the transverse relaxation time (T_2), as shown in Fig. 2A. Further basic pulse sequences employed a CPMG acquisition train. The Saturation Recovery pulse sequence (Fig. 2B) was used to measure the longitudinal relaxation time constant, T_1. A constant gradient stimulated echo (STE) pulse sequence with a CPMG acquisition and phase tables[28] (Fig. 2C) were used to determine the apparent D_s. These were interpreted as the intracrystalline

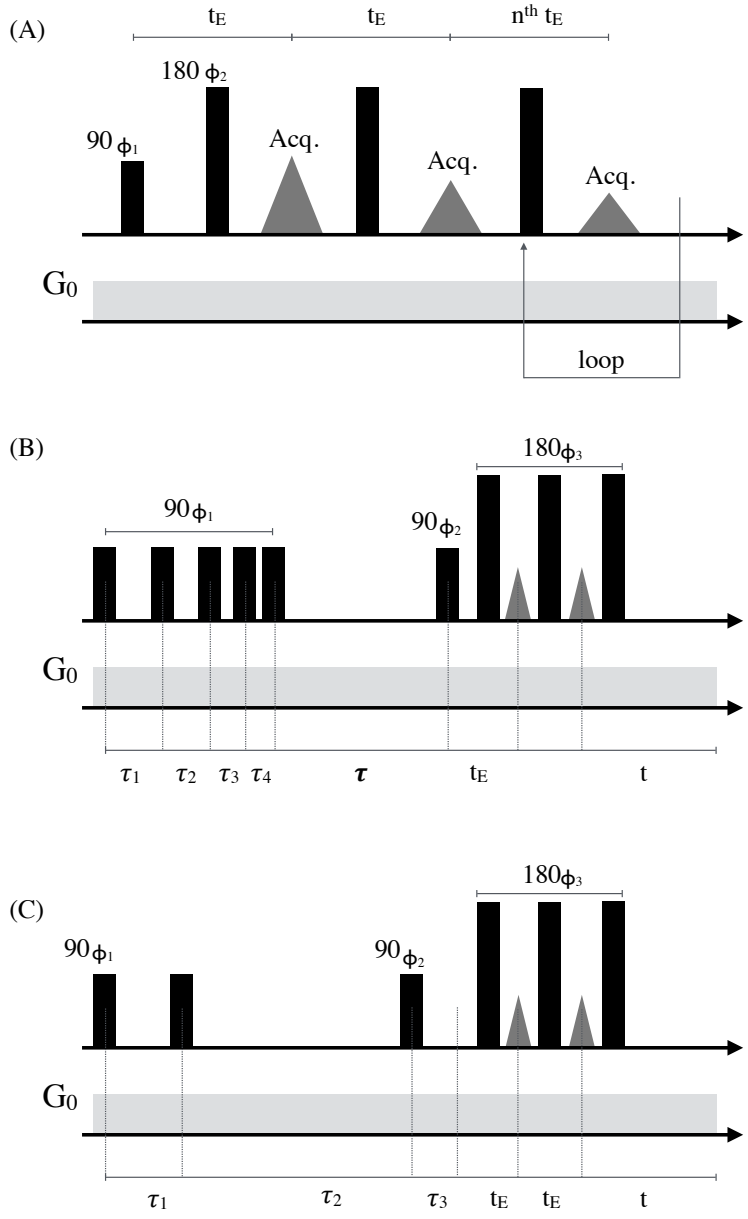

Figure 2: The standard NMR schematic for (A) the Carr-Purcell-Meiboom-Gill (CPMG) pulse sequence, (B) the Saturation Recovery pulse sequence with CPMG acquisition for inhomogeneous fields and (C) the Stimulated Echo sequences with CPMG acquisition for inhomogeneous fields.

Table 1: Loadings used in the MD simulations in units of molecules per unit cell.

Temperature (K)	o-xylene	m-xylene	p-xylene
270	54	53	53
280	53	53	53
290	53	51	51
300	52	50	50

diffusivities due to the large crystal size (450 µm) and small diffusion time, τ_2, (10 ms to 100 ms) chosen. This sequence has been shown to minimize decoherence of the signal due to transverse relaxation by storing the signal along the z-axis during the experimental diffusion time. During this storage interval, the signal experiences negligible longitudinal relaxation. The resulting signal was T_2-corrected during post-processing for the transverse relaxation experienced during the intervals of τ_1 and τ_3. The signal intensity as a function of τ_1 was analyzed using Numerical Non-Negative Linear "Inverse" Laplace Transformation (NNL) with Tikonov regularization to yield a spectrum of self-diffusion coefficients.[28, 59] This algorithm was provided with the Prospa® software from Magritek.

Molecular Dynamics Simulation Details

Molecular dynamics simulations were conducted with LAMMPS[60] in the NVT ensemble using a timestep of 0.5 fs, the Nosé-Hoover chain thermostat[61, 62] and a rigid-body time integrator [63]. The Lennard-Jones potential, shifted and truncated at 12.0 Å, was used to describe dispersive interactions. Framework atoms were modeled with a previously published force field [64], adsorbate molecules were modeled with the TraPPE force field,[65] and Lorentz-Berthelot mixing rules were used to calculate cross-interactions; this force field has been shown to provide good agreement with experimental diffusion coefficients of small aromatic molecules in MOF-5.[64] As the TraPPE models do not have partial charges, Coulombic interactions were not calculated. The framework was assumed to be rigid since it has been shown[66] that framework flexibility does not have an effect on adsorbate diffusion in MOF-5. and the experimental crystal structure[67] was used.

The frameworks were loaded with guest molecules at densities corresponding to the saturated liquid densities found by simulations in a previous study.[56] These densities are shown in Table 1, below. The periodic simulation box comprised 1 unit cell of MOF-5, (cubic with a 25.832 Å side length).

All MD simulations were equilibrated for 5 ns, followed by a production period of at least 100 ns, which was found to be sufficiently long for the mean-squared

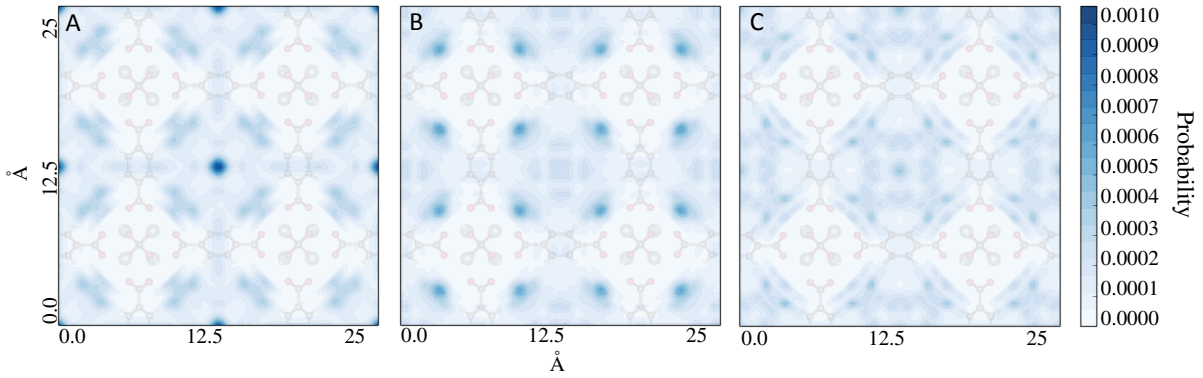

Figure 3: Results of the MD simulations at 280 K and loadings shown in Table 1 displaying the spatial probability distribution of liquid phase xylene molecules in the MOF-5 structure: (A) metaxylene, (B) orthoxylene, (C) paraxylene.

displacement (MSD) to become a linear function of time, as verified by measuring the slope of the MSD plot on a log-log scale. Self-diffusion coefficients were obtained by fitting the Einstein relation, $D_s = \frac{1}{6} \lim_{t\to\infty} \frac{d}{dt} \left\langle [r(t) - r(0)]^2 \right\rangle$, to the linear portion of the MSD versus time plot, using the order-n algorithm [68, 69] to collect MSD data.

Rotational Calculation of Spatial and Orientational Probability Distributions

Spatial density distributions of xylenes were generated from MD simulations (Fig. 3), where the center-of-mass of each xylene molecule was recorded every 5 fs and binned into a $100 \times 100 \times 100$ grid overlaid on the MOF-5 structure. As MOF-5 is cubic, the three-dimensional grid was reduced to a two-dimensional grid by averaging together all slices in one of the dimensions. In Fig. 3 these data are presented in the form of a probability maps. The angle between methyl groups on xylene molecules and the nearest neighboring carboxylate group was recorded every 0.5 ps. The methyl bond vector was defined as pointing from the aromatic carbon atom on the xylene to its bonded united atom methyl group. The carboxylate bond vector was defined as having either the carboxylate oxygen or carboxylate carbon as its vertex such that the vector always pointed in the positive x, y or z direction. These definitions yield symmetric distributions of the calculated angle. In Fig. 4, these data are presented in the form of probability density functions.

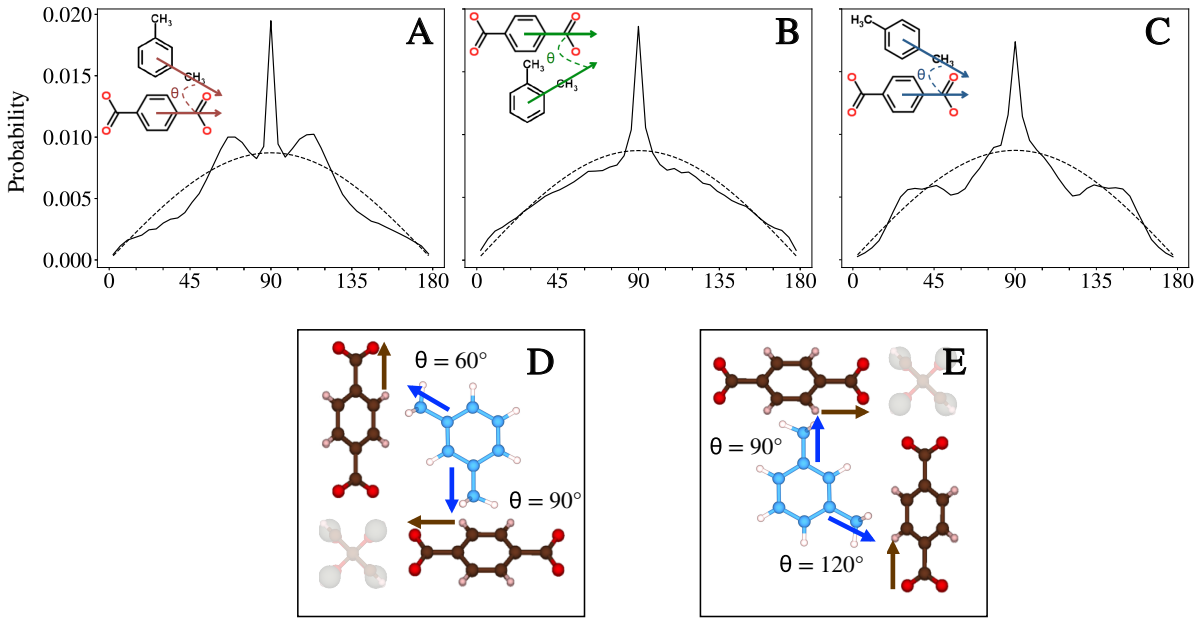

Figure 4: Probability density functions describing the likelihood of finding a methyl bond on a xylene molecule oriented at a range of angles relative to the nearest neighboring carboxylate group on a framework linker, demonstrated by (D) and (E), and the resulting distributions (A) metaxylene, (B) orthoxylene, (C) paraxylene. In (A), (B) and (C), the dashed black lines reflect a random distribution of methyl orientations. In (D) and (E), oxygen atoms are red, hydrogen atoms are light pink and carbon atoms on the xylene and linker are blue and brown, respectively.

Rotational Diffusion Coefficient Calculations

We define rotational displacement as $\hat{\psi}(t) = \int_0^t \Delta\hat{\psi}(t')dt'$ where both the magnitude and direction of vector $\Delta\hat{\psi}(t')$ are given by the normalized vector of interest $u(t)$ at times $t = t'$,$t' + dt'$. The magnitude of $\Delta\hat{\psi}(t')$ is given by $|\Delta\hat{\psi}(t')|= \cos^{-1}\left(u(t' + dt') \cdot u(t')\right)$ and direction is given by $u(t' + dt') \times u(t')$.[70] In this work, the vector of interest $u(t)$ is either the bond vector pointing from an aromatic xylene ring carbon to the its bonded methyl group (in-plane, $\|$) or the vector normal to the aromatic xylene ring (out-of-plane, $\perp$).

Analogously to translational motion, rotational self-diffusion coefficients were obtained by fitting the relation, $D_r = \frac{1}{4}\lim_{t\to\infty}\frac{d}{dt}\left\langle\left[\hat{\psi}(t) - \hat{\psi}(0)\right]^2\right\rangle$ to the linear portion

Table 2: Translational activation energy ($E_{a,\mathrm{trans}}$) calculated from an Arrhenius fit to the experimental data in Fig. 5. The actual $D_{0,\mathrm{trans}}$ were taken from the intercept of the linear fit with inverse temperature.

	p-xylene	m-xylene	o-xylene
$E_{a,trans}$ ($\mathrm{kJ\,mol^{-1}}$)	15.3	19.7	21.2
$D_{0,\mathrm{trans}}$ ($\mathrm{m^2\,s^{-1}}$)	1.8×10^{-7}	1.68×10^{-6}	2.45×10^{-6}
$E_{a,trans}$ ($\mathrm{kJ\,mol^{-1}}$)	15.3	16.1	10.3
$D_{0,\mathrm{trans}}$ ($\mathrm{m^2\,s^{-1}}$)	3.79×10^{-7}	3.93×10^{-8}	5.06×10^{-7}

of the rotational MSD versus time plot, defined as $\langle \psi^2(\Delta t) \rangle = \left\langle \left[\hat{\psi}(t + \Delta t) - \hat{\psi}(t) \right]^2 \right\rangle$.

2.4 Results and discussion

Translational Motion

The self-diffusion coefficients of (p,m,o)-xylene were measured as a function of diffusion time (τ_2) ranging from 10 ms to 100 ms, and temperatures ranging from 253 K to 293 K. These diffusion times were chosen to ensure that the xylene molecules would spend most of their time sampling the intracrystalline environment belonging to MOF-5 and very little time experiencing the inter-crystalline environment. The characteristic length (l_D) travelled by the adsorbed molecule was estimated using $l_D = \sqrt{D_{app}\tau_2}$; varying diffusion times from 10 ms to 100 ms yielded a range of characteristic lengths from 100 µm to 0.1 µm, much smaller than the MOF-5 crystal size. None of the self-diffusion coefficients of the xylene isomers demonstrated a strong dependence on the diffusion time, τ_2 (see Appendix A). All self-diffusion coefficients of the xylene isomers were dependent on the temperature and were analyzed with an Arrhenius fit of the self-diffusion coefficients at the shortest τ_2 value (10 ms). In this way the values of translational activation energy ($E_{a,\mathrm{trans}}$) and the entropic pre-exponential coefficient ($D_{0,\mathrm{trans}}$) of the xylene isomers were determined (Fig 5 and Table 2).

Paraxylene displays the fastest experimentally-determined self-diffusion coefficients at all temperatures (Fig. 5) and the lowest experimental calculated activation energy for translational motion (Table 2). Paraxylene translational motion in MOF–5 deviates from bulk isomer behavioral trends[71] by exhibiting the smallest pre-exponential factor; this is surprising because when measured in bulk it has the largest[72]. The simulated D_s are on the same order of magnitude as the experiment and display the same ordering between isomers. However, the temperature dependence of the

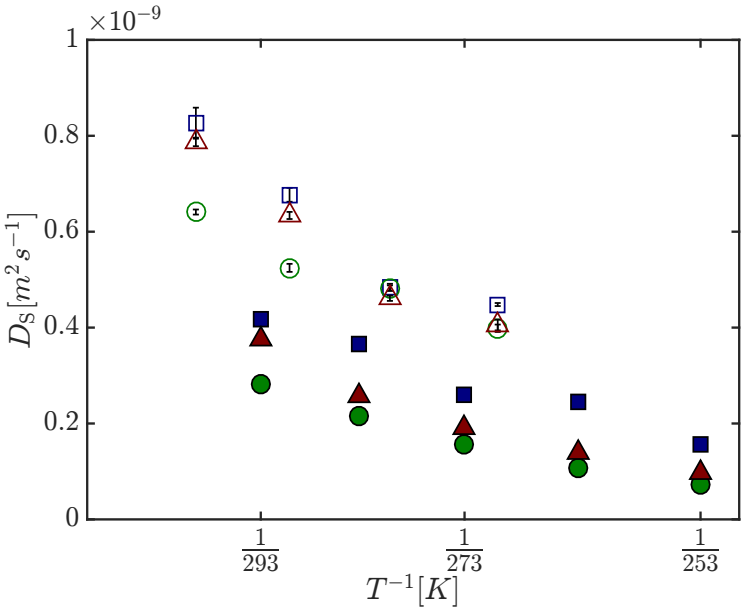

Figure 5: A plot of the experimental inverse temperature dependence of the self-diffusion coefficient for each xylene (para ■ , ortho ●, meta ▲) isomer at constant loading of 6 to 7 molecules/cage, and the simulated self-diffusion coefficients, (para □, ortho ◯, meta △).All error is calculated as the standard deviation of the measurement and is contained within the demarcation.

simulated D_s do not compare well with experiment, which is likely due to the D_s being very sensitive to adsorbate loadings, the temperature dependence of which could only be estimated based on past simulation work (Table 1).

We further explored the guest molecule configurations by considering the spatial probability distributions from the MD simulations (Fig. 3). These figures reveal the preferential adsorption sites of each xylene isomer. Metaxylene prefers to adsorb in the center of the pore, while orthoxylene prefers adsorption closer to those metal clusters that are located at the corners of the pore (Fig. 3 A and B, darker shaded areas). Paraxylene, by contrast, shows a more uniform distribution (Fig. 3 C). The presence of multiple and proximal preferential adsorption sites for orthoxylene and metaxylene suggests that their translational diffusion mechanism involves the hopping of molecules between these sites and that these adsorbates must overcome a larger free energy barrier to translate compared to paraxylene. These observations are consistent with the trend in the experimentally determined translational activation

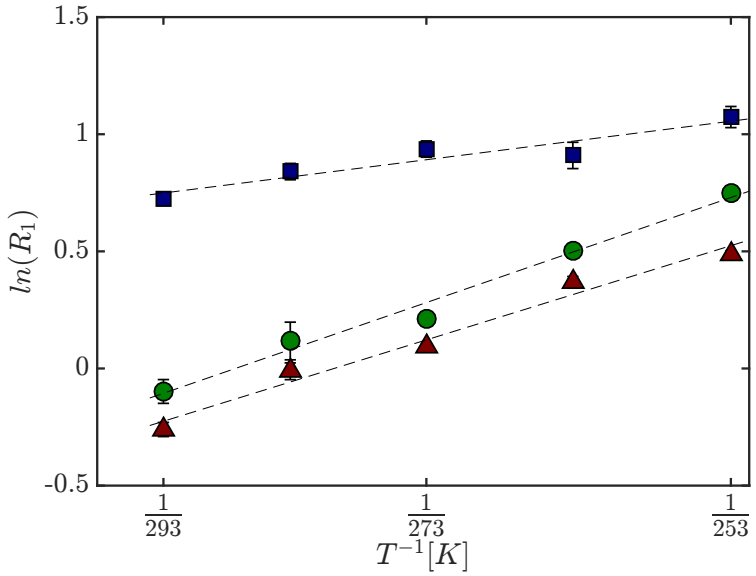

Figure 6: A plot of the experimental inverse temperature dependence of R_1 for each xylene (para ■ , ortho ●, meta ▲) isomer at constant loading of 6 to 7 molecules/cage.

energies.

Rotational Motion

The standard expression of the spin-lattice relaxation rate as a result of homonuclear dipolar coupling is $R_1 \propto J(\omega)+4J(2\omega)$ [73, 74], where R_1 is the inverse of T_1, J is the spectral density function, and ω is the Larmor frequency. We employ the simplified Lipari-Szabo model [75, 76] as the descriptor for the spectral density function to separate the contributions of molecular rotational motion and internal methyl motions to R_1. In this model-free formalism the spectral density is related to the correlation times by the expression, $J(\omega) = \frac{2}{5}\frac{\tau_m S^2}{1+\omega^2\tau_m^2} + \frac{(1-S^2)\tau}{1+[\tau^2\omega]^2}$, where τ_m is the isotropic rotational correlation time of the molecule, $\tau = \frac{\tau_m\tau_e}{\tau_m+\tau_e}$, and τ_e is an effective correlation time for internal motions (associated with methyl groups for xylene isomers); S^2 is a generalized order parameter ranging from 0 to 1 representing the degree of spatial restriction of the molecule in a medium[74].

Under the conditions in which the internal motion of methyl groups is extremely fast[77], $\tau_e \ll \tau_m$, and the order parameter is large, the truncated form of the Lipari-

Table 3: Experimental Rotational activation energy ($E_{a,\mathrm{rot}}$) of xylene molecules calculated from fitting the experimental longitudinal relaxation rate to an Arrhenius relation given in Fig. 6.

($\mathrm{kJ\,mol^{-1}}$)	p-xylene	m-xylene	o-xylene
$E_{a,rot}$	47.26	12.88	11.55

Table 4: The simulated in-plane and out-of-plane rotational activation energies and the pre-exponential factors fitted from an Arrhenius relation in Fig. 7.

	para	meta	ortho
$E_{a,rot,\parallel}$ ($\mathrm{kJ\,mol^{-1}}$)	17.03	11.37	6.0
$D_{0,\mathrm{rot},\parallel}$ ($\mathrm{rad^2\,ps^{-1}}$)	37.83	5.95	1.4
$E_{a,rot,\perp}$ ($\mathrm{kJ\,mol^{-1}}$)	10.84	10.06	9.05
$D_{0,\mathrm{rot},\perp}$ ($\mathrm{rad^2\,ps^{-1}}$)	10.43	4.2	2.44

Szabo spectral density function is suitable and internal motions (second additive terms) are neglected. The extreme motional narrowing regime applies, making it appropriate to associate $R_1 \propto S^2\tau_m$, assume the correlation time is exponential, then employ an Arrhenius analysis to determine the activation energies for restricted rotational motion of the xylenes adsorbed in MOF-5 (see Figure 6 and Table 3). Paraxylene is found to have almost four times the rotational activation energy of the other isomers and thus experiences some combination of increased spatial restriction (higher S^2 value) and/or a longer isotropic rotational correlation time. This is different from bulk behavior where the rotational activation energy ($E_{a,rot}$) were all on the same order of magnitude.[78]

MD simulations were performed at the aforementioned loadings and affirm the notion of paraxylene restricted rotational motion. For all three xylenes, two types of rotational motion were distinguished and tracked during the course of MD simulations. In-plane xylene rotation was tracked with the methyl bond vectors as a reference, and out-of-plane xylene rotation was tracked with the vector normal to the aromatic ring as a reference. Paraxylene displays a large difference between the in-plane and out-of-plane diffusion coefficients, with the out-of-plane coefficients being a factor of three larger (Fig. 7). The trend in the in-plane activation energies derived from these simulations show that paraxylene's activation energy is greater than that of both metaxylene and orthoxylene (Table 4).

To further explore the effect of confinement on the orientations sampled during rotational motion, the angle between the methyl bond and the bond connecting the nearest-neighbor carboxylate group to the aromatic part of organic linker was tracked.

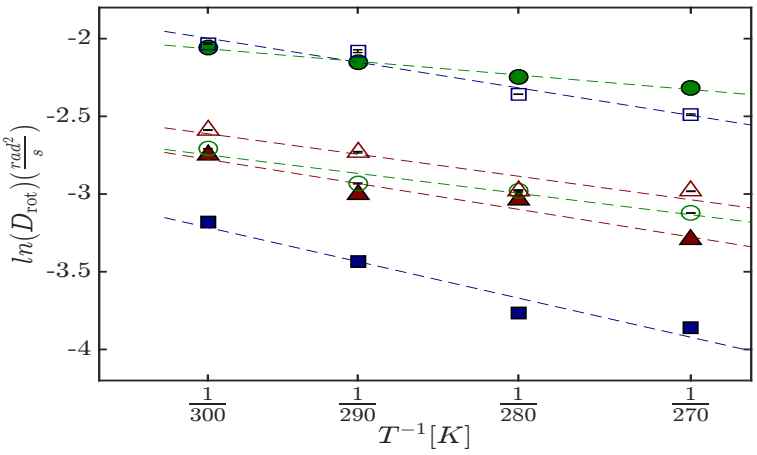

Figure 7: The inverse temperature dependence of the simulated rotational self diffusion coefficients for each xylene isomer at constant loading, where the filled symbols represent the in-plane rotation,(para ■ , ortho ●, meta ▲), results and the empty symbols represent the out-of-plane results, (para □, ortho ◯, meta △). The dashed lines represent the linear fit for an Arrhenius relationship.

The probability of finding a molecule oriented at a particular angle was then calculated for each xylene and the results are displayed in Fig. 4. The observed probability distributions shown in solid black lines can be compared to the dashed black lines, which shows a random distribution of methyl group orientations with the functional form $P(\theta) = \frac{1}{2}\sin(\theta)$. All xylenes display a dominating peak larger than that of the random distribution around 90°. This suggests the most favored orientation for a methyl group relative to the framework phenyl ring may be a t-configuration near π-pocket of the ligand. This is not the case for orthoxylene, as Fig. 3 shows that the molecular center-of-mass is predominantly found in the corners of the pore rather than the center.

Additional features in the metaxylene and paraxylene angle probability distributions can be intuited by considering the positions of the two methyl groups relative to each other. Fig 4 c and d demonstrate the proposed metaxylene configurations. The peaks at 60° and 120° in the metaxylene plot are observed because when one methyl group is in the favored orientation (perpendicular to one set of linkers) and the aromatic xylene ring is parallel to the other set of organic linkers, the second methyl group forms a 60° or 120° angle with the nearest neighboring carboxylate group. The paraxylene distribution is unique because when the aromatic xylene

ring is similarly-aligned parallel to one set of organic linkers, both methyl groups would be perpendicular to the other set, and there would be only a single peak at 90°. The additional features at 140° and 40° indicate that paraxylene cannot fit into configurations where it is oriented exactly parallel to a set of organic linkers and must be tilted with respect to the pore. Paraxylene therefore samples a more restrictive environment due to its rigid rod like shape.

2.5 Conclusion

MOF-5, synthesized as a large crystal, was imbibed with saturated-liquid loadings of metaxylene, orthoxylene, and paraxylene. The effects of subtle geometric differences between the isomers were manifest in the guest molecule translational and rotational motions, as observed using NMR techniques. The quantification of the self-diffusion coefficient and the longitudinal relaxation time as functions of temperature at constant loading allowed for the quantification of the translational and rotational activation energies for each species. Paraxylene was experimentally observed to have the fastest self-diffusion coefficient at all temperatures (p>m>o), the lowest activation energy for translational motion (p<m<o), and the highest activation energy for rotational motion (p>m>o). These results were compared with MD simulations and confirm the constriction of rotational freedom in an isotropically confined geometry and the faster translational motion of the most rod-like molecule, paraxylene. MD simulations indicate that neither metaxylene nor orthoxylene experienced comparable restrictions for in-plane rotations when adsorbed in MOF-5, supporting the experimental findings that paraxylene faces higher energy barriers for rotational motion.

References

(8) Li, J.-R.; Kuppler, R. J.; Zhou, H.-C. *Chem. Soc. Rev.* **2009**, *38*, 1477–1504.

(10) Kärger, J.; Caro, J.; Cool, P.; Coppens, M.-O.; Jones, D.; Kapteijn, F.; Rodríguez-Reinoso, F.; Stöcker, M.; Theodorou, D.; Vansant, E. F.; Weitkamp, J. *Chem. Eng. Technol.* **2009**, *32*, 1494–1511.

(16) Stallmach, F.; Gröger, S.; Künzel, V.; Kärger, J.; Yaghi, O. M.; Hesse, M.; Müller, U. *Angew. Chem. Int. Ed. Engl.* **2006**, *45*, 2123–6.

(28) Casanova, F.; Perlo, J., *Single-Sided NMR*; Casanova, F., Perlo, J., Blümich, B., Eds.; Springer Berlin Heidelberg: Berlin, Heidelberg, 2011.

(33) Rowsell, J. L.; Yaghi, O. M. Metal organic frameworks: a new class of porous materials., 2004.

(34) Li, H; Eddaoudi, M; O'Keeffe, M; Yaghi, O. *Nature* **1999**, *402*, 276–279.

(35) James, S. L. *Chem. Soc. Rev.* **2003**, *32*, 276.

(36) Furukawa, H.; Müller, U.; Yaghi, O. M. *Angew. Chem. Int. Ed. Engl.* **2015**, *54*, 3417–30.

(37) Li, J.-r.; Sculley, J.; Zhou, H.-c. *Chemical Reviews* **2012**, 869–932.

(38) Davis, M. E. *Nature* **2002**, *417*, 813–821.

(39) Kolokolov, D. I.; Diestel, L.; Caro, J.; Freude, D.; Stepanov, A. G. *The Journal of Physical Chemistry C* **2014**, *118*, 1287312879.

(40) Schlayer, S.; Pusch, A.-K.; Pielenz, F.; Beckert, S.; Peksa, M.; Horch, C.; Moschkowitz, L.; Einicke, W.-D.; Stallmach, F. *Materials (Basel).* **2012**, *5*, 617–633.

(41) Pusch, A.-K.; Splith, T.; Moschkowitz, L.; Karmakar, S.; Biniwale, R.; Sant, M.; Suffritti, G. B.; Demontis, P.; Cravillon, J.; Pantatosaki, E.; Stallmach, F. *Adsorption* **2012**, *18*, 359–366.

(42) Chmelik, C.; Freude, D.; Bux, H.; Haase, J. *Microporous Mesoporous Mater.* **2012**, *147*, 135–141.

(43) Sholl, D. S.; Lively, R. P. *Nature* **2016**, *532*, 435.

(44) Alaerts, L.; Maes, M.; Jacobs, P. A.; Denayer, F. M.; Vos, D. E. D. *Phys. Chem. Chem. Phys.* **2008**, *10*, 2979–2985.

(45) Rives, S; Jobic, H; Kolokolov, D. I.; Gabrienko, A. A.; Stepanov, A. G.; Ke, Y; Frick, B; Devic, T; Maurin, G *J. Phys. Chem.* **2013**, *47*, 6293–6302.

(46) Gabrienko, A.; Frick, B. *J. Phys. Chem. C* **2013**, *47*, 6293–6302.

(47) Moreira, M. A.; Santos, C.; Ferreira, A. F. P.; Loureiro, M. *Ind. Eng. Chem. Res.* **2011**, *50*, 7688–7695.

(48) Duan, L.; Dong, X.; Wu, Y.; Li, H; Wang, L; Song, L *J. Porous Mater.* **2013**, *53*, 431–440.

(49) Alaerts, L.; Kirschhock, C. E. a.; Maes, M.; van der Veen, M. a.; Finsy, V.; Depla, A.; Martens, J. a.; Baron, G. V.; Jacobs, P. a.; Denayer, J. F. M.; De Vos, D. E. *Angew. Chem. Int. Ed. Engl.* **2007**, *46*, 4293–7.

(50) Finsy, V.; Verelst, H.; Alaerts, L.; De Vos, D.; Jacobs, P. a.; Baron, G. V.; Denayer, J. F. M. *J. Am. Chem. Soc.* **2008**, *130*, 7110–8.

(51) Gu, Z.-y.; Jiang, D.-q.; Wang, H.-f.; Cui, X.-y.; Yan, X.-p. **2010**, 311–316.

(52) Gee, J. A.; Sholl, D. S. *J. Phys. Chem. C* **2016**, *120*, 370–376.

(53) Germanus, A.; Kärger, J.; Pfeifer, H.; Samulevič, N.; Zèanov, S. *Zeolites* **1985**, *5*, 91–95.

(54) Trens, P.; Belarbi, H.; Shepherd, C.; Gonzalez, P.; Ramsahye, N. A.; Lee, U. H.; Seo, Y. K.; Chang, J. S. *Microporous Mesoporous Mater.* **2014**, *183*, 17–22.

(55) Moreira, M. A.; Santos, C; Ferreira, A. F. P.; Loureiro, J. M.; Ragon, F.; Horcajada, P.; Shim, K.-e.; Hwang, Y.-k.; Lee, U; Chang, J.-s.; Serre, C.; Rodrigues, E *Langmuir* **2012**, *21*, 5715–5723.

(56) Braun, E.; Chen, J. J.; Schnell, S. K.; Lin, L.-C.; Reimer, J. a.; Smit, B. *Angew. Chem. Int. Ed. Engl.* **2015**, *54*, 14349–52.

(57) Chen, J. J.; Kong, X.; Sumida, K.; Manumpil, M. A.; Long, J. R.; Reimer, J. a. *Angew. Chemie Int. Ed.* **2013**, n/a–n/a.

(58) Carr, H.; Purcell, E. *Phys. Rev.* **1954**, *94*, 630–638.

(59) Galvosas, P.; Callaghan, P. T. *Comptes Rendus Phys.* **2010**, *11*, 172–180.

(60) Plimpton, S. *J. Comput. Phys.* **1995**, *117*, 1–42.

(61) Nosé, S. *Mol. Phys.* **1984**, *52*, 255–268.

(62) Hoover, W. G. *Phys. Rev. A* **1985**, *31*, 1695–1697.

(63) Kamberaj, H; Low, R. J.; Neal, M. P. *J. Chem. Phys.* **2005**, *122*, 224114.

(64) Dubbeldam, D; Walton, K. S.; Ellis, D. E.; Snurr, R. Q. *Angew. Chem. Int. Ed.* **2007**, *46*, 4496–4499.

(65) Wick, C. D.; Martin, M. G.; Siepmann, J. I. *J. Phys. Chem. B* **2000**, *104*, 8008–8016.

(66) Ford, D. C.; Dubbeldam, D.; Snurr, R. Q.; Snurr, R. Q. *Open-Access J. Basic Princ. Diffus. Theory, Exp. Appl.* **2009**, *11*, 1–8.

(67) Lemak, A. S.; Balabaev, N. K. *Mol. Simul.* **1994**, *13*, 177–187.

(68) Frenkel, D.; Smit, B., *Understanding Molecular Simulation: From Algorithms to Applications, Elzevier Science 2002*, 2002.

(69) Dubbeldam, D.; Ford, D.; Ellis, D.; Snurr, R.; Dubbeldam, D.; Ford, D.; Ellis, D.; Snurr, R.; Perspective, A. N. *Mol. Simul.* **2009**, *35*, 1084–1097.

(70) Mazza, M. G.; Giovambattista, N.; Stanley, H. E.; Starr, F. W. *Physical Review E* **2007**, *76*, 031203.

(71) Rousseau, B.; Petravic, J. *The Journal of Physical Chemistry B* **2002**, *106*, 13010–13017.

(72) Kitchlew, A.; Rao, B. D. N. *Mol. Phys.* **1971**, *21*, 1145–1147.

(73) L. Sudmeier, J.; E. Anderson, S.; S. Frye, J. *Concepts Magn. Reson.* **1990**, *2*, 197–212.

(74) Kowalewski, J.; Maler, L., *Nuclear Spin Relaxation in Liquids: Theory, Experiments, and Applications*, 2006.

(75) Szabo, A. *J. Am. Chem. Soc.* **1982**, *I04*, 4546–4559.

(76) Andrec, M.; Montelione, G. T.; Levy, R. M. *J. Biomol. NMR* **2000**, *18*, 83–100.

(77) Kimmich, R., *Strange kinetics, porous media, and NMR*; 1-2, 2002; Vol. 284, pp 253–285.

(78) Eades, R. G.; Jones, T.; Llewellyn, J. P. *J. Chem. Soc. Faraday Trans. 2 Mol. Chem. Pysics* **1972**, 1316–1322.

Chapter 3

Quantifying Internal Gradients in Metal Organic Frameworks

3.1 Motivation

Magnetic resonance techniques such as relaxometry and diffusometry have been widely employed for characterization of adsorbate-adsorbent dynamics and the structural configurations in porous materials.[79, 80] More recently, the community has sought to measure magnetic resonance time constants, longitudinal relaxation time (T_1), transverse relaxation time (T_2), and self-diffusion coefficient (D_s) of adsorbates adsorbed in metal-organic frameworks (MOFs) as a way to probe their inter- and intra-molecular dynamics.[15, 41, 81] Measurements of such time constants and diffusivities are grossly affected by the presence of any internal magnetic field gradient (g_{int}) that exists as a result of physical attributes of the media i.e. pore size, susceptibility, and chemical composition [82, 83]. Ignoring these contributions may lead to misinterpretation of experimental data [84]; either through incorrect implementation of basic magnetic resonance pulse sequences, or misattributing signal attenuation to the complex physical phenomenon.[85, 86]. Investigators have developed methods to compensate for measurements in the presence of g_{int}, yet have not been quantified or even qualitative assessed for many MOFs. As we seek to further employ magnetic resonance as a tool to characterize adsorbate dynamics in MOFs, correctly posed nuclear magnetic resonance (NMR) experiments and methodical analysis are crucial for our community to gain a better understanding of how inherent physical attributes of MOFs contribute to the presence of internal field gradients and thus observed relaxation time constants and self-diffusion coefficients. In this work we investigate and determine internal gradients present in the prototypical MOFs imbued with liquid adsorbates, pentane

and benzene, and correlate their contributions to the observed T_2 or $T_{2\text{eff}}$.

3.2 Introduction

NMR for investigation Internal Magnetic Field Gradients in Porous Media

Internal Magnetic Field Gradients (g_{int}) may be described as a distortion of the uniformity of a magnetic field (B_0). In porous materials imbibed with liquids, g_{int} are found to occur naturally due to magnetic susceptibility contrast $\Delta\chi$ associated with heterogeneous structures present in these nanoporous materials.[87] In fact, the porous media community has taken advantage of this correlation to calculate pore size distributions in rocks and cement[31]. These internal magnetic field gradients were later also observed to be dependent on pore geometry.[88] Liquid magnetic susceptibility contrasts with the susceptibility of the porous media and thus yields the g_{int} associted with porous media. These internal gradients contribute irreversibly to the de-coherence of the magnetization of nuclear spins associated with diffusing imbibed molecules, and many pulse sequences[85, 86, 89, 90]focus on minimizing this contribution to the NMR observables.

The magnitude of this additional decay due to the presence of internal gradient is moderated by the both the time spent and the speed at which the molecules move through the gradient field. The diffusive term contributing to transverse relaxation in the phenomenological Bloch Equations is, $D_0\nabla M$, where D_0 is the self-diffusivity and ∇M is any applied or constant magnetic field gradient. The characteristic length needed to be traveled during the course of an NMR experiments for the internal gradients to contribute to additional decoherence of transverse magnetization is

$$l_g = \frac{D_0}{\gamma g_{\text{int}}} \tag{3.1}$$

where γ is the gyromagnetic ratio of the diffusing nuclei, and D_0 is the apparent diffusion coefficient of the liquid. Typically, the relaxation of the transverse magnetization can be measured utilizing a Carr-Purcell-Meiboom-Gill (CPMG) train (Fig 1A) [20]. Although the contribution of g_{int} is minimized due to rapid refocusing pulses, the diffusive attenuation not associated with g_{int} occurs during the sequence and its characteristic length is described as:

$$l_E = (D_0\tau_{\text{Echo}})^{\frac{1}{2}}. \tag{3.2}$$

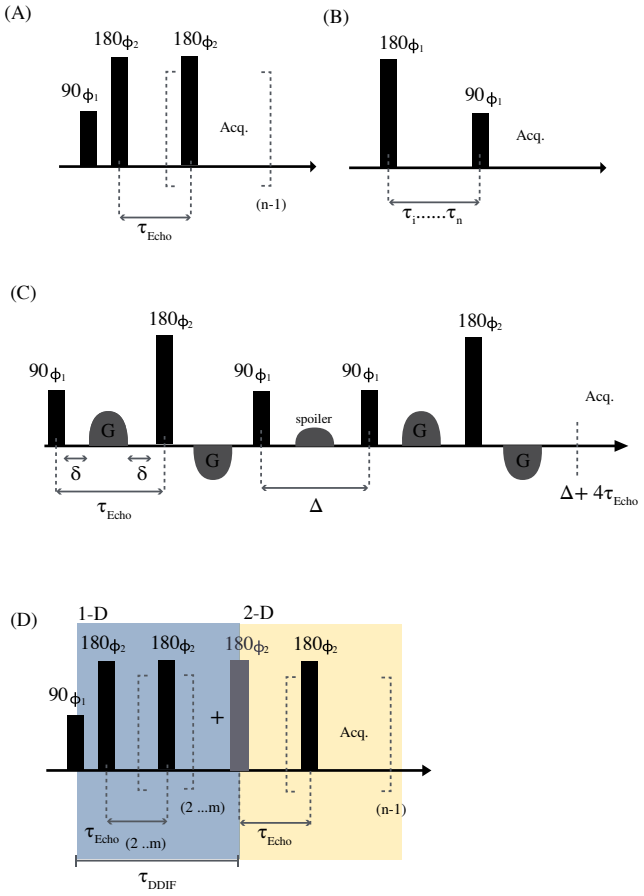

Figure 1: Schematic depictions of (A) the Carr-Purcell-Meiboom-Gill (CPMG) sequence, where τ_{Echo} is the echo time or spacing between echo and the signal is acquired in between π pulses; (B) the Inversion Recovery Sequence, where τ_i is the the variable time delay;(C) 13 Interval Bi-Polar Pulse Field Gradient Stimulated Echo (13 Interval BP-PFGSTE), where δ is the time between the RF pulses and the gradient pulse G, τ_{Echo} is the echo time associated with this pulse sequence, Δ is the diffusion time while magnetization is stored the z-direction; and (D) the two-dimensional DDIF (Diffusion Decay in Internal Field Gradients)-CPMG or the modified CPMG sequence where $\tau Echo_{2..m}$ is a variable echo time with the corresponding number of echos (m) to keep τ_{DDIF} constant.

Under the condition that $l_E \ll l_g$ the correlation between the diffusive decay due to internal field gradients and the observed or effective transverse relaxation time (T_{2eff}) can be quantified. Therefore two pulse sequences are employed and combined, which are a modified CPMG (Fig 1 (D)) [90] to quantify the decay in internal gradients and the 13 Interval Bi-Polar Pulse Field Gradient Stimulated Echo[27] sequence (Fig 1 (C)) to measure D_s. The attenuation in each sequence is dependent on different parameters, which can be found in Table 1. The 13 Interval BP-PFGSTE sequence allows for isolation of D_s which is used in the analysis of the 2D DDIF-CPMG sequence enabling the correlation of g_{int} and T_{2eff} [90] through a 2D Inverse Laplace Transformation of the data.

Information about T_{2eff} is obtained by a CPMG Acquisition in the 1st dimension, while the 2nd dimension encodes information about the diffusive decay by the constant time DDIF sequence. All of the experiments were carried out on an Avance Bruker 300 MHz NMR spectrometer using a Diff30 gradient system at 25 °C. The duration of the 90° pulse was 1.8 µs and the diffusion times, Δ and τ_{DDIF} ranged from 3 ms to 5 ms while variable echo times ranged from 20 µs to 2500 µs where the shortest echo time was used for the CPMG acquisition. In the 13 Interval BP-PFGSTE sequence the maximum applied gradient strengths ranged from 1.8 T m^{-1} to 4 T m^{-1}.

Table 1: The attenuation of the pulse sequences, , and DDIF-CPMG, based on the experimental parameters introduce in the used to characterize the

Sequence	Signal Attenuation
CPMG	$M = M_0 \exp(\frac{\tau}{T_{2\text{eff}}})$
Inversion Recovery	$M = M_0(1 - 2\exp(\frac{\tau}{T_1}))$
13	$M = M_0 \exp\,(\,-(\gamma g_{\text{app}} 2\delta)^2 D_{\text{s}} \tau_{\text{DDIF}}$
DDIF-CPMG	1D $M = M_0 \exp(\frac{\tau}{T_{2\text{eff}}})$ 2D $M = M_0 \exp((g_{\text{int}} m_{\text{i}} \tau_{\text{Echo}})^2 D_{\text{s}} \tau_{\text{DDIF}})$

Prototypical Metal-Organic Frameworks

In this section we introduce as set of prototypical metal-organic frameworks investigated for separation and storage purposes [37]. These MOFs were chosen to represent some of the most common classes of topologies and pore chemistries. The open metal site, isotropic, *cage and window* type MOF $Cu_2(BTC)_3$ (btc = 1,3,5

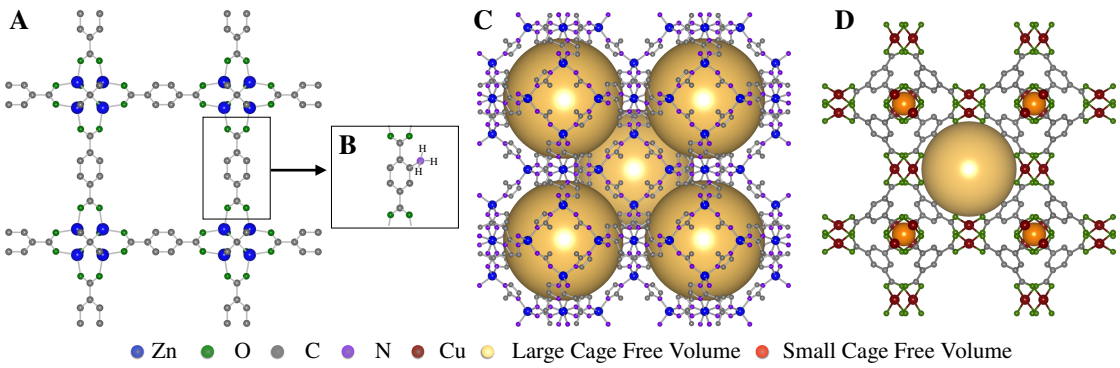

Figure 2: Schematic of the structure of the prototypical MOF (A) IRMOF-1 , (B) IRMOF-3, (C) ZIF-8, and (D) $Cu_2(BTC)_3$.

benzene tricarboxylate a.k.a. HKUST-1) was first synthesized in 1999. $Cu_2(BTC)_3$ has three pore sizes or domains where the largest pore (9 Å) is surrounded by the middle pore (5 Å) and a small triangular pore (3 Å) serving as the connecting window between the middle and large pore (Fig. 2 (D)). Since its introduction as one of the first open-metal site MOFs, with under coordinated Cu^{2+}located in the large pores (Figure 2, yellow balls), investigators have explored its use and the affinity of the under coordinated Cu sites for storage of small molecules and catalysis.

Zeolitic imidazolate frameworks (ZIFs) are a series of MOFs that actualize topologies similar to known zeolites due to the bridging angle inherent to the imidazole organic linker. Zinc 2-methyl-imidazolate ($Zn(MeIM)_2$) framework or ZIF-8 has the sodalite zeolite structure with 11.6 Å sized large pores and 3.6 Å sized pores as the small windows. ZIF-8 has large cages connected by small windows in cubic SOD-like topology (Fig. 2 (C)). ZIF-8 is was initially well known for its thermal and chemical stability motivating investigators to explore the use of ZIF-8 in both post-combustion carbon capture and more recently natural gas enrichment[91, 92].

Isoreticular metal-organic framework (IRMOF)-1, better known as MOF-5 (Figure 2 (A)) was initially investigated for hydrogen adsorption technologies [34]. This type of IRMOF has many analogues of varying pore size and chemistry retaining its basic crystal structure [93]. IRMOF-1 is composed of tetrahedral metal oxide clusters and rod-like organic ligands, bdc (1,4-benzenedicarboxylic acid) linker. The IRMOF-3 MOF, shown in the inset (Fig 2 (B)), is of the same topology as IRMOF-1 with amine functionalization of the linker, NH_2-bdc (2-amino-1,4-benzenedicarbocylic acid). IRMOF-3 is investigated to probe the effect of changing the pore chemistry through linker functionalixzation on the observed g_{int}-T_{2eff} correlation. Table 2 shows the optimized synthesis conditions used to produce large crystals for this investigation.

3.3 Methods

Synthesis of Metal Organic Frameworks

IRMOF-1 Synthesis

IRMOF-1 was synthesized by preparing a 3:1 mixture of zinc nitrate hexahydrate and 1,4-benzenedicarboxylic acid (Sigma Aldrich chemicals, 99.95 % purity) in 100 mL of diethylformamide (DEF) and heating for 72 hours at 90 °C, resulting in a typical crystal size of 425 µm. Solvent exchanges from DEF to dry dimethylformamide (DMF) were followed by solvent exchanges from DMF to dry dichloromethane (DCM) in preparation for activation. After solvent exchange, powder x-ray diffraction spectra were measured at room temperature using a D8 Discover GADDS Powder XRD (see Supporting Information) and nitrogen (Praxair, 99.999 %) adsorption isotherms were collected using a Micromeritics TriStar 3000 BET instrument, which determined the BET surface area of the crystals to be 3565 $m^2\,g^{-1}$.

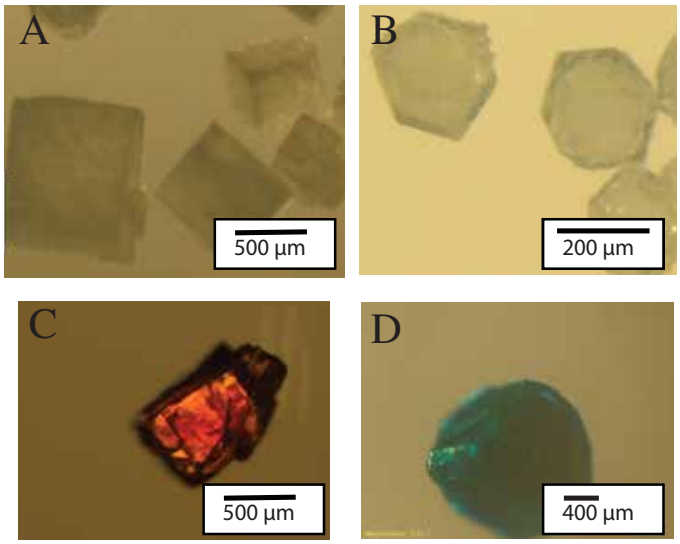

Figure 3: Showing the magnified images of the large crystals used in this investigation. (A) IRMOF-1, (B) ZIF-8, (C) IRMOF-3, (D) $Cu_2(btc)_3$ = 1,3,5 benzene tricarboxylate ($Cu_2(BTC)_3$)

IRMOF-3 Synthesis

IRMOF-3 was synthesized by preparing a 3:1 mixture of zinc nitrate hexahydrate and 1,4-(2-amino)benzenedicarboxylic acid (Sigma Aldrich chemicals, 99.95 % purity) in 100 mL of DEF and heating for 72 hours at 90 °C, resulting in an typical crystal size of 425 µm. Solvent exchanges from DEF to dry DMF were followed by solvent exchanges from DMF to dry DCM in preparation for activation. After solvent exchange, powder x-ray diffraction (PXRD) spectra were measured (see Supporting Information) and nitrogen adsorption isotherms determined the BET surface area of the crystals to be $3147\,m^2\,g^{-1}$.

Table 2: Showing the final synthesis conditions and the starting materials of the prototypical MOF crystals during solvothermal synthesis optimized for larger crystals.

MOF	Metal Salt	Organic Linker	Solvent	Temperature	Duration	Crystal Size
ZIF-8	$Zn(NO_3)$	2-methyl-imidazolate	Methanol	110 °C	72 hours	>350 µm
IRMOF-1	$Zn(NO_3)$	1,4-benzenedicarboxylic acid	DEF	90 °C	72 hours	>425 µm
IRMOF-3	$Zn(NO_3)$	1,4-(2-amino)benzenedicarboxylic acid	DEF	90 °C	72 hours	425 µm
$Cu_2(BTC)_3$	$Cu(NO_3)$	1,3,5 benzene tricarboxy-late	DMF	85 °C	1 week	650 µm

ZIF-8 Synthesis

A 1:1 mixture of Zinc nitrate tetrahydrate and 2-methylimidazole from SigmaAldrich dissolved in 120 120 mL of DMF and heated for 72 hours 120 °C resulting in a typical crystal size of 350 µm for ZIF-8. Solvent exchanges from DMF to chloroform $CHCl_3$ to methanol were made in preparation for activation. After solvent exchange, powder x-ray diffraction spectra were measured at room temperature (PXRD) (see Supporting Information) and nitrogen adsorption isotherms were determined the BET surface area of the crystals to be $1794\,m^2\,g^{-1}$.

$Cu_2(BTC)_3$ Synthesis

A solvothermal method was used to synthesize large $Cu_2(BTC)_3$ single crystals, which consisted of the dissolution of copper nitrate trihydrate ($Cu(NO_3)_2 \cdot 3H_2O$) with benzene-1,3,5-tricarboxylic acid (H_3BTC) into DMF and sub-sequentially the addition of 12 12 mL of glacial acetic acid. The solution was refrigerated overnight and then place in a oven at 90 °C for 1 week. Solvent exchanges from DMF to dry DCM were in preparation for activation. After solvent exchange, powder x-ray diffraction (PXRD) spectra were measured at room temperature and nitrogen adsorption isotherms were collected to determined the BET surface area of the crystals to be 1986 $m^2\,g^{-1}$.

NMR Sample Preparation

All samples were activated under flow of argon gas at a temperature of 150 °C to degas the samples overnight. Afterwards a 425 µm sieve separated approximately 250 mg of the larger crystals, which were re-activated overnight at 150 °C and 0.01 mbar of vacuum. Then they were sealed in a flame-dried 5 mm glass NMR tube. Magnified images were obtained of each crystal batch to confirm the typical crystal size. A small sample of crystals were separated for powder x-ray diffraction (PXRD). The crystals were loaded with the respective solvent according to literature isotherms when available [94–97].

3.4 Results and Discussion

Self Diffusivity of Saturated MOFs

The D_s of each solvent adsorbed in these MOFs are shown in Table 3. All measurements were conducted near or at saturation loadings[94, 96–99]. In general benzene molecules diffuse slower than pentane molecules in the IRMOF frameworks. Benzene has a kinetic diameter of 2 Å and pentane has a kinetic diameter of 3 Å, and both interact differently with the frameworks. Benzene is suspected of having weak $\pi - \pi$ interactions with the phenyl rings on framework organic ligands [98, 100–102] and pentane is suggested to have weak Van-der-Wall interactions with the pores in the IRMOF series[37], and thus diffuse faster. However in the cage and window MOFs $Cu_2(BTC)_3$ and ZIF-8, pentane diffuses slower because it has a higher probability of be found in the small windows or cages.

Table 3: The D_s or pentane and benzene at or near saturation loadings in IRMOF-1, IRMOF-3, ZIF-8, and $Cu_2(BTC)_3$ at room temperature

Solvent	MOF	Loading	D_s m^2/sec
Benzene	IRMOF-1	7-8 molecules per cage	$1.778 \pm 0.18 \times 10^{-13}$
	IRMOF-3	6-7 molecules per cage	$1.136 \pm 0.004 \times 10^{-11}$
	ZIF-8	2-3 molecules per cage	$5.367 \pm 0.419 \times 10^{-10}$
	$Cu_2(BTC)_3$	14-15 molecules per large cage	$2.312 \pm 0.4389 \times 10^{-10}$
Pentane	IRMOF-1	3-5 molecules per cage	$2.443 \pm 0.03 \times 10^{-9}$
	IRMOF-3	3-4 molecules per cage	$1.385 \pm 0.167 \times 10^{-8}$
	ZIF-8	2-3 molecule per cage	$9.2485 \pm 0.2 \times 10^{-11}$
	$Cu_2(BTC)_3$	13-14 molecules per large cage	$6.332 \pm .329 \times 10^{-11}$

Internal Gradients in Prototypical MOFs

The reported magnetic susceptibility of benzene (68.80×10^{-8})[103] is less than that of pentane (79.23×10^{-8}) [103]. The correlation maps correlated the the value of the T_{2eff} with the value of the internal gradient, The graphs along the right and top side of the correlation maps are the distrubutions of either the T2eff or the g_{int} wieghted by the population as indicated by the correlation maps; they are not the resultin 1-D Inverse Lapalace transformations.

Internal Gradients in the IRMOF-1 and IRMOF-3

Comparing the g_{int}-T_2 correlation maps of Benzene (Figure 4, Figure 6) to those of pentane (Figure 5, Figure 7) shows that greater magnitudes of g_{int} exist for benzene imbibed in the IRMOF series. Earlier NMR investigations of benzene in IRMOF-1 suggested that benzene experiences broad distribution of effective T_2 due to the coexistence of both the vapor and liquid phases at all loading below the critical point[56], It is possible that the broad distribution of g_{int}-T_{2eff} correlation maps in Fig 4 and Fig 6 may be attributed to this phenomenon. Pentane sample both a narrower distribution of and smaller magnitudes of g_{int}.

Internal Gradients in the Window and Cage MOFs

The observed g_{int}-T_{2eff} correlation maps for ZIF-8 showed that benzene (Fig 8) has a lower average value of g_{int} than pentane (Fig 9). In ZIF-8 there are no phenyl-benzene, or $\pi - \pi$ stacking interactions due to the imadzolate linker, thus interactions with the framework are weaker than with IRMOFs. Molecular dynamics

adsorption studies of adsorbate motion in the ZIF framework indicate that although pentane-framework interactions are weak, diffusivity between the cages is limited by small connecting windows[104]. Pentane, the more linear molecule is able to diffuse more freely through the windows where it may experience higher magnitudes of g_{int}. The same investigation indicated the similar trends in the influence of pore accessibility for $Cu_2(BTC)_3$. In $Cu_2(BTC)_3$ system pentane sampled slightly higher magnitudes of g_{int} than benzene. Both pentane and benzene demonstrate a very broad range of g_{int} which we attribute to the presence of paramagnetic Cu at the open metal sites.

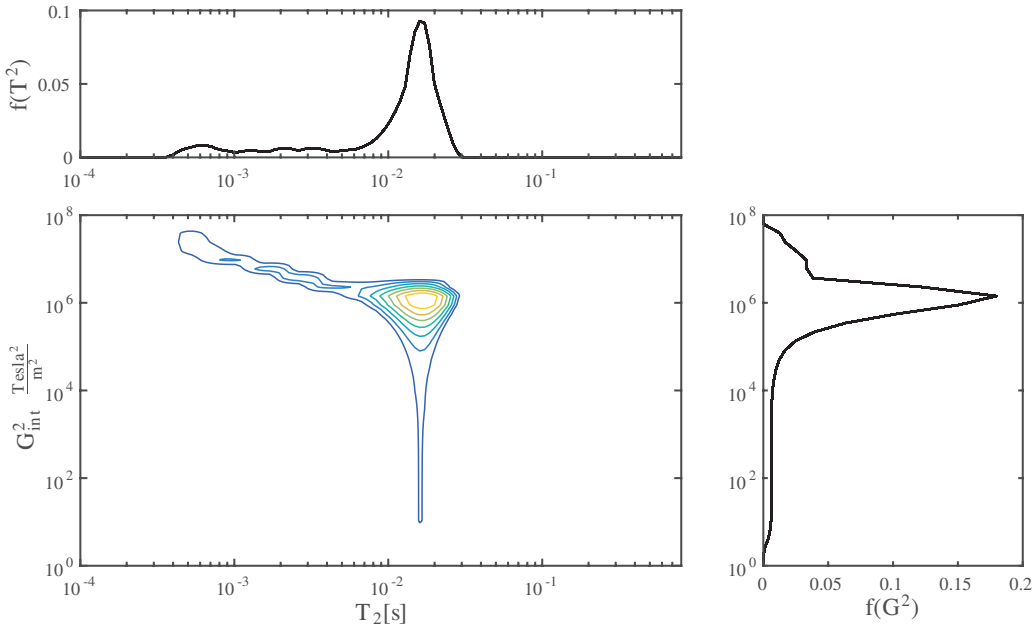

Figure 4: 2-D ILT resulting ${g_{\text{int}}}^2 - T_{2\text{eff}}$ Correlation Map (left bottom) of benzene in IRMOF-1 with corresponding 1-D Projections for $T_{2\text{eff}}$ (top) and ${g_{\text{int}}}^2$ (right)

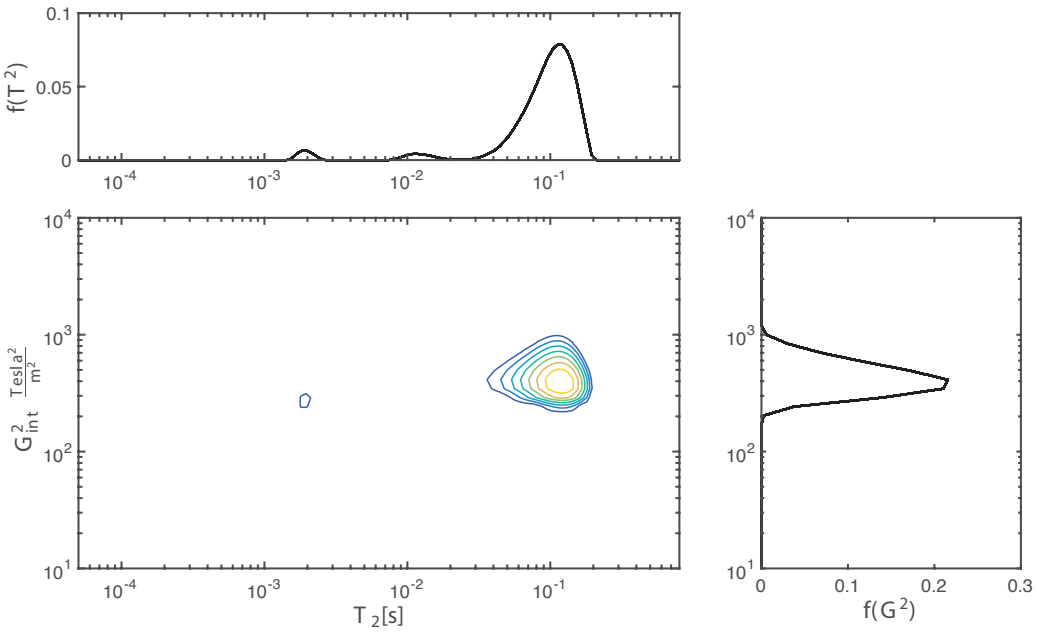

Figure 5: 2-D ILT resulting ${g_{\text{int}}}^2 - T_{2\text{eff}}$ Correlation Map (left bottom) of pentane in IRMOF-1 with corresponding 1-D Projections for $T_{2\text{eff}}$ (top) and ${g_{\text{int}}}^2$ (right)

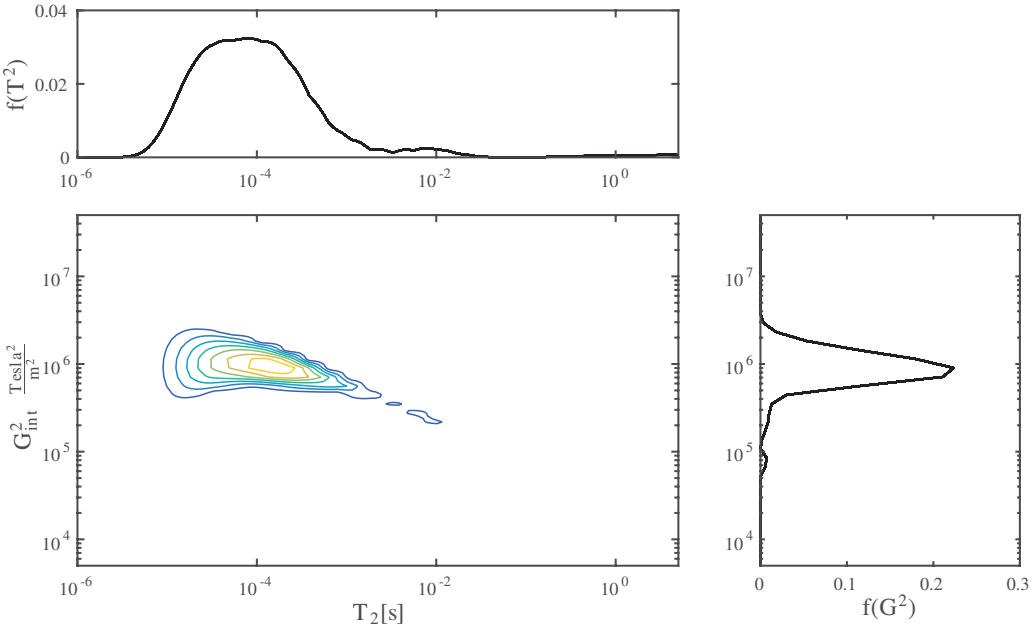

Figure 6: 2-D ILT resulting ${g_{\text{int}}}^2 - T_{2\text{eff}}$ Correlation Map (left bottom) of benzene in IRMOF-3 with corresponding 1-D Projections for $T_{2\text{eff}}$ (top) and ${g_{\text{int}}}^2$ (right)

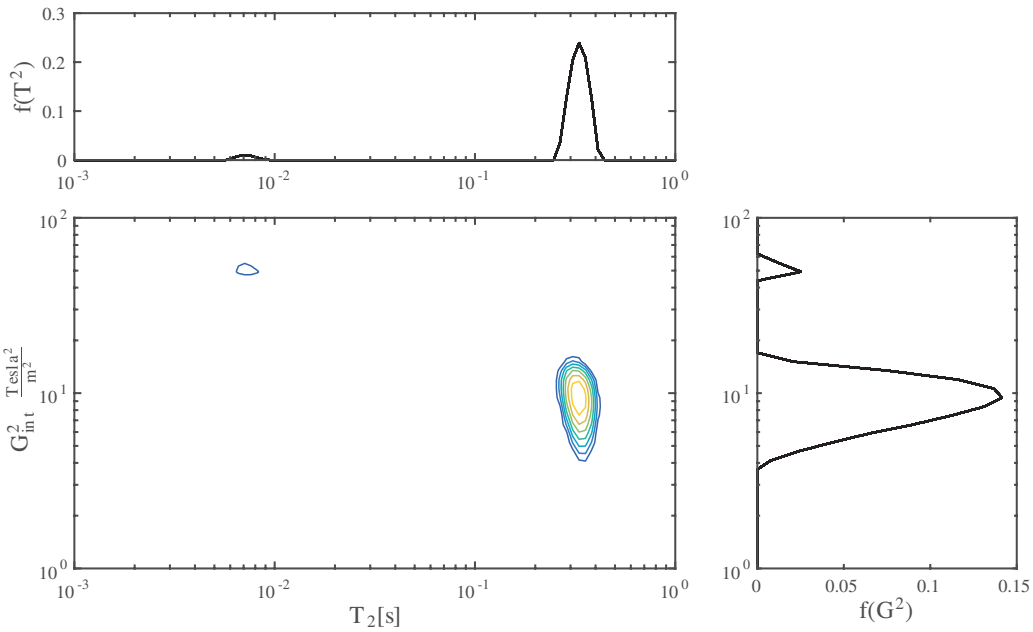

Figure 7: 2-D ILT resulting ${g_{\text{int}}}^2 - T_{2\text{eff}}$ Correlation Map (left bottom) of pentane in IRMOF-3 with corresponding 1-D Projections for $T_{2\text{eff}}$ (top) and ${g_{\text{int}}}^2$ (right)

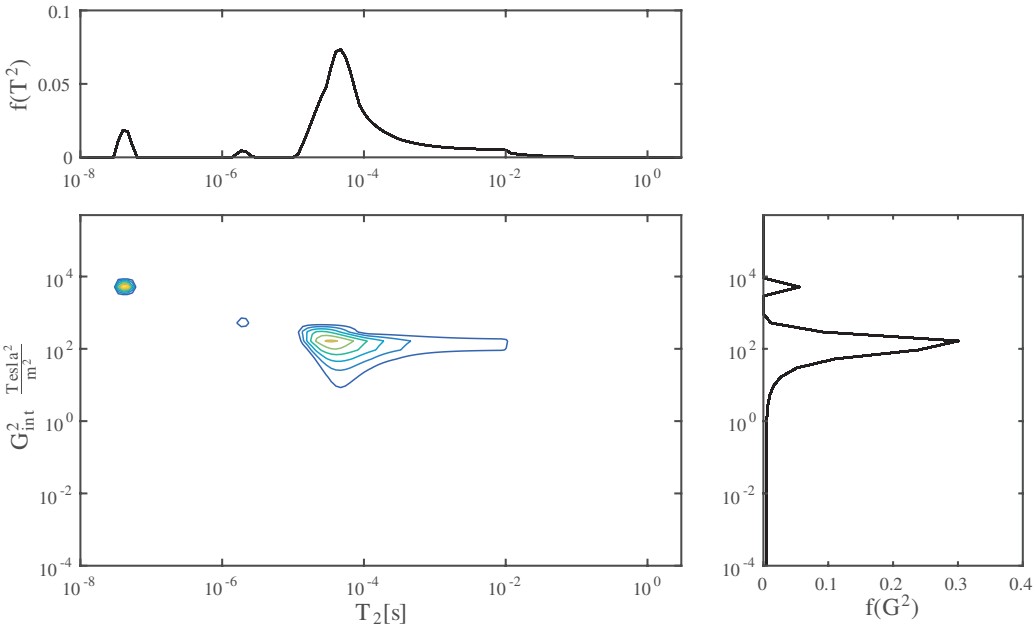

Figure 8: 2-D ILT resulting ${g_{\text{int}}}^2 - T_{2\text{eff}}$ Correlation Map (left bottom) of benzene in ZIF-8 with corresponding 1-D Projections for $T_{2\text{eff}}$ (top) and ${g_{\text{int}}}^2$ (right)

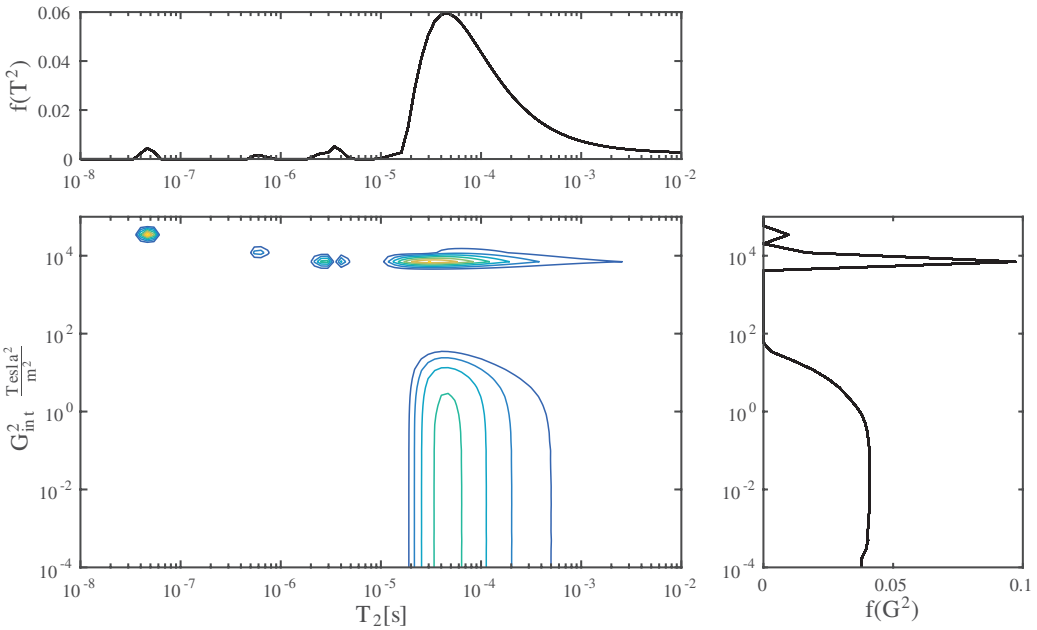

Figure 9: 2-D ILT resulting ${g_{\text{int}}}^2 - T_{2\text{eff}}$ Correlation Map (left bottom) of pentane in ZIF-8 with corresponding 1-D Projections for $T_{2\text{eff}}$ (top) and ${g_{\text{int}}}^2$ (right)

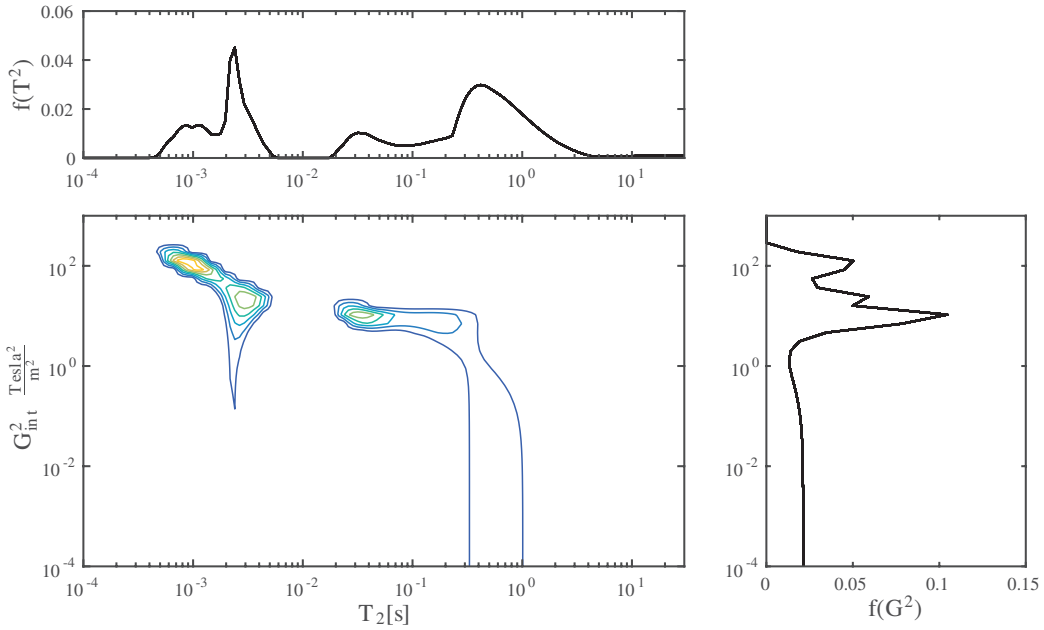

Figure 10: 2-D ILT resulting ${g_{\text{int}}}^2 - T_{2\text{eff}}$ Correlation Map (left bottom) of benzene in $Cu_2(BTC)_3$ with corresponding 1-D Projections for $T_{2\text{eff}}$ (top) and ${g_{\text{int}}}^2$ (right)

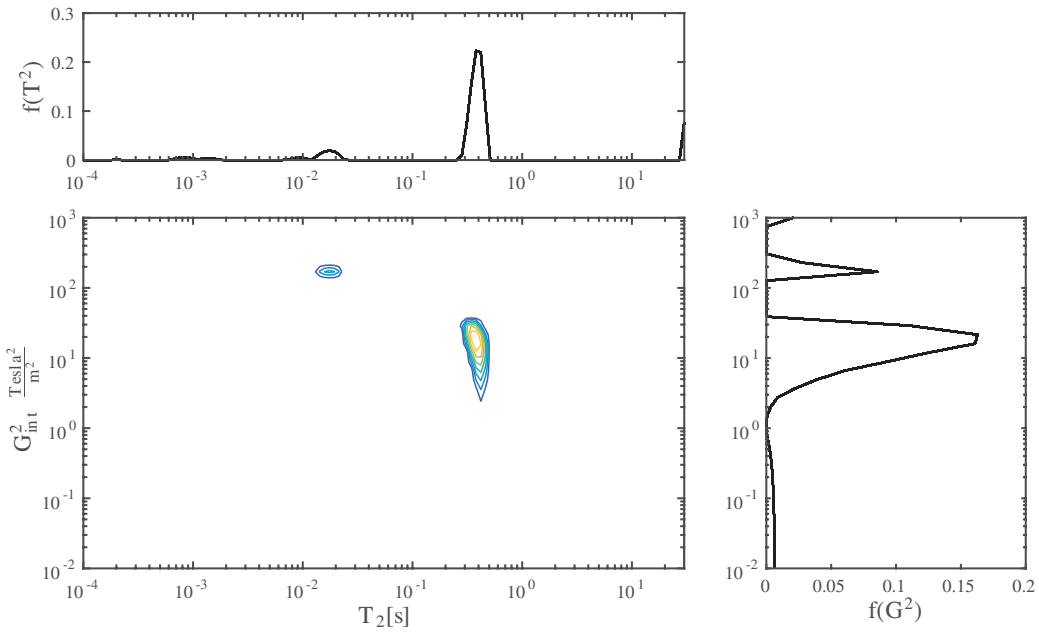

Figure 11: 2-D ILT resulting ${g_{\text{int}}}^2 - T_{2\text{eff}}$ Correlation Map (left bottom) of pentane in $Cu_2(BTC)_3$ with corresponding 1-D Projections for $T_{2\text{eff}}$ (top) and ${g_{\text{int}}}^2$ (right)

3.5 Conclusion

$G^2 - T_2$ 2D correlation maps were acquired of prototypical MOFs embibed with pentane and benzene. We demonstrated that g_{int} in these systems are not negligible and must be considered when interpreting complex trends in relaxation times. Due to the lower susceptibility difference, we suspect them to become less significant at lower fields. In general, for both benzene and pentane, larger pore MOFs induces smaller g_{int} on the solvents than MOFs with smaller pores or windows. For both pentane and benzene, the stronger interactions between the framework and the adsorbate lead to a sampling of g_{int} of greater magnitude. There is not a strong correlation between the number of pore size present in MOFs with the observed distributions of g_{int}. The effect of the open metal site on the sampled g_{int} for MOFs does not appear significant for these adsorbate-MOF systems except that it is dominated by the presence of a paramagnetic ion.

References

(15) Barrie, P. J. *Annu. reports NMR Spectrosc.* **2000**, *41*, 265–316.

(20) Bloembergen, N.; Purcell, E. M. E.; Pound, R. R. V. *Phys. Rev.* **1948**, *73*, 679–712.

(27) Cotts, R. M.; Hoch, M. J. R.; Sun, T; Markert, J. T. I. *J. Magn. Reson.* **1989**, *266*, 252–266.

(31) Song, Y.-Q. Q. *Concepts Magn. Reson.* **2003**, *18A*, 97–110.

(34) Li, H; Eddaoudi, M; O'Keeffe, M; Yaghi, O. *Nature* **1999**, *402*, 276–279.

(37) Li, J.-r.; Sculley, J.; Zhou, H.-c. *Chemical Reviews* **2012**, 869–932.

(41) Pusch, A.-K.; Splith, T.; Moschkowitz, L.; Karmakar, S.; Biniwale, R.; Sant, M.; Suffritti, G. B.; Demontis, P.; Cravillon, J.; Pantatosaki, E.; Stallmach, F. *Adsorption* **2012**, *18*, 359–366.

(56) Braun, E.; Chen, J. J.; Schnell, S. K.; Lin, L.-C.; Reimer, J. a.; Smit, B. *Angew. Chem. Int. Ed. Engl.* **2015**, *54*, 14349–52.

(79) Song, Y. Q.; Cho, H; Hopper, T; Pomerantz, A. E.; Sun, P. Z. *J Chem Phys* **2008**, *128*, 52212.

(80) D'Agostino, C.; Mitchell, J.; Mantle, M. D.; Gladden, L. F. *Chem. - A Eur. J.* **2014**, *20*, 1–8.

(81) Horch, C.; Schlayer, S.; Stallmach, F. *J. Magn. Reson.* **2014**, *240*, 24–33.

(82) Mitchell, J; Chandrasekera, T. C.; Gladden, L. F. *Prog. Nucl. Magn. Reson. Spectrosc.* **2012**, *62*, 34–50.

(83) Washburn, K. E. *Concepts Magn. Reson. Part A* **2014**, *43A*, 57–78.

(84) Sorland, G. H. *J. Magn. Reson.* **1997**, 146–148.

(85) Mitchell, J; Griffith, J. D.; Collins, J. H. P.; Sederman, a. J.; Gladden, L. F.; Johns, M. L. *J. Chem. Phys.* **2007**, *127*, 234701.

(86) Grunewald, E.; Knight, R. *Near Surf. Geophys.* **2011**, *9*, 1–10.

(87) Hürlimann, M. *J. Magn. Reson.* **1998**, *131*, 232–40.

(88) Cho, H. J.; Sigmund, E. E.; Song, Y. *Materials (Basel).* **2012**, *5*, 590–616.

(89) Sørland, G. H.; Aksnes, D.; Gjerdåker, L. *J. Magn. Reson.* **1999**, *137*, 397–401.

(90) Sun, B.; Dunn, K.-J. *Phys. Rev. E* **2002**, *65*, 51309.

(91) Stallmach, F.; Pusch, A.-K. K.; Splith, T.; Horch, C.; Merker, S. *Microporous Mesoporous Mater.* **2015**, *205*, 36–39.

(92) Chmelik, C.; Freude, D.; Bux, H.; Haase, J. *Microporous Mesoporous Mater.* **2012**, *147*, 135–141.

(93) Deng, H.; Grunder, S.; Cordova, K. E.; Valente, C.; Furukawa, H.; Hmadeh, M.; Gándara, F.; Whalley, A. C.; Liu, Z.; Asahina, S.; Kazumori, H.; O'Keeffe, M.; Terasaki, O.; Stoddart, J. F.; Yaghi, O. M. *Science* **2012**, *336*, 1018–23.

(94) Zhang, L.; Qian, G.; Liu, Z.; Cui, Q.; Wang, H.; Yao, H. *Sep. Purif. Technol.* **2015**, *156*, 472–479.

(95) Sarkisov, L.; Düren, T.; Snurr, R. Q. *Mol. Phys.* **2003**, *-1*, 1–1.

(96) Zhang, K.; Lively, R. P.; Zhang, C.; Chance, R. R.; Koros, W. J.; Sholl, D. S.; Nair, S. *J. Phys. Chem. Lett.* **2013**, *4*, 3618–3622.

(97) Zukal, A.; Opanasenko, M.; Rubeš, M.; Nachtigall, P.; Jagiello, J. *Catal. Today* **2015**, *243*, 69–75.

(98) Sun, X; Li, H; Li, Y; Xu, F; Xiao, J; Xia, Q; Li, Y; Li, Z *Chem. Commun.* **2015**, *51*, 10835–10838.

(99) Zhao, Z.; Wang, S.; Yang, Y.; Li, X.; Li, J.; Li, Z. *Chem. Eng. J.* **2015**, *259*, 79–89.

(100) Amirjalayer, S.; Tafipolsky, M.; Schmid, R. *Angew. Chemie - Int. Ed.* **2007**, *46*, 463–466.

(101) Amirjalayer, S.; Schmid, R. *Microporous Mesoporous Mater.* **2009**, *125*, 90–96.

(102) Ueda, T.; Kurokawa, K. *J. ...* **2011**, 1012–1019.

(103) Broersma, S. *J. Chem. Phys.* **1949**, *17*, 873–882.

(104) Krishna, R.; van Baten, J. M. *Phys. Chem. Chem. Phys.* **2013**, *15*, 7994–8016.

Chapter 4

Influence of the Open Metal site on CH4 Rotational and Translation Motion in MgMOF74

4.1 Abstract

Metal-organic frameworks (MOFs) are a novel class of porous materials with potential for applications as solid adsorbents in gas separation and storage processes. It is important to probe the translational motion of gases confined within MOFs in order to better understand interactions between hosts and adsorbates, thereby contributing basic knowledge to improve the functionality and design of MOFs for a targeted application. Investigations of MOFs probed experimentally by nuclear magnetic resonance (NMR)[41] and computationally by molecular dynamics (MD)[105] have improved understanding of the translation dynamics taking place. However, paired studies (experimental and simulated) with systematic variations of pore attributes are rare.[106] We investigate the loading dependence of methane (CH_4) adsorbed in three metal analogues of the M_2(dobdc) series (M = Mg, Ni, Zn) to understand the influence of the open-metal site (OPM) on adsorbate motion. The complementary investigations of motion via NMR and MD simulations suggest that the intracrystalline self-diffusivity is dominated by the adsorption strength of the CH_4 to the OPM at low loadings. CH_4-CH_4 interactions become more significant at higher loadings resulting in larger self-diffusion coefficients (D_s) and longer rotational correlation times.

4.2 Introduction

MOFs are novel materials that consist of metal-oxide clusters coordinately bound together by organic linkers that serve as bridges and pillars to create porous framework structures. These materials are easily modified via organic linker functionalization, transition metal exchange, and post-synthetic modification, often resulting in unprecedented degrees of separations selectivity for targeted small molecules [107]. Isoreticular MOFs, are a subclass of MOFs that retain a single topology while synthetic variations allows for systematic changes of influential pore attributes. M = (Ni,Zn,Mg); $dobdc^4$-=2,5-dioxodo1-4-bezenediacarboxylate a.k.a. M-MOF-74 (M_2(dobdc)) is part of the isoreticular subclass and has shown great potential for applications in gas storage and separation technologies, show in Fig. 1. [108] Improvements of these materials for selective interactions with CH_4 is important for chemical processes such as natural gas enrichment and the separation of CH_4 and CO_2.[109] Investigators have systematically evaluated the potential of MOFs for natural gas storage, showing that the choice of transition metal in the M_2(dobdc) could increase or decrease the MOF's adsorptive capacity.[110] Fig. 2 shows the experimental isotherms data taken at low pressure for the Ni, Zn, and Mg analogues of M_2(dobdc).

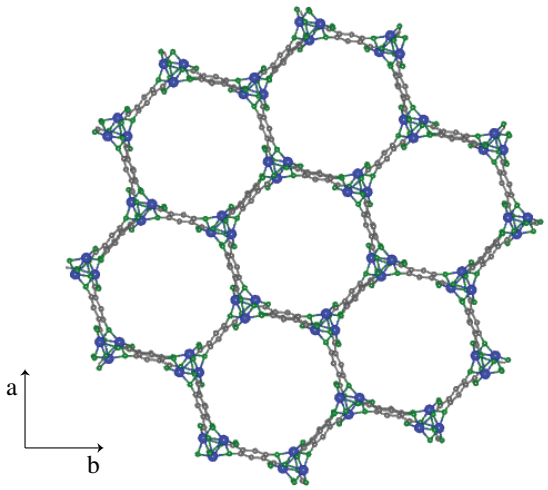

Figure 1: Schematic of M_2(dobdc) where green is O, blue is the metal (M=Zn, Mg, or Ni), and gray is C. H are ommited for clarity.

Neutron sacttering characterization of CH_4 in the (dhtp)=2,5-dihydroxyterephtalate linker analogue of M_2(dobdc) found that primary adsoprtion sites were located directly above the OPM and that secondary adsoprtion sites were either coordinated

to the first adsorbed CH_4 or in the center of the pore. [111] In both studies the nickel analogue of M_2(dobdc) was shown to have the one highest volumetric uptakes, 230 $cm^3\,g^{-1}$ while the other analogues were significantly lower: Mg (200 $cm^3\,g^{-1}$) and Zn (188 $cm^3\,g^{-1}$).[110] It was suggested that difference between the analogues were due to the binding energies associated with the adsorption of CH_4 to the OPMs. The experimentally reported low pressure uptake isotherms are shown in Fig. 2[110, 112] demonstrating difference at low pressures. Later a computational investigation[112] ranked the relative binding energies of CH_4 adsorbed in M_2(dobdc) from highest to lowest (Ni >Mg>Zn). This studies also showed that higher binding energies were associated with the primary adsorption sites while the secondary adsorption sites has slightly lower binding energies.[112] Analysis of the spatially probability distribution produced through the MD calculations investigators showed that for the strongly interacting metal ions, the location of the adsorption sites for gases were more evenly spread along the channels of the pores.

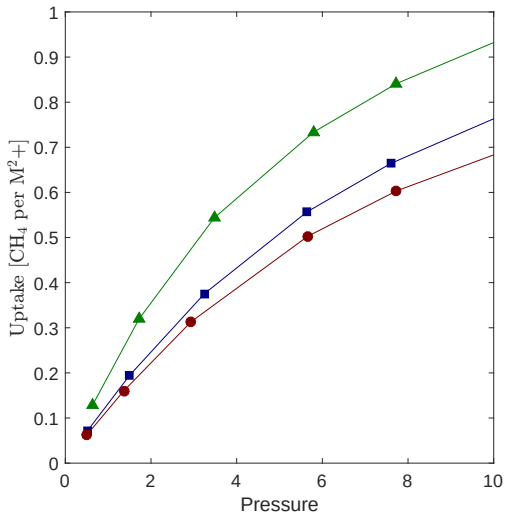

Figure 2: Low pressure experimental uptake CH_4 isotherms with the pressure in bar on the x axis and the uptake in molecules per metal site on the y axis. Experimental data taken from [112]

We have chosen to investigate the influence of the OPM ion on the translational and rotational motion of CH_4 because the performance of adsorption-based applications depends both on energectics of the systems as well as mass transfer. The transport phenomenon of CH_4 in M_2(dobdc) was previously investigated via permeation experiments for pack-bed applications. The investigators found these

macroscopic methods yielded averaged mass transfer coefficients with contributions from both the intercrystalline and intracrystalline regimes [113]. Understanding the transport phenomenon of small molecules in MOFs has proven challenging as only a few available experimental techniques may assess mass-transfer coefficients associated with the intracrystalline regime [114] where systematic variation of pore attributes are most influential. NMR is a robust and proven method that has been implemented to understand the motion of adsorbed gases via observation of their self-diffusion coefficients and relaxation rate constants as a function of thermodynamic states [16, 115][21]. MD simulations performed as a function of loading of other MOFs indicate that the observed intracrystalline D_s is a strong function of the interaction strength of the adsorbate the framework [104].

4.3 Methods

Nuclear Magnetic Resonance

Ex-Situ Sample Preparation

MOFs were evacuated and placed under argon in a glove box for transfer to a valved NMR glass tube. The sample was reactivated for 12 hours at 180 °C and 0.01 mbar. Samples were then cooled to 40 °C and held at the desired equilibrium pressure for 1 hour before closing the valve on the NMR tube. The sample was allowed to cool to room temperature and transferred to the probe where it was re-heated to 40 °C for 1 hr before experiments were performed.

Measurement

The 13 Interval Bi-Polar Pulse Field Gradient Stimulated Echo (13 Interval BP-PFGSTE) with z-spoiler[27] was implemented by a Bruker Avance III 700 MHz spectrometer and the Diff30 insert in the Mic5 Bruker imaging probe. Diffusion times ranged from 1 ms to 2.5 ms while gradient strength range from 0 $\mathrm{T\,m^{-1}}$ to 5.58 $\mathrm{T\,m^{-1}}$ with 48 steps. The observed attenuation was processed using bi-exponential fit o the attenuating signal. The reported values are the mean of 3-5 measurements at each loading. The longitudinal relaxation time (T_1) was characterized by the Inversion Recovery Pulse Sequence (180-90-Acquire) and transverse relaxation time (T_2) was measure by implementation of the Carr-Purcell-Meiboom-Gill (CPMG) pulse sequence. For all sample loadings $T_1 > T_2$ and the stimulated echo diffusion time was much less than T_1 or T_2.

Molecular Dynamics

The self-diffusion coefficients were computed for CH_4 in M_2(dobdc) (M = Mg, Ni, and Zn) using MD simulations performed in LAMMPS.[60] The systems were simulated in the canonical ensemble at loadings corresponding to the equilibrium uptakes from grand canonical monte carlo (GCMC) simulations at 313 K between 0.1 bar and 10 bar. After equilibration, each system was simulated for a total of either 100 ns (0.1 bar $\leq P \geq$ 10 bar) or 10 ns ($P >$ 10 bar) with a timestep of one femtosecond using a Nosé-Hoover thermostat, and a unit cell consisting of 6 channels (1x1x4 supercell).

Self diffuscion coefficients of adsorbed CH_4 were calculated by dividing by 6 the slopes of linear fits to the mean-squared displacements (MSDs) of methane in each framework between 2 and 1000 ps, where the adsorbed gas is in the diffusive regime under all considered conditions with enough statistics for the MSDs to be meaningful. For framework-methane interactions, DFT-derived force field of [112] was used, with methane-methane interactions taken from TraPPE [116] and select framework-methane interactions taken from UFF[65].

Probability densities of adsorbed CH_4 in all three M_2(dobdc) frameworks were computed by binning the positions of CH_4 from the first 10 ns of each MD simulation on a 0.1 Å x 0.1 Å x 0.1 Å grid and plotted using VisIt[117].

Structural details: Simulations for all three frameworks were done in 1x1x4 supercells built from orthogonal unit cells with the following lattice parameters (all numbers in $\mathring{A}$) – Mg: a = 26.114, b = 45.230, c = 6.917; Ni: a = 26.017, b = 45.063, c = 6.829; Zn: a = 52.191, b = 45.198, c = 6.882. The simulation structures have the following densities – Mg: 0.887 996 g cm^{-3}; Ni: 1.162 86 g cm^{-3}; Zn: 1.196 34 g cm^{-3}. Both the Mg_2(dobdc) and Ni_2(dobdc) structures contain 36 OPMs per unit cell (144 per supercell), whereas the Zn_2(dobdc) structure contains 72 OPMs per unit cell (288 per supercell).

4.4 Results and Discussion

It was previously observed that for gaseous species the observed spin-lattice relaxation times decreased with increasing density in what was considered a low density regime.[118] Earlier investigators understood that in the low density regime the magnitude of the contributions of the spin-rotation mechanism is dominated by the number of binary collisons or the density of the gas. The spin-lattice relaxation times exhibited a minimum, which defined the transition to the intermediate to high density regimes (reciprocal regime of T_1 and density). In the high density regime T_1 for gases behave similar to liquids.

To further understand these phenomena, one must posit the underlying mechanisms for the spin-lattice relaxation.

$$\frac{1}{T_{1\,obs}} = \frac{1}{T_{1\,intra}} + \frac{1}{T_{1\,inter}} + \frac{1}{T_{1\,CSA}} + \frac{1}{T_{1\,SR}} \tag{4.1}$$

$$\tag{4.2}$$

The first contribution is from intra-molecular interactions, which in the case of CH_4 are predominately dipole-dipole interactions from ^{1}H-^{1}H and ^{1}H-^{13}C on a single molecule. These may be neglected for most gases near or above room temperature because the spectral density funtion $J(\omega)$ is flat in respect to the larmor frequency. [119] Contributions from chemical shift anisotropy (CSA) are important for the observation of nuclei with large chemical shift ranges. This does not apply to CH_4 because protons have a very narrow chemical shift span. Other types of contributions are classified as inter-molecular interactions. These may be represented by ^{1}H-^{1}H,^{1}H-Metal, and ^{1}H-^{13}C between different CH_4 molecules or CH_4 near the framework nuclei. The last contribution, often considered the dominant one for gaseous species, is the spin-rotation relaxation, stemming from the coupling beween molecular rotational angular momentum and spin of each nucleus.[120].

Thus, as a function of gas density at very low densities, T_1 is large. The T_1 will reach a minimum when the collision frequency is very low; this corresponds to the spin-precession frequency and the collision frequency being equal to each other. Then T_1 enters the reciprocal regime where it increases linearly with gas density.[119]. Stallmach et al.[115] observed this expected behavior for intermediate to high densities of CH_4 gas adsorbed in zeolitic MOFs. They proposed that in addition to the traditional density dependent contributions from inter- and intra-molecular dipole-dipole interactions, the spin rotation mechanism is influenced by interactions with the framework scaled by amount contact with the surface of the pore. A surface relaxivity term, ρ_S, was used to describe the slope of the observed spin-lattice relaxation times with increasing density. The authors compared the fitted ρ_S to quantify the strength of interaction between the frameworks and the gases.

However, the observed T_1 of CH_4 gas in M_2(dobdc) initially decreases with increasing density because the collison frequency is low. For most pure gases in the low density regimes, the spin-lattice relaxation is dominated by the frequency of binary collisions. This may be attributed to the presence of the primary adsorption site, which was found to be located adjacent to the OPMs, [111] and as shown by the MD simulations at low loadings. With increasing loading, as long as the metal sites are remain significantly undersaturated, the rate of CH_4 binary collisons is controlled by the CH_4 hopping frequency between OPMs, or the free energy barrier for translational

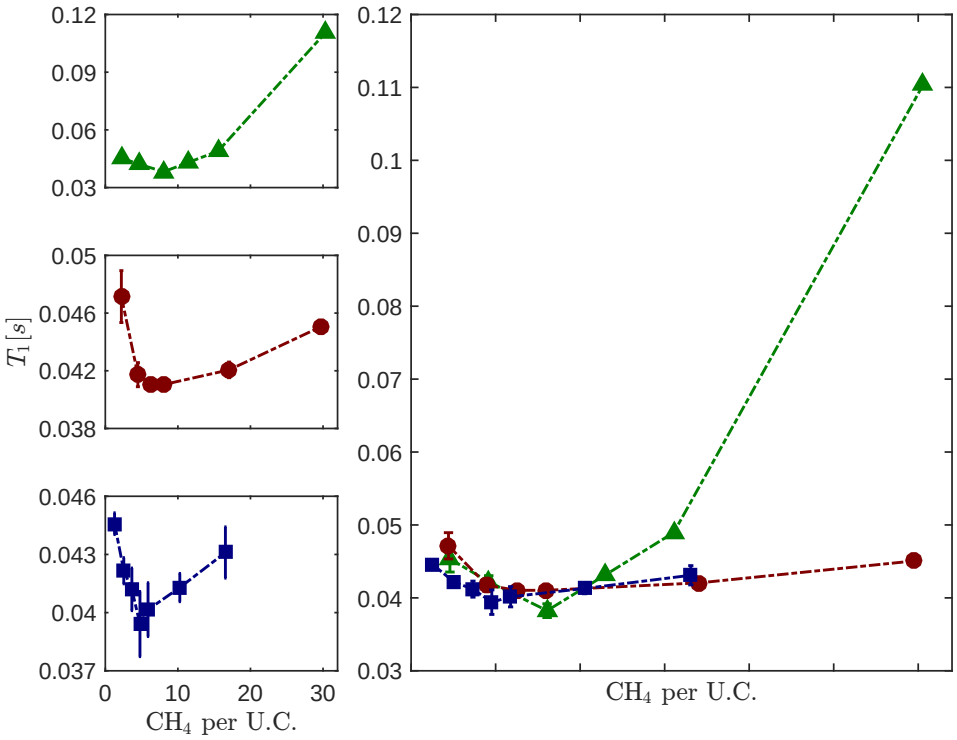

Figure 3: The T_1 of CH_4 adsorbed in the Zn, Mg, and Ni analogues of M_2(dobdc) as a function of adsorbed number of molecules. Interpolated lines are shown as guides.

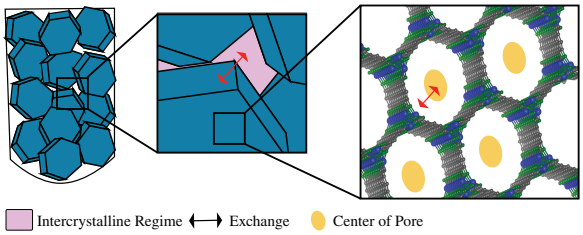

Figure 4: Schematic representing the population where the NMR observable are average within these environments due to fast exchange

motion. In this regime it is supsected that the contributions from intermolecular interactions are more significant due to the increased likelyhood of proximity to the OPM and pore surface. As the metal sites become occupied, more methane

molecules are left in the weakly adsorbed locations of the pore. Exchange between primary and secondary adsorption sites, as well as exchange with free methane, consequentially decreases the spin-rotational correlation time as the probability of collsion and methane-methane interactions increases. This is the behavior normally expected for methane gas [118] The trends for each analogue passes through a minimum corresponding to the frequency of collision for that adsorbed gas. The collison frequencies corresponding to the minimum values, 26.1445 Hz,25.3743 Hz,and 24.3665 Hz for Ni,Mg, and Zn respectively, are slightly different due to varying frame pore chemistry. The CH_4 adsorbed in both the Zn and Mg analogues reach their minimum at under 5 molecules per u.c. while Ni reaches its minimum close to 10 molecule per u.c. 3, suggesting that metal-CH_4interactions in these analogues allow for more CH_4-CH_4methane collisions or interactions.. In the reciprocal regime it is possible to correlate the observed slope with the surface relaxivity but there is not enough data to confirm the transition from this regime close to the minimum.

The analysis of the diffusive signal attenuation led to the presence of two D_s. On set on the order of of $1 \times 10^{-7}\,\mathrm{m\,s^{-2}}$, and a smaller D_s was much slower with values on the order order of $1 \times 10^{-9}\,\mathrm{m\,s^{-2}}$. We expect that the faster population is attributed to rapid exchange between the free gass in the inter-crystalline space and adsorbed gas in the MOF, whilst the slower population is describes the of the intercrystalline CH_4. All analogues of M_2(dobdc) posses small crystal sizes, 10 µm to 30 µm, for the as synthesize powders meaning the diffusive path of the molecule in a 2 ms diffusive time still travels hundreds of microns. The trend in the magnitude of the D_s of each analogue from largest to smallest is Zn >Mg >Ni. This suggest that the weakest interacting analogue allows for faster translation motion while the strong interaction in Ni hinder this motion.

MD simulations containing more CH_4 molecules per unit cell than OPMs were carried out so as to see if the D_s increased after all OPMs were occupied, as the methane spends the majority of the time during simulation above these sites. The idea is that once all the strong binding sites are filled, additional methane molecules can diffuse much more quickly through the center of the pores, where the binding energy is weaker. However, this was not observed. Instead, it is observed is that the D_s increases slightly with the pressure going from 0.1 bar to 1 bar, and then remains at about $1 \times 10^{-7}\,\mathrm{m\,s^{-2}}$ for all higher pressures considered, as shown in Fig. 6 Interestingly, the D_s is inversely correlated with the binding energy at the OPMs (Ni >Mg >Zn), such that it is fastest in Zn_2(dobdc) (Zn_2(dobdc)) and slowest Ni_2(dobdc) (Ni_2(dobdc)). The magnitudes of the intra-crystalline D_s measured by NMR and the D_s calculated by MD differed by 1 order of magnitude but displayed similar increasing trends. This faster NMR D_s may be attributed to the fast exchange between adsorbed CH_4 the inter-crystalline CH_4.

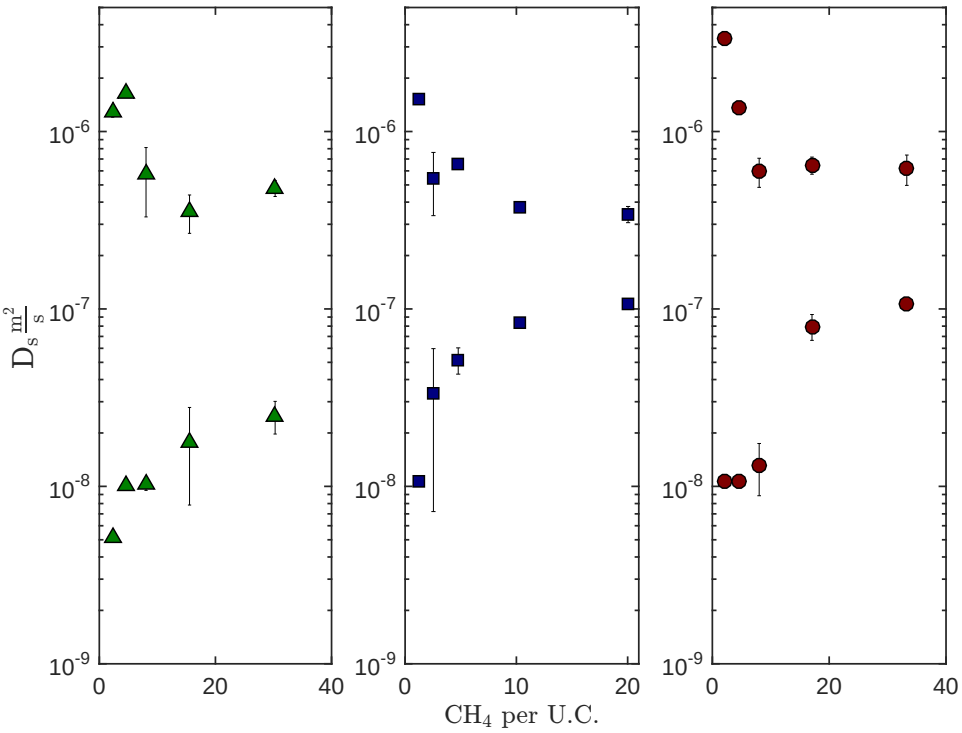

Figure 5: The D_s of CH_4 in Ni, Mg, and Zn analogues of M_2(dobdc) measure by NMR for 2 ms of diffusion time.

4.5 Conclusion

The Ni analogue of M_2(dobdc) had the strongest influence on the observed T_1 times of CH_4 in M_2(dobdc) possibly attributed to increased rotational correlation times . Two experimental D_s were observed for all loading, whilst MD calculations in a defect-free (and perfectly periodic) system yielded only one observed D_s. The magnitude of the intracrystalline CH_4 D_s from smallest to largest was Ni <Mg <Zn demonstrating that CH_4 interacted the most strongly with the Ni analogue. The MD simulations demonstrated that with increasing loading the self diffusion coefficient approached a single value for all analogues

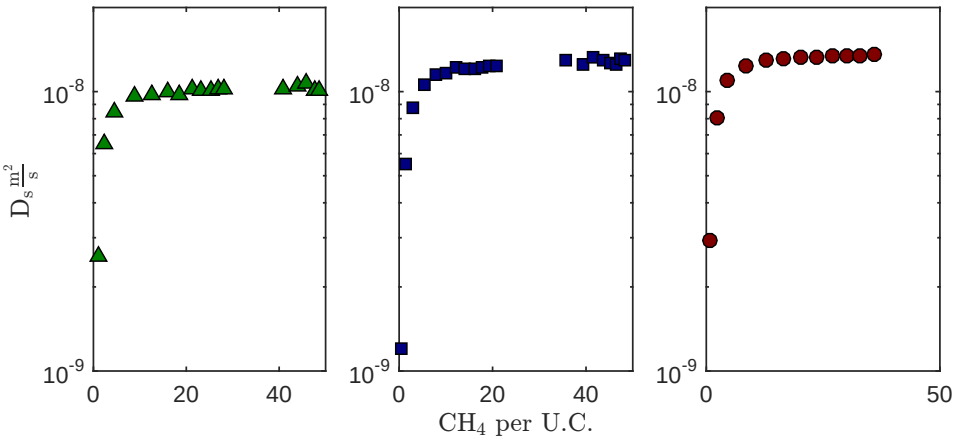

Figure 6: The D_s of CH_4 in Ni, Mg, and Zn analogues of M_2(dobdc) calculated by MD.

References

(16) Stallmach, F.; Gröger, S.; Künzel, V.; Kärger, J.; Yaghi, O. M.; Hesse, M.; Müller, U. *Angew. Chem. Int. Ed. Engl.* **2006**, *45*, 2123–6.

(21) Kong, X.; Scott, E.; Ding, W.; Mason, J. a.; Long, J. R.; Reimer, J. a. *J. Am. Chem. Soc.* **2012**, *134*, 14341–4.

(27) Cotts, R. M.; Hoch, M. J. R.; Sun, T; Markert, J. T. I. *J. Magn. Reson.* **1989**, *266*, 252–266.

(41) Pusch, A.-K.; Splith, T.; Moschkowitz, L.; Karmakar, S.; Biniwale, R.; Sant, M.; Suffritti, G. B.; Demontis, P.; Cravillon, J.; Pantatosaki, E.; Stallmach, F. *Adsorption* **2012**, *18*, 359–366.

(60) Plimpton, S. *J. Comput. Phys.* **1995**, *117*, 1–42.

(65) Wick, C. D.; Martin, M. G.; Siepmann, J. I. *J. Phys. Chem. B* **2000**, *104*, 8008–8016.

(104) Krishna, R.; van Baten, J. M. *Phys. Chem. Chem. Phys.* **2013**, *15*, 7994–8016.

(105) Chmelik, C. *Microporous Mesoporous Mater.* **2015**, DOI: `10.1016/j.micromeso.2015.05.008`.

(106) Sutrisno, A.; Huang, Y. *Solid State Nucl. Magn. Reson.* **2013**, *49-50*, 1–11.

(107) Wang, C.; Liu, D.; Lin, W. *J. Am. Chem. Soc.* **2013**, 130814191409007.

(108) Kuppler, R. J.; Timmons, D. J.; Fang, Q.-R.; Li, J.-R.; Makal, T. a.; Young, M. D.; Yuan, D.; Zhao, D.; Zhuang, W.; Zhou, H.-C. *Coord. Chem. Rev.* **2009**, *253*, 3042–3066.

(109) Schoedel, A.; Ji, Z.; Yaghi, O. M. *Nat. Energy* **2016**, *1*, 16034.

(110) Mason, J. a.; Veenstra, M.; Long, J. R. *Chem. Sci.* **2014**, *5*, 32.

(111) Wu, H.; Zhou, W.; Yildirim, T. *J. Am. Chem. Soc.* **2009**, *131*, 4995–5000.

(112) Mercado, R.; Vlaisavljevich, B.; Lin, L.-c.; Lee, K.; Lee, Y.; Mason, J. A.; Xiao, D. J.; Gonzalez, M. I.; Kapelewski, M. T.; Neaton, J. B.; Smit, B. *J. Phys. Chem. C* **2016**, acs.jpcc.6b03393.

(113) Chen, D. L.; Shang, H.; Zhu, W.; Krishna, R. *Chem. Eng. Sci.* **2015**, *124*, 109–117.

(114) Kaerger, J.; Caro, J.; Cool, P.; Coppens, M.-O.; Jones, D.; Kapteijn, F.; Rodr\'\iguez-Reinoso, F.; Stoecker, M.; Theodorou, D.; Vansant, E. F.; Others *Chem. Eng. & Technol.* **2009**, *32*, 1494–1511.

(115) Stallmach, F.; Pusch, A.-K. K.; Splith, T.; Horch, C.; Merker, S. *Microporous Mesoporous Mater.* **2015**, *205*, 36–39.

(116) Rappé, A. K.; Casewit, C. J.; Colwell, K. S.; Goddard III, W.; Skiff, W. *J. Am. Chem. Soc.* **1992**, *114*, 10024–10035.

(117) Childs, H. et al. In *High Performance Visualization–Enabling Extreme-Scale Scientific Insight*, 2012, pp 357–372.

(118) Trappenieks, N. J. **1971**, *51*, 418–431.

(119) Jackowski, K.; Jaszunski, M., *Gas Phase NMR*; Jackowski, K., Jaszunski, M., Eds.; Royal Society of Chemistry: Cambridge, UK, 2016.

(120) Kowalewski, J., *Nuclear Spin Relaxation in Diamagnetic Fluids. Part 1. General Aspects and Inorganic Applications*; C, 1990; Vol. 22, pp 307–414.

Appendix A

Supporting Information for Translational and Rotational Motion of C8 Aromatics Adsorbed in Isotropic Porous Media (MOF-5): NMR Studies and MD Simulations

A.1 Supporting Simulated and Experimental Data

Table 1: Summary of Experimental and Simulated Translational Self-Diffusion Coefficients as a function of temperature

NMR Apparent Self-Diffusion Coefficients $[m^2 s^{-1}]$			
Temperature (K)	p-xylene	m-xylene	o-xylene
253	$1.558 \pm 0.0001 \times 10^{-10}$	$0.980 \pm 0.0001 \times 10^{-10}$	$0.722 \pm 0.009 \times 10^{-10}$
263	$2.457 \pm 0.061 \times 10^{-10}$	$1.390 \pm 0.018) \times 10^{-10}$	$1.079 \pm 0.005 \times 10^{-10}$
273	$2.593 \pm 0.002 \times 10^{-10}$	$1.907 \pm 0.004 \times 10^{-10}$	$1.559 \pm 0.011 \times 10^{-10}$
283	$3.657 \pm 0.005 \times 10^{-10}$	$2.579 \pm 0.018 \times 10^{-10}$	$2.152 \pm 0.022 \times 10^{-10}$
293	$4.18 \pm 0.01 \times 10^{-10}$	$3.747 \pm 0.026 \times 10^{-10}$	$2.823 \pm 0.098 \times 10^{-10}$

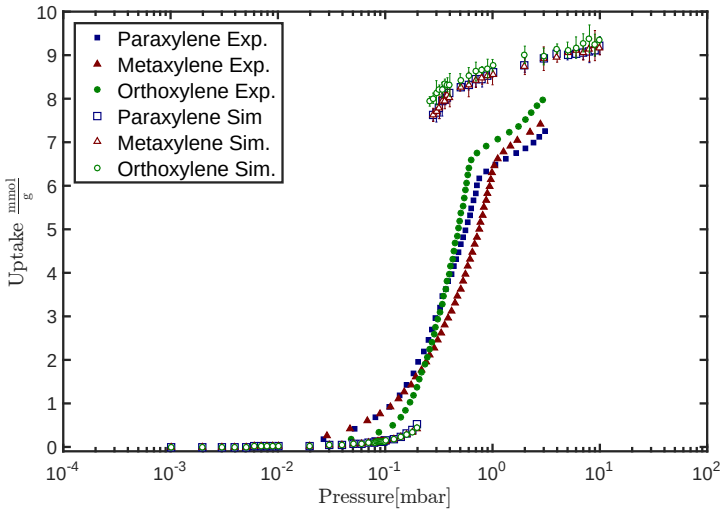

Figure 1: Experimental and simulated pure-component gas adsorption isotherms of the three xylene isomers in MOF-5, taken at 25 °C. Experimental gas phase adsorption isotherms were measured by a volumetric method using a Micromeritics 3Flex gas sorption analyzer. A typical sample of ca. 50 mg of metal-organic framework (MOF) was transferred in a nitrogen-filled glovebox to a pre-weighed analysis tube, which was capped with a Micromeretics TranSeal and evacuated by heating to 150 °C with a ramp rate of 1 °C min^{-1} under dynamic vacuum until an outgas rate of less than 2 µbar min^{-1} was achieved. The evacuated analysis tube containing the degassed sample was then transferred to an electronic balance and weighed again to determine the mass of sample. The tube was then transferred back to the analysis port of the gas adsorption instrument, where the outgas rate was confirmed to be less than 2 µbar min^{-1}. For all isotherms, free space correction measurements were performed using ultrahigh purity (UHP, 99.999 %) helium gas. Pure component xylene vapor was prepared by thoroughly degassing liquid xylene by freezing the xylene, pumping on the headspace for 10 min, allowing the xylene to fully thaw, and repeating this freeze-pump-thaw cycle 3 more times. Isotherms collected were measured using an isothermal water bath. Oil-free vacuum pumps and oil-free pressure regulators were used for all measurements to prevent contamination of the. Simulated gas adsorption isotherms were obtained with grand canonical Monte Carlo simulations using the same force field as was used with the MD simulations. Data were collected over 1,000,000 cycles following 1,000,000 equilibration cycles. The simulation box consisted of 1 unit cell of MOF-5.

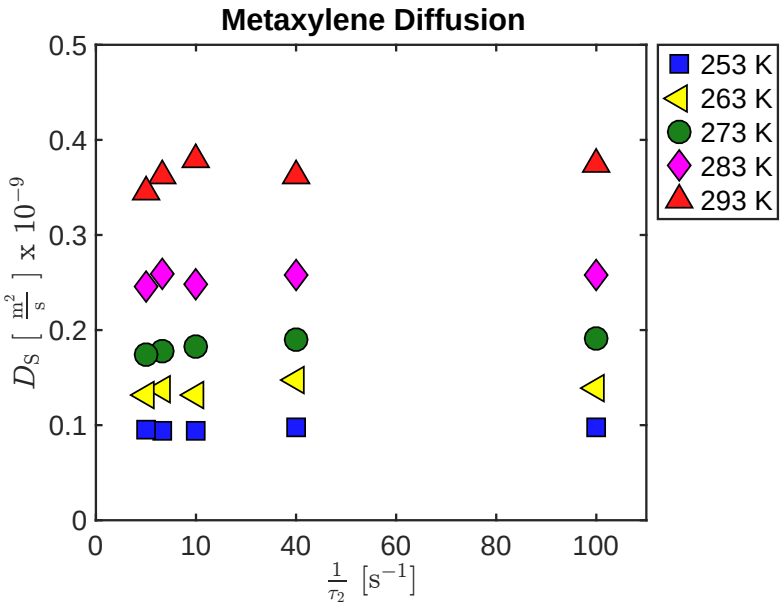

Figure 2: The self-diffusion coefficient of metaxylene versus diffusion time at various temperatures.

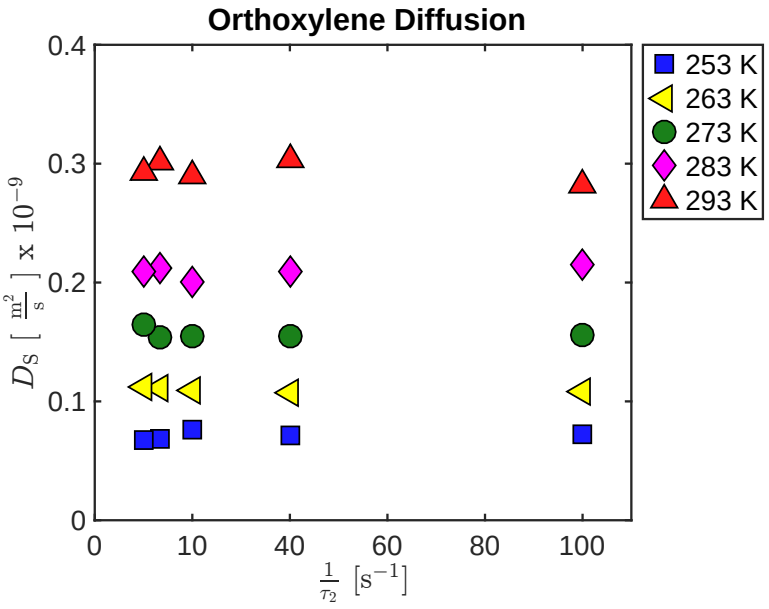

Figure 3: The self-diffusion coefficient of orthoxylene versus diffusion time at various temperatures.

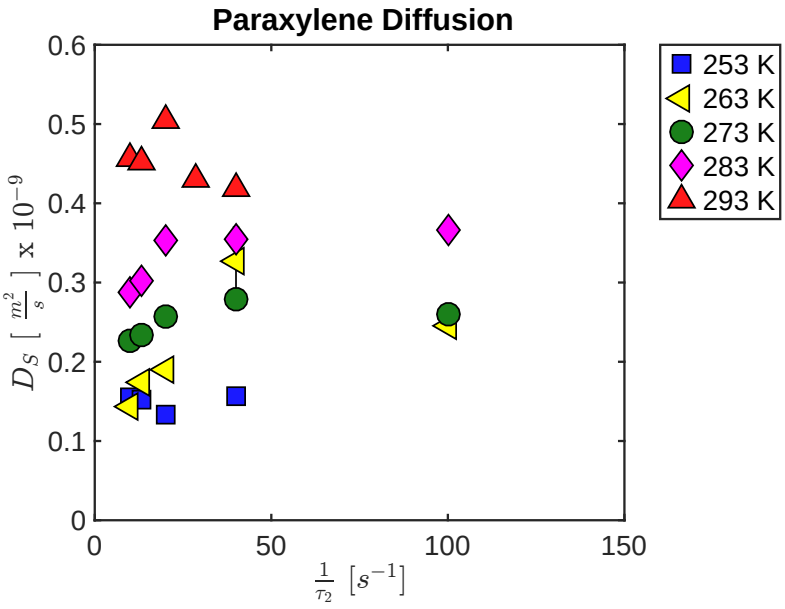

Figure 4: The self-diffusion coefficient of paraxylene versus diffusion time at various temperatures.

Appendix B

Design and Construction of In Situ Gas Dosing Apparatus

B.1 Motivation

Thermodynamically Define States

The thermodynamic state of an adsorbate-adsorbent systems is defined by the following quantities, T, temperature, θ_i, adsorbate (i) loading, and the pressure of the systems. Physically control 2 of the these thermodynamic variables experimentally will fix the state of the system. This is essential for all measurements of adsorbate dynamics because all measurements are dependent on the state of the systems. Although extensive work has been done in the field of NMR probe development in order to develop solid state in situ probes and specialized setups for catalysis, zero in situ apparatuses have been developed for NMR gas adsorption and diffusion measurements. However, as we start to investigate materials whose adsorption isotherms are greatly sensitive at low and moderate pressure to fluctuation in temperature and pressure, it becomes more essential to accurately determine the experimental thermodynamic state of our system during measurement2. The most common way to classify the state of an adsorbent in solid-state materials is to identify where on the isotherm the system is located. In order to do this we must have a well-defined pressure and temperature of our system. In most gas-adsorbed systems studied in NMR the experimental loading methodology proceeds in this manner: (1) the adsorbent is activated under vacuum and high temperature; (2) the sample gas is exposed at a known pressure to the activated adsorbent; (3) the NMR tube is flame sealed through cryo-pumping. Then experimentalist proceeded to vary the temperature of the sealed

container (which will cause the system to deviate in pressure as well) as they perform experiments that then determine the correlation time, diffusion coefficient, and other relaxation parameter.

The actual loading of the adsorbent material can be back calculated if the initial pressure of the system is well known, but this is often not the practice of most experimentalists. Thus, although the previous measurements of gases in MOFs have been valuable for room temperature order of magnitude estimates of diffusion coefficients as well as general trends with temperature change, because the pressure of theses systems was not well defined, the actual loading of the MOF can differ greatly from what was reported. Also, as these novel MOF materials have been found to be extremely sensitive to the moisture content of air,it is important that the system remain well-isolated from impurities. This small but important factor is often ignored in NMR adsorption gas studies. By ignoring the change in the loading on the molecules due to a macroscopic change in temperature we are ignoring the effects of loading on the transport mechanism experimentally observed during the experiment. In my thesis I will present the solution to this problem. The solution is to perform in situ NMR experiments where the thermodynamic states of the system (P, T) are controlled while allowing the adsorbed species to fluctuate based on the known adsorption isotherm in the literature. In other words, an isobaric and isothermal system that allows us control the loading and simultaneously measure the diffusion coefficient will allows us to better discern the effects of loading and operating conditions on the transport mechanism. An in situ apparatus for diffusometry measurement offers several advantages; (1) Minimum necessary sample that can be exposed to many temperature pressures and loadings. Usually to access four different operating conditions, four different samples must be made. NMR experiments are most efficient when a lot of sample can be used to increase the density of observed spins and filling the volume of the RF coil is not always possible if sample must be conserved for multiple experimental conditions; (2) Using the same sample eliminates artifacts from batch to batch deviation in crystal size or sample quality; (3) An in situ apparatus that offers active pressure and temperature control is the best set up for measurements of intracrystalline diffusion coefficient to compare with the results of molecular dynamic simulation where their systems are often defined with constant pressure, closed volume, and constant temperature.

B.2 Technical Specifications

Schematics of the InSitu Apparatus

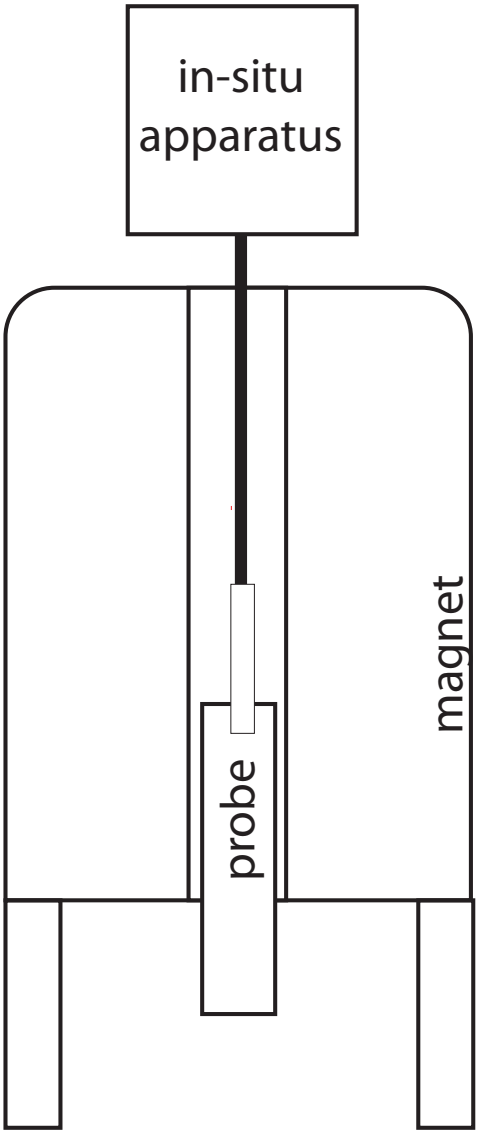

Figure 1: Simple Schematic of the in situ demonstrating what it look like in lab.

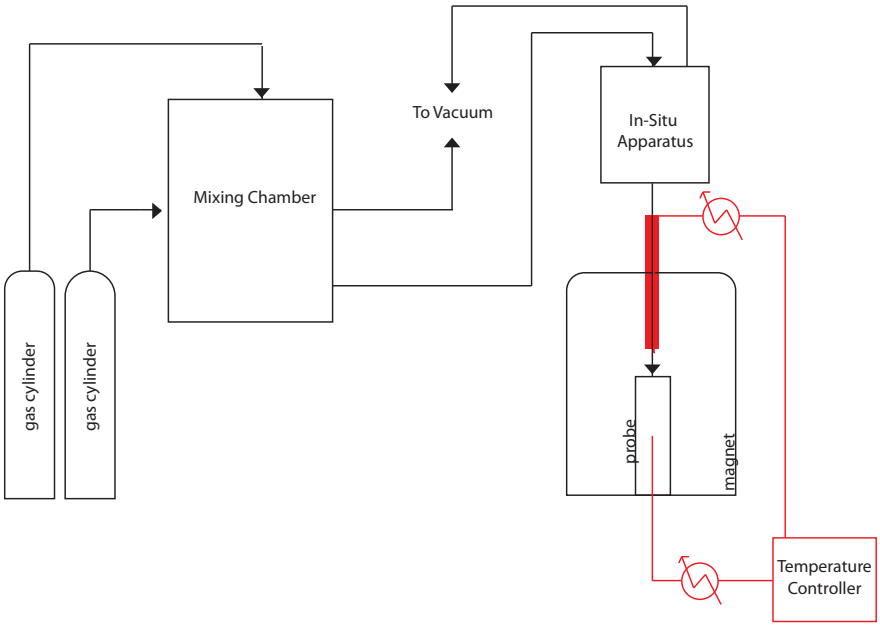

Figure 2: Simple Schematic of the in situ demonstrating all the parts.

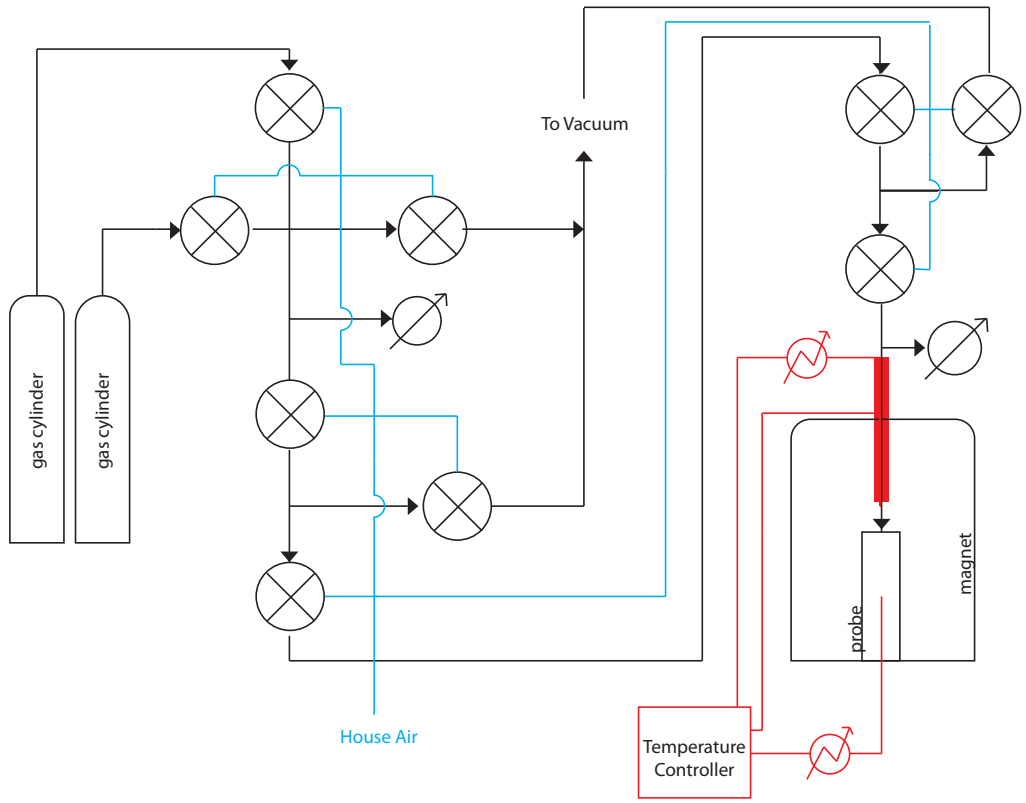

Figure 3: Simple Schematic of the in situ demonstrating with the location of the pneumatically activated valves.

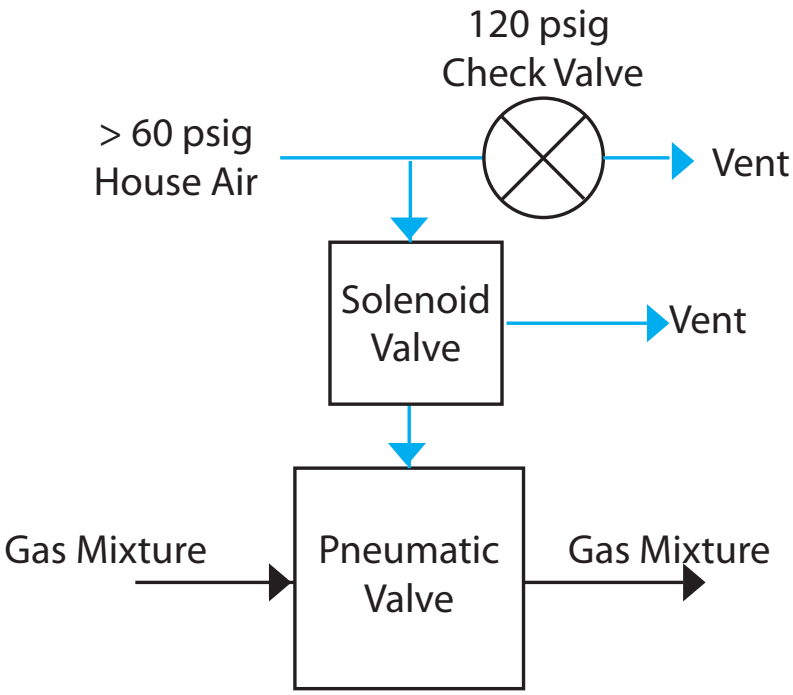

Figure 4: Simple Schematic of the pneumatically activated valves.

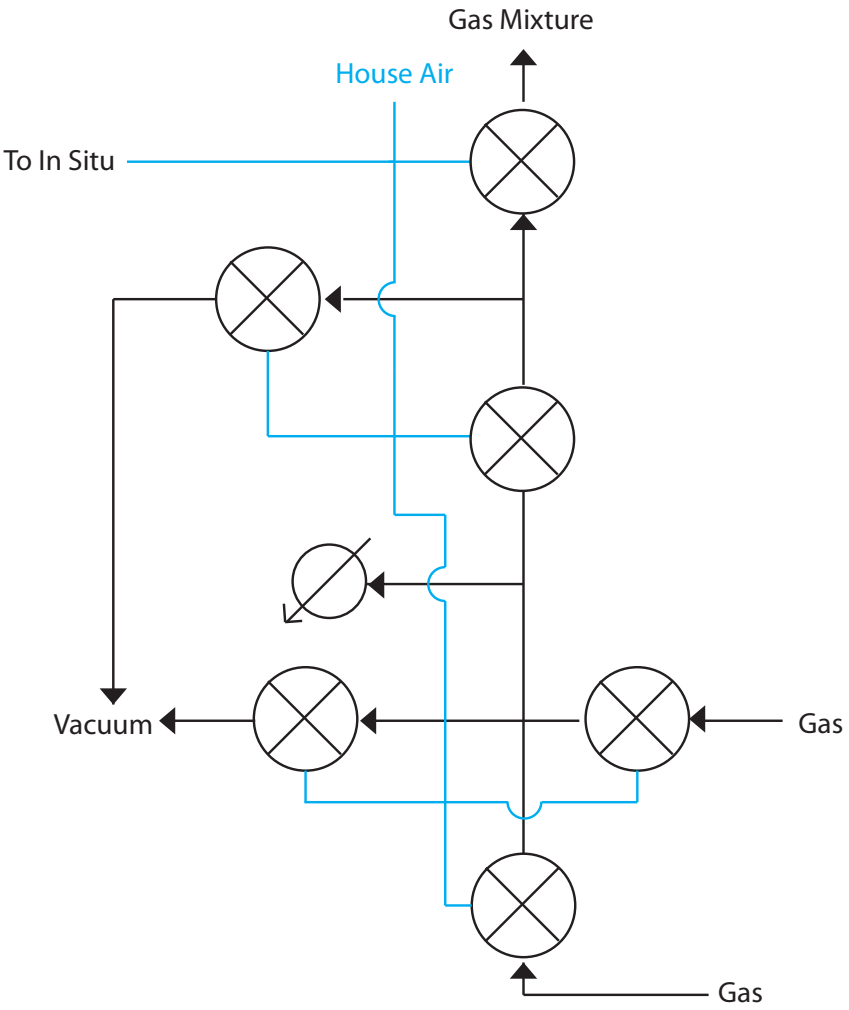

Figure 5: Simple Schematic of the mixing chamber.

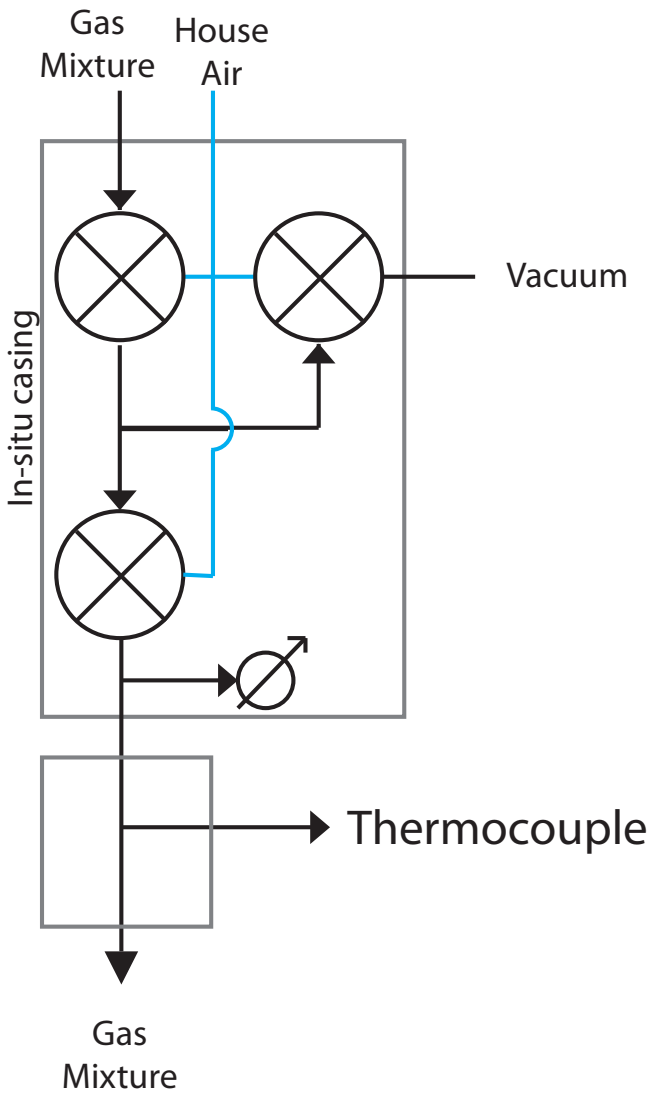

Figure 6: Simple Schematic of the dosing chamber that is magnetically shielded.

B.3 Alignment Achievements

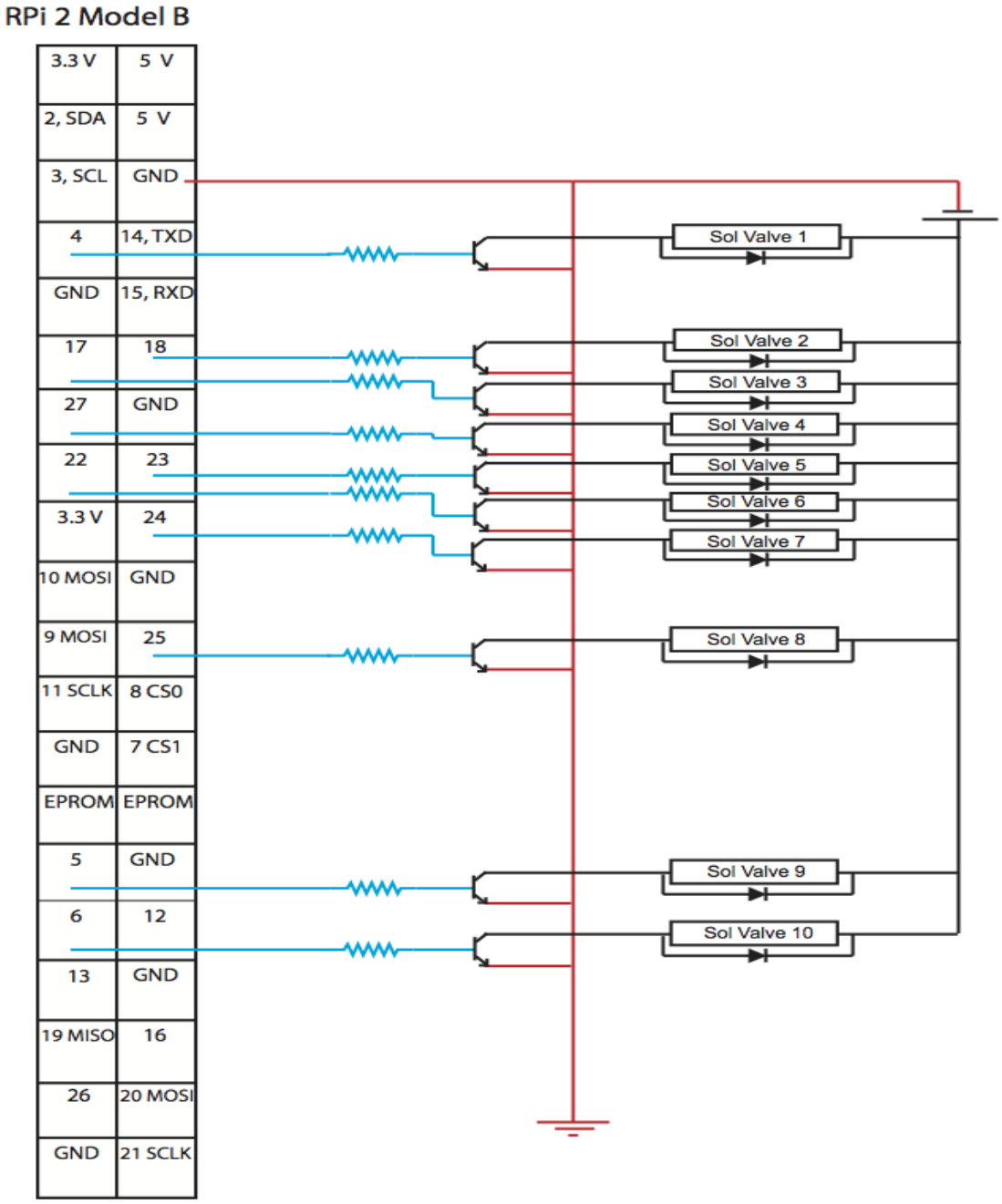

Figure 7: Schematic of the circuit board controlling the apparatus.

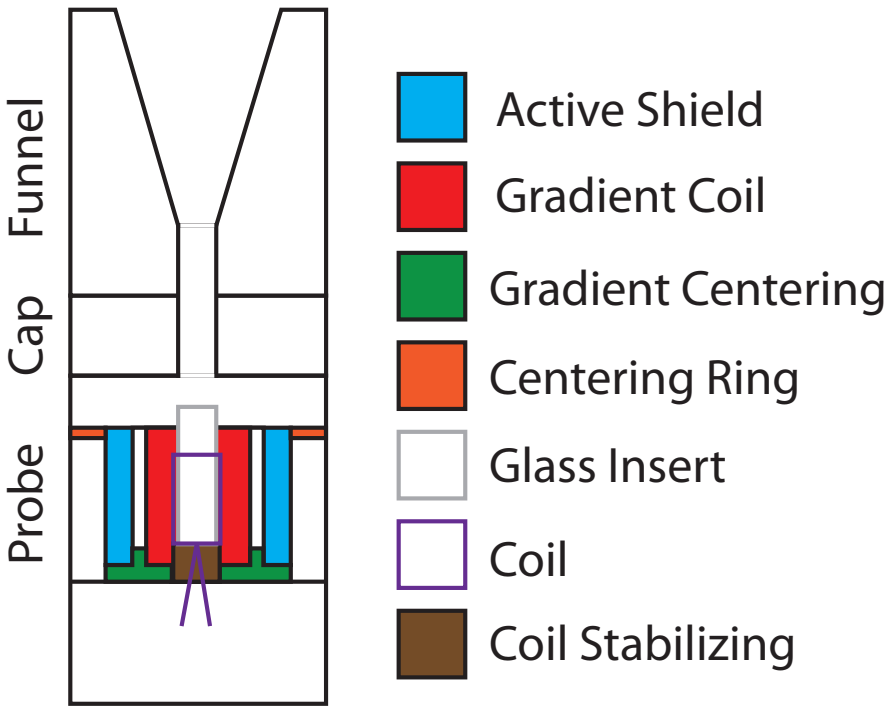

Figure 8: Simple Schematic of the alignment with the probe.

Appendix C

Selected Measurements of Adsorbate Self Diffusivity in MOFs

Table 1: Summary of Reported Literature Values of Adsorbates Diffusivities in MOFs

Dosing			Temp.	Diffusivity		Meas.	Ref.
Amount	Unit	Method		Value	Type	Method	
Reported Diffusivities for Adsorbates in MOF-5 (Zn_2(bdc))							
Benzene							
10	molec. /u.c.	Ex-Situ (sealed)	221.4	4.0876E-11	D_{S-eff}	NMR PFG	[121]
10	molec. /u.c.	Ex-Situ (sealed)	235.9	7.0329E-11	D_{S-eff}	NMR PFG	[121]
10	molec. /u.c.	Ex-Situ (sealed)	249.0	1.2279E-10	D_{S-eff}	NMR PFG	[121]
10	molec. /u.c.	Ex-Situ (sealed)	253.0	3.8109E-10	D_{S-eff}	NMR PFG	[121]
20	molec. /u.c.	Ex-Situ (sealed)	253.0	1.5185E-10	D_{S-eff}	NMR PFG	[121]

Continued on Next Page...

Table 1 – continued from previous page

Dosing			Temp.	Diffusivity		Meas.	Ref.
Amount	Unit	Method		Value	Type	Method	
32	molec. /u.c.	Ex-Situ (sealed)	253.0	1.3180E-10	D_{S-eff}	NMR PFG	[121]
56	molec. /u.c.	Ex-Situ (sealed)	253.0	1.3726E-10	D_{S-eff}	NMR PFG	[121]
10	molec. /u.c.	Ex-Situ (sealed)	261.7	2.3411E-10	D_{S-eff}	NMR PFG	[121]
32	molec. /u.c.	Ex-Situ (sealed)	273.0	3.5400E-10	D_{S-eff}	NMR PFG	[121]
32	molec. /u.c.	Ex-Situ (sealed)	273.0	9.2000E-11	D_{S-eff}	NMR PFG	[121]
10	molec. /u.c.	Ex-Situ (sealed)	273.3	4.0281E-10	D_{S-eff}	NMR PFG	[121]
56	molec. /u.c.	Ex-Situ (sealed)	273.3	2.0516E-10	D_{S-eff}	NMR PFG	[121]
20	molec. /u.c.	Ex-Situ (sealed)	273.8	1.5989E-10	D_{S-eff}	NMR PFG	[121]
10	molec. /u.c.	Ex-Situ (sealed)	293.2	9.0243E-10	D_{S-eff}	NMR PFG	[121]
56	molec. /u.c.	Ex-Situ (sealed)	293.2	3.4279E-10	D_{S-eff}	NMR PFG	[121]
32	molec. /u.c.	Ex-Situ (sealed)	293.7	3.5300E-10	D_{S-eff}	NMR PFG	[121]

Continued on Next Page...

Table 1 – continued from previous page

Dosing			Temp.	Diffusivity		Meas.	Ref.
Amount	Unit	Method		Value	Type	Method	
20	molec. /u.c.	Ex-Situ (sealed)	294.2	4.3986E-10	D_{S-eff}	NMR PFG	[121]
7	molec. /u.c.	Ex-Situ (sealed)	298.0	1.8193E-09	D_{S-eff}	NMR PFG	[121]
7	molec. /u.c.	Ex-Situ (sealed)	298.0	9.0900E-10	D_{Smic}	MAS NMR PFG	[121]
7	molec. /u.c.	Ex-Situ (sealed)	298.0	8.3000E-11	D_{Smic}	MAS NMR PFG	[121]
10	molec. /u.c.	Ex-Situ (sealed)	298.0	2.2045E-09	D_{S-eff}	NMR PFG	[121]
20	molec. /u.c.	Ex-Situ (sealed)	298.0	7.3785E-10	D_{S-eff}	NMR PFG	[121]
32	molec. /u.c.	Ex-Situ (sealed)	298.0	7.0700E-10	D_{S-eff}	NMR PFG	[121]
32	molec. /u.c.	Ex-Situ (sealed)	298.0	1.7900E-10	D_{S-eff}	NMR PFG	[121]
32	molec. /u.c.	Ex-Situ (sealed)	298.0	7.0142E-10	D_{S-eff}	NMR PFG	[121]
56	molec. /u.c.	Ex-Situ (sealed)	298.0	7.1964E-10	D_{S-eff}	NMR PFG	[121]
6	molec. /u.c.	Ex-Situ (sealed)	298.0	1.3000E-09	D_{S-eff}	NMR PFG	[121]

Continued on Next Page...

Table 1 – continued from previous page

Dosing			Temp.	Diffusivity		Meas.	Ref.
Amount	Unit	Method		Value	Type	Method	
6	molec. /u.c.	Ex-Situ (sealed)	298.0	1.4000E-09	D_{S-eff}	NMR PFG	[121]
6	molec. /u.c.	Ex-Situ (sealed)	298.0	1.8000E-09	$_{Sintra}$	NMR PFG	[121]
6	molec. /u.c.	Ex-Situ (sealed)	298.0	2.0000E-10	$_{Sintra}$	NMR PFG	[121]
6	molec. /u.c.	Ex-Situ (sealed)	298.0	3.5000E-10	$_{Sintra}$	NMR PFG	[121]
6	molec. /u.c.	Ex-Situ (sealed)	298.0	4.0000E-10	$_{Sintra}$	NMR PFG	[121]
10	molec. /u.c.	Ex-Situ (sealed)	308.0	3.4980E-09	D_{S-eff}	NMR PFG	[121]
20	molec. /u.c.	Ex-Situ (sealed)	308.0	8.8360E-10	D_{S-eff}	NMR PFG	[121]
32	molec. /u.c.	Ex-Situ (sealed)	308.0	8.7900E-10	D_{S-eff}	NMR PFG	[121]
32	molec. /u.c.	Ex-Situ (sealed)	308.0	2.2000E-10	D_{S-eff}	NMR PFG	[121]
32	molec. /u.c.	Ex-Situ (sealed)	308.0	8.6538E-10	D_{S-eff}	NMR PFG	[121]
56	molec. /u.c.	Ex-Situ (sealed)	308.0	7.7429E-10	D_{S-eff}	NMR PFG	[121]

Continued on Next Page...

Table 1 – continued from previous page

Dosing			Temp.	Diffusivity		Meas.	Ref.
Amount	Unit	Method		Value	Type	Method	
20	molec. /u.c.	Ex-Situ (sealed)	310.7	6.5356E-10	D_{S-eff}	NMR PFG	[121]
56	molec. /u.c.	Ex-Situ (sealed)	311.7	7.1368E-10	D_{S-eff}	NMR PFG	[121]
10	molec. /u.c.	Ex-Situ (sealed)	314.6	2.1756E-09	D_{S-eff}	NMR PFG	[121]
32	molec. /u.c.	Ex-Situ (sealed)	315.0	7.1368E-10	D_{S-eff}	NMR PFG	[121]
10	molec. /u.c.	Ex-Situ (sealed)	318.0	4.3178E-09	D_{S-eff}	NMR PFG	[121]
20	molec. /u.c.	Ex-Situ (sealed)	318.0	1.0202E-09	D_{S-eff}	NMR PFG	[121]
32	molec. /u.c.	Ex-Situ (sealed)	318.0	1.1300E-09	D_{S-eff}	NMR PFG	[121]
32	molec. /u.c.	Ex-Situ (sealed)	318.0	2.7400E-10	D_{S-eff}	NMR PFG	[121]
32	molec. /u.c.	Ex-Situ (sealed)	318.0	1.0840E-09	D_{S-eff}	NMR PFG	[121]
56	molec. /u.c.	Ex-Situ (sealed)	318.0	1.0020E-09	D_{S-eff}	NMR PFG	[121]
56	molec. /u.c.	Ex-Situ (sealed)	322.3	7.9084E-10	D_{S-eff}	NMR PFG	[121]

Continued on Next Page...

Table 1 – continued from previous page

Dosing			Temp.	Diffusivity		Meas.	Ref.
Amount	Unit	Method		Value	Type	Method	
10	molec. /u.c.	Ex-Situ (sealed)	322.8	3.4279E-09	D_{S-eff}	NMR PFG	[121]
20	molec. /u.c.	Ex-Situ (sealed)	322.8	9.1576E-10	D_{S-eff}	NMR PFG	[121]
32	molec. /u.c.	Ex-Situ (sealed)	322.8	8.6359E-10	D_{S-eff}	NMR PFG	[121]
32	molec. /u.c.	Ex-Situ (sealed)	328.0	1.5100E-09	D_{S-eff}	NMR PFG	[121]
32	molec. /u.c.	Ex-Situ (sealed)	328.0	4.1600E-10	D_{S-eff}	NMR PFG	[121]
56	molec. /u.c.	Ex-Situ (sealed)	329.6	9.5696E-10	D_{S-eff}	NMR PFG	[121]
10	molec. /u.c.	Ex-Situ (sealed)	330.1	4.2092E-09	D_{S-eff}	NMR PFG	[121]
32	molec. /u.c.	Ex-Situ (sealed)	330.1	1.1245E-09	D_{S-eff}	NMR PFG	[121]
56	molec. /u.c.	Ex-Situ (sealed)	336.4	1.1081E-09	D_{S-eff}	NMR PFG	[121]
20	molec. /u.c.	Ex-Situ (sealed)	336.9	1.2100E-09	D_{S-eff}	NMR PFG	[121]
32	molec. /u.c.	Ex-Situ (sealed)	336.9	1.4858E-09	D_{S-eff}	NMR PFG	[121]

Continued on Next Page...

Table 1 – continued from previous page

Dosing			Temp.	Diffusivity		Meas.	Ref.
Amount	Unit	Method		Value	Type	Method	
10	molec. /u.c.	Ex-Situ (sealed)	337.4	9.5696E-10	D_{S-eff}	NMR PFG	[121]
CO_2							
		In-Situ	295.7	8.1700E-13	D_T	Uptake	[122]
		In-Situ	304.7	9.5700E-13	D_T	Uptake	[122]
		In-Situ	313.7	1.0260E-12	D_T	Uptake	[122]
		In-Situ	331.7	1.1540E-12	D_T	Uptake	[122]
Dodecane							
6	molec. /u.c.	Ex-Situ (sealed)	298.0	2.475E-10	D_{S-eff}	NMR PFG	[123]
Ethane							
120	molec. /u.c.	Ex-Situ (sealed)	223.0	0.0000014	D_{S-eff}	NMR PFG	[16]
120	molec. /u.c.	Ex-Situ (sealed)	223.0	0.000000019	D_{S-eff}	NMR PFG	[16]
120	molec. /u.c.	Ex-Situ (sealed)	223.0	4.7E-09	D_{S-eff}	NMR PFG	[16]
120	molec. /u.c.	Ex-Situ (sealed)	298.0	0.0000002	D_{S-eff}	NMR PFG	[16]
25	molec. /u.c.	Ex-Situ (sealed)	223.0	2.06072E-08	D_{S-eff}	NMR PFG	[123]
Hexadecane							

Continued on Next Page...

Table 1 – continued from previous page

Dosing			Temp.	Diffusivity		Meas.	Ref.
Amount	Unit	Method		Value	Type	Method	
4.5	molec. /u.c.	Ex-Situ (sealed)	298.0	1.14376E-10	D_{S-eff}	NMR PFG	[123]
Hexane							
100	molec. /u.c.	Ex-Situ (sealed)	298.0	1.8E-09	D_{S-eff}	NMR PFG	[16]
100	molec. /u.c.	Ex-Situ (sealed)	298.0	2.6E-09	D_{S-eff}	NMR PFG	[16]
100	molec. /u.c.	Ex-Situ (sealed)	298.0	3.2E-09	D_{S-eff}	NMR PFG	[16]
100	molec. /u.c.	Ex-Situ (sealed)	298.0	4.1E-09	D_{S-eff}	NMR PFG	[16]
100	molec. /u.c.	Ex-Situ (sealed)	298.0	4E-10	D_{S-eff}	NMR PFG	[16]
100	molec. /u.c.	Ex-Situ (sealed)	298.0	4.5E-10	D_{S-eff}	NMR PFG	[16]
6.3	molec. /u.c.	Ex-Situ (sealed)	298.0	3.11981E-09	D_{S-eff}	NMR PFG	[123]
Methane							
120	molec. /u.c.	Ex-Situ (sealed)	173.0	0.00000019	D_{S-eff}	NMR PFG	[16]
120	molec. /u.c.	Ex-Situ (sealed)	298.0	0.000002	D_{S-eff}	NMR PFG	[16]

Continued on Next Page...

Table 1 – continued from previous page

Dosing Amount	Dosing Unit	Method	Temp.	Diffusivity Value	Diffusivity Type	Meas. Method	Ref.
46	molec. /u.c.	Ex-Situ (sealed)	298.0	1.68178E-07	D_{S-eff}	NMR PFG	[123]
Hexane in Benzene							
mixture		Ex-Situ (sealed)	298.0	9.49E-10	D_{Smic}	MAS NMR PFG	[124]
mixture		Ex-Situ (sealed)	298.0	9.5E-11	D_{Smic}	MAS NMR PFG	[124]
Reported Diffusivities for Adsorbates in CuBTC (HKUST-1)							
1-Butene							
20.00	molec./ u.c	Ex-Situ (sealed)	–	3.2000E-08	$D_{S_{App}}$	NMR PFG	[125]
20.00	molec./ u.c	Ex-Situ (sealed)	298	6.7000E-11	$D_{S_{App}}$	NMR PFG	[125]
2-methyly-butane							
0.067	θ_i	In-Situ	298	6.2275E-13	$D_{T_{intra}}$	IRM	[126]
0.106	θ_i	In-Situ	298	1.0123E-12	$D_{T_{intra}}$	IRM	[126]
0.141	θ_i	In-Situ	298	1.1115E-12	$D_{T_{intra}}$	IRM	[126]
0.171	θ_i	In-Situ	298	1.2668E-12	$D_{T_{intra}}$	IRM	[126]
0.190	θ_i	In-Situ	298	1.6456E-12	$D_{T_{intra}}$	IRM	[126]
0.214	θ_i	In-Situ	298	1.4988E-12	$D_{T_{intra}}$	IRM	[126]

Continued on Next Page...

Table 1 – continued from previous page

Dosing			Temp.	Diffusivity		Meas.	Ref.
Amount	Unit	Method		Value	Type	Method	
0.232	θ_i	In-Situ	298	1.6456E-12	$D_{T_{intra}}$	IRM	[126]
0.248	θ_i	In-Situ	298	1.5852E-12	$D_{T_{intra}}$	IRM	[126]
0.257	θ_i	In-Situ	298	1.4438E-12	$D_{T_{intra}}$	IRM	[126]
0.267	θ_i	In-Situ	298	1.5852E-12	$D_{T_{intra}}$	IRM	[126]
0.276	θ_i	In-Situ	298	1.3398E-12	$D_{T_{intra}}$	IRM	[126]
0.287	θ_i	In-Situ	298	1.1977E-12	$D_{T_{Fick-intra}}$	IRM	[126]
0.308	θ_i	In-Situ	298	1.0509E-12	$D_{T_{Fick-intra}}$	IRM	[126]
0.341	θ_i	In-Situ	298	9.5713E-13	$D_{T_{Fick-intra}}$	IRM	[126]
0.390	θ_i	In-Situ	298	6.8374E-13	$D_{T_{Fick-intra}}$	IRM	[126]
0.451	θ_i	In-Situ	298	5.3627E-13	$D_{T_{Fick-intra}}$	IRM	[126]
0.541	θ_i	In-Situ	298	2.5875E-13	$D_{T_{Fick-intra}}$	IRM	[126]
0.614	θ_i	In-Situ	298	1.6523E-13	$D_{T_{Fick-intra}}$	IRM	[126]
0.687	θ_i	In-Situ	298	1.0954E-13	$D_{T_{Fick-intra}}$	IRM	[126]
0.757	θ_i	In-Situ	298	5.4639E-13	$D_{T_{Fick-intra}}$	IRM	[126]
0.844	θ_i	In-Situ	298	1.5559E-12	$D_{T_{Fick-intra}}$	IRM	[126]
0.916	θ_i	In-Situ	298	2.4824E-12	$D_{T_{Fick-intra}}$	IRM	[126]
0.949	θ_i	In-Situ	298	4.8645E-12	$D_{T_{Fick-intra}}$	IRM	[126]

Continued on Next Page...

Table 1 – continued from previous page

Dosing			Temp.	Diffusivity		Meas.	Ref.
Amount	Unit	Method		Value	Type	Method	
0.965	θ_i	In-Situ	298	1.3097E-11	$D_{T_{Fick-intra}}$	IRM	[126]
0.987	θ_i	In-Situ	298	8.2087E-12	$D_{T_{Fick-intra}}$	IRM	[126]
Ethane							
1	bar?	Ex-Situ (sealed)	327.9	6.5704E-08	$D_{S_{App}}$	NMR PFG	[127]
1	bar?	Ex-Situ (sealed)	317.9	6.3351E-08	$D_{S_{App}}$	NMR PFG	[127]
1	bar?	Ex-Situ (sealed)	307.8	5.7985E-08	$D_{S_{App}}$	NMR PFG	[127]
1	bar?	Ex-Situ (sealed)	298.0	5.1228E-08	$D_{S_{App}}$	NMR PFG	[127]
iso-Butane							
0.022	θ_i	In-Situ	298	9.3941E-13	$D_{T_{Fick-intra}}$	IRM	[126]
0.040	θ_i	In-Situ	298	1.2668E-12	$D_{T_{Fick-intra}}$	IRM	[126]
0.057	θ_i	In-Situ	298	1.5852E-12	$D_{T_{Fick-intra}}$	IRM	[126]
0.076	θ_i	In-Situ	298	1.5559E-12	$D_{T_{Fick-intra}}$	IRM	[126]
0.103	θ_i	In-Situ	298	1.7405E-12	$D_{T_{Fick-intra}}$	IRM	[126]
0.129	θ_i	In-Situ	298	1.8409E-12	$D_{T_{Fick-intra}}$	IRM	[126]
0.149	θ_i	In-Situ	298	2.4824E-12	$D_{T_{Fick-intra}}$	IRM	[126]

Continued on Next Page...

Table 1 – continued from previous page

Dosing			Temp.	Diffusivity		Meas.	Ref.
Amount	Unit	Method		Value	Type	Method	
0.194	θ_i	In-Situ	298	2.6751E-12	$D_{T_{Fick-intra}}$	IRM	[126]
0.229	θ_i	In-Situ	298	3.6754E-12	$D_{T_{Fick-intra}}$	IRM	[126]
0.268	θ_i	In-Situ	298	3.3475E-12	$D_{T_{Fick-intra}}$	IRM	[126]
0.329	θ_i	In-Situ	298	6.6835E-12	$D_{T_{Fick-intra}}$	IRM	[126]
0.422	θ_i	In-Situ	298	7.0689E-12	$D_{T_{Fick-intra}}$	IRM	[126]
0.537	θ_i	In-Situ	298	1.0082E-11	$D_{T_{Fick-intra}}$	IRM	[126]
0.654	θ_i	In-Situ	298	7.0689E-12	$D_{T_{Fick-intra}}$	IRM	[126]
0.740	θ_i	In-Situ	298	8.2087E-12	$D_{T_{Fick-intra}}$	IRM	[126]
0.800	θ_i	In-Situ	298	2.0129E-11	$D_{T_{Fick-intra}}$	IRM	[126]
0.841	θ_i	In-Situ	298	2.3375E-11	$D_{T_{Fick-intra}}$	IRM	[126]
0.884	θ_i	In-Situ	298	2.7144E-11	$D_{T_{Fick-intra}}$	IRM	[126]
0.905	θ_i	In-Situ	298	6.7818E-11	$D_{T_{Fick-intra}}$	IRM	[126]
0.925	θ_i	In-Situ	298	7.8753E-11	$D_{T_{Fick-intra}}$	IRM	[126]
0.949	θ_i	In-Situ	298	8.2955E-10	$D_{T_{Fick-intra}}$	IRM	[126]
0.959	θ_i	In-Situ	298	9.2798E-10	$D_{T_{Fick-intra}}$	IRM	[126]
0.973	θ_i	In-Situ	298	2.1603E-10	$D_{T_{Fick-intra}}$	IRM	[126]
0.983	θ_i	In-Situ	298	9.4548E-10	$D_{T_{Fick-intra}}$	IRM	[126]

Continued on Next Page...

Table 1 – continued from previous page

Dosing			Temp.	Diffusivity		Meas.	Ref.
Amount	Unit	Method		Value	Type	Method	
Methane							
1	bar?	Ex-Situ (sealed)	327.9	9.7431E-08	$D_{S_{App}}$	NMR PFG	[127]
1	bar?	Ex-Situ (sealed)	317.9	9.6004E-08	$D_{S_{App}}$	NMR PFG	[127]
1	bar?	Ex-Situ (sealed)	307.9	9.3418E-08	$D_{S_{App}}$	NMR PFG	[127]
1	bar?	Ex-Situ (sealed)	298.0	9.0597E-08	$D_{S_{App}}$	NMR PFG	[127]
n-Butane							
20.00	molec./ u.c	Ex-Situ (sealed)	–	2.3000E-08	$D_{S_{App}}$	NMR PFG	[125]
20.00	molec./ u.c	Ex-Situ (sealed)	298	7.3000E-10	$D_{S_{App}}$	NMR PFG	[125]
5.00	molec./ u.c	Ex-Situ (sealed)	–	7.3000E-10	$D_{S_{Intra}}$	NMR PFG	[125]
0.017	θ_i	In-Situ	298	1.9110E-12	$D_{T_{Fick-intra}}$	IRM	[126]
0.037	θ_i	In-Situ	298	3.7447E-12	$D_{T_{Fick-intra}}$	IRM	[126]
0.052	θ_i	In-Situ	298	7.7612E-12	$D_{T_{Fick-intra}}$	IRM	[126]
0.068	θ_i	In-Situ	298	7.2022E-12	$D_{T_{Fick-intra}}$	IRM	[126]
0.095	θ_i	In-Situ	298	1.0663E-11	$D_{T_{Fick-intra}}$	IRM	[126]

Continued on Next Page...

Table 1 – continued from previous page

Dosing			Temp.	Diffusivity		Meas.	Ref.
Amount	Unit	Method		Value	Type	Method	
0.119	θ_i	In-Situ	298	1.6389E-11	$D_{T_{Fick-intra}}$	IRM	[126]
0.140	θ_i	In-Situ	298	2.0129E-11	$D_{T_{Fick-intra}}$	IRM	[126]
0.179	θ_i	In-Situ	298	2.6148E-11	$D_{T_{Fick-intra}}$	IRM	[126]
0.211	θ_i	In-Situ	298	3.7294E-11	$D_{T_{Fick-intra}}$	IRM	[126]
0.246	θ_i	In-Situ	298	2.7656E-11	$D_{T_{Fick-intra}}$	IRM	[126]
0.294	θ_i	In-Situ	298	3.3968E-11	$D_{T_{Fick-intra}}$	IRM	[126]
0.365	θ_i	In-Situ	298	3.6604E-11	$D_{T_{Fick-intra}}$	IRM	[126]
0.465	θ_i	In-Situ	298	3.8715E-11	$D_{T_{Fick-intra}}$	IRM	[126]
0.576	θ_i	In-Situ	298	3.7998E-11	$D_{T_{Fick-intra}}$	IRM	[126]
0.676	θ_i	In-Situ	298	3.8715E-11	$D_{T_{Fick-intra}}$	IRM	[126]
0.754	θ_i	In-Situ	298	1.0041E-10	$D_{T_{Fick-intra}}$	IRM	[126]
0.810	θ_i	In-Situ	298	6.6562E-11	$D_{T_{Fick-intra}}$	IRM	[126]
0.873	θ_i	In-Situ	298	9.1452E-11	$D_{T_{Fick-intra}}$	IRM	[126]
0.905	θ_i	In-Situ	298	1.3540E-10	$D_{T_{Fick-intra}}$	IRM	[126]
0.932	θ_i	In-Situ	298	7.0400E-11	$D_{T_{Fick-intra}}$	IRM	[126]
0.956	θ_i	In-Situ	298	4.4957E-11	$D_{T_{Fick-intra}}$	IRM	[126]
0.963	θ_i	In-Situ	298	6.6562E-11	$D_{T_{Fick-intra}}$	IRM	[126]

Continued on Next Page...

Table 1 – continued from previous page

Dosing Amount	Dosing Unit	Method	Temp.	Diffusivity Value	Diffusivity Type	Meas. Method	Ref.
0.975	θ_i	In-Situ	298	4.5805E-11	$D_{T_{Fick-intra}}$	IRM	[126]
n-Hexane							
13.33	molec./ u.c	Ex-Situ (sealed)	–	4.2000E-09	$D_{S_{App}}$	NMR PFG	[125]
3.33	molec./ u.c	Ex-Situ (sealed)	–	4.2000E-09	$D_{S_{Intra}}$	NMR PFG	[125]
n-Pentane							
16.00	molec./ u.c	Ex-Situ (sealed)	–	9.9000E-09	$D_{S_{App}}$	NMR PFG	[125]
neo Propane							
0.060	θ_i	In-Situ	298	1.3150E-12	$D_{T_{Fick-intra}}$	IRM	[126]
0.100	θ_i	In-Situ	298	2.0593E-12	$D_{T_{Fick-intra}}$	IRM	[126]
0.122	θ_i	In-Situ	298	3.4750E-12	$D_{T_{Fick-intra}}$	IRM	[126]
0.148	θ_i	In-Situ	298	4.1890E-12	$D_{T_{Fick-intra}}$	IRM	[126]
0.173	θ_i	In-Situ	298	4.7744E-12	$D_{T_{Fick-intra}}$	IRM	[126]
0.197	θ_i	In-Situ	298	4.3485E-12	$D_{T_{Fick-intra}}$	IRM	[126]
0.210	θ_i	In-Situ	298	3.8873E-12	$D_{T_{Fick-intra}}$	IRM	[126]
0.232	θ_i	In-Situ	298	2.9925E-12	$D_{T_{Fick-intra}}$	IRM	[126]
0.278	θ_i	In-Situ	298	2.1377E-12	$D_{T_{Fick-intra}}$	IRM	[126]

Continued on Next Page...

Table 1 – continued from previous page

Dosing			Temp.	Diffusivity		Meas.	Ref.
Amount	Unit	Method		Value	Type	Method	
0.462	θ_i	In-Situ	298	1.0909E-12	$D_{T_{Fick-intra}}$	IRM	[126]
0.589	θ_i	In-Situ	298	7.0978E-13	$D_{T_{Fick-intra}}$	IRM	[126]
0.732	θ_i	In-Situ	298	4.0684E-14	$D_{T_{Fick-intra}}$	IRM	[126]
0.813	θ_i	In-Situ	298	8.8820E-13	$D_{T_{Fick-intra}}$	IRM	[126]
0.862	θ_i	In-Situ	298	1.4711E-12	$D_{T_{Fick-intra}}$	IRM	[126]
0.910	θ_i	In-Situ	298	3.3475E-12	$D_{T_{Fick-intra}}$	IRM	[126]
0.929	θ_i	In-Situ	298	3.7447E-12	$D_{T_{Fick-intra}}$	IRM	[126]
0.949	θ_i	In-Situ	298	1.9837E-12	$D_{T_{Fick-intra}}$	IRM	[126]
0.968	θ_i	In-Situ	298	1.6456E-12	$D_{T_{Fick-intra}}$	IRM	[126]
0.983	θ_i	In-Situ	298	1.3398E-12	$D_{T_{Fick-intra}}$	IRM	[126]
0.990	θ_i	In-Situ	298	7.2317E-13	$D_{T_{Fick-intra}}$	IRM	[126]
Propane							
1	bar?	Ex-Situ (sealed)	328.1	3.7799E-08	$D_{S_{App}}$	NMR PFG	[127]
1	bar?	Ex-Situ (sealed)	318.0	3.0120E-08	$D_{S_{App}}$	NMR PFG	[127]
1	bar?	Ex-Situ (sealed)	308.0	2.4406E-08	$D_{S_{App}}$	NMR PFG	[127]

Continued on Next Page...

Table 1 – continued from previous page

Dosing			Temp.	Diffusivity		Meas.	Ref.
Amount	Unit	Method		Value	Type	Method	
1	bar?	Ex-Situ (sealed)	298.0	1.9617E-08	$D_{S_{App}}$	NMR PFG	[127]
26.67	molec./ u.c	Ex-Situ (sealed)	–	2.4000E-09	$D_{S_{App}}$	NMR PFG	[125]
26.67	molec./ u.c	Ex-Situ (sealed)	–	2.7000E-08	$D_{S_{App}}$	NMR PFG	[125]
Reported Diffusivities for Adsorbates in DMOF-1 ($Zn_2(bdc)_2$ dabco							
Benzene							
saturated?		Ex-Situ (sealed)	–	298.0	1.0E10-11	$D_{S\parallel}$ NMR PFG	[128]
saturated?		Ex-Situ (sealed)	–	298.0	3.0E10-13	$D_{S\perp}$ NMR PFG	[128]
CO_2							
saturated?		Ex-Situ (sealed)	–	298.0	6.0E10-09	$D_{S_{App}}$ NMR PFG	[128]

References

(16) Stallmach, F.; Gröger, S.; Künzel, V.; Kärger, J.; Yaghi, O. M.; Hesse, M.; Müller, U. *Angew. Chem. Int. Ed. Engl.* **2006**, *45*, 2123–6.

(121) Hertel, S.; Wehring, M.; Amirjalayer, S.; Gratz, M.; Lincke, J.; Krautscheid, H.; Schmid, R.; Stallmach, F. *Eur. Phys. J. Appl. Phys.* **2011**, *55*, 20702.

(122) Zhao, Z.; Li, Z.; Lin, Y. *Ind. Eng. Chem. Res.* **2009**, 10015–10020.

(123) Ford, D. C. D.; Dubbeldam, D.; Snurr, R. Q.; Künzel, V.; Wehring, M.; Stallmach, F.; Kärger, J.; Müller, U. *J. ...* **2012**, *3*, 930–933.

(124) Gratz, M.; Hertel, S.; Wehring, M.; Stallmach, F.; Galvosas, P. *New J. Phys.* **2011**, *13*, 045016.

(125) Wehring, M.; Gascon, J.; Dubbeldam, D.; Kapteijn, F.; Snurr, R. Q.; Stallmach, F. *J. Phys. Chem. C* **2010**, *114*, 10527–10534.

(126) Chmelik, C.; Kärger, J.; Wiebcke, M.; Caro, J.; van Baten, J.; Krishna, R.; Baten, J. M. V. *Microporous Mesoporous Mater.* **2009**, *117*, 22–32.

(127) Arnold, L.; Averlant, G.; Marx, S.; Weickert, M.; Müller, U.; Mertel, J.; Horch, C.; Peksa, M.; Stallmach, F. *Chemie Ing. Tech.* **2013**, *85*, 1726–1733.

(128) Wehring, M.; Amirjalayer, S.; Schmid, R.; Stallmach, F. **2011**, *2*, 1–2.